TECHNISCHE
UNIVERSITÄT
DRESDEN

Syntheses and Assemblies of Noble Metal Nanostructures

Dissertation

zur Erlangung des akademischen Grades

Doctor rerum naturalium

(Dr. rer. nat.)

vorgelegt

der Fakultät Mathematik und Naturwissenschaften
der Technischen Universität Dresden

von

Dipl.-Chem. Christoph Ziegler

geboren am 24.05.1984 in Görlitz

Eingereicht am:	08.11.2012
Tag der Verteidigung:	15.12.2012
Gutachter:	Prof. Dr. rer. nat. habil. Alexander Eychmüller Prof. Dr. rer. nat. habil. Stefan Kaskel

Die Dissertation wurde in der Zeit von Mai/2009 bis November/2012 in der Professur für Physikalische Chemie/Elektrochemie angefertigt.

Meiner Familie

“Es ist eine fast allgemeine Klage, daß schon jetzt - ich bitte Sie zu bedenken: schon jetzt - die Kolloidchemie ein fast unübersehbar großes Wissenschaftsgebiet geworden ist.”

«Die Welt der vernachlässigten Dimensionen»
Wolfgang Ostwald, 1927

Contents

List of Figures

figures in color online

List of Tables

Abbreviations

ABC	absorbing boundary conditions
abs	absorption
Abs.	absorbance
at	atoms
ATZ	5-amino-tetrazole
BEM	boundary element method
BET	Brunauer-Emmet-Teller
conc.	concentrated
corr	corrected
CTAB	cetyltrimethylammonium bromide
DDA	discrete dipole approximation
DTA	differential thermal analysis
EDX	energy-dispersive X-ray spectroscopy
EF	enhancement factor
ext	extinction
FDTD	finite-difference time-domain
FEM	finite elements method
GC-MS	gas chromatography-mass spectrometry
GMT	generalized Mie theory
ICP-OES	iductively coupled plasma optical emission spectroscopy
Im	imaginary part
LbL	layer by layer
LED	light-emitting diode
loc	local
max	maximum
MIT	Massachusetts Institute of Technology
MMP	multiple multipoles
MOM	method of moments
MTZ	5-methyl-tetrazole
norm.	normalized
OLED	organic light-emitting diode

p-ATP	para-aminothiophenol
PAH	polyallylamine hydrochloride
PDDA	polydiallydimethylammonium chloride
PML	perfectly matched layer
PTFE	polytetrafluoroethylene
R6G	rhodamine 6G
Re	real part
rel.	relative
sca	scattering
SEF	surface-enhanced fluorescence
SEM	scanning electron microscopy
SERS	surface-enhanced Raman scattering
SHINERS	shell-isolated nanoparticle-enhanced Raman scattering
TEM	transmission electron microscopy
TGA	thermogravimetric analysis
TZ	tetrazole
UV	ultraviolett
Vis	visible
XANES	X-ray absorption near edge structure
XPS	X-ray photoelectron spectroscopy

Introduction

Size matters! For everyone who deals with nanoscale materials this is self-evident. It just depends on the size of a particle whether it diffuses or not, whether it dialyses or not and whether it can be removed from a solution by filtration or not. Besides the pure geometric effects other material properties are also influenced by size. The most prominent one is of cause the change of the electronic properties of semiconducting materials due to quantum confinement effects. But also for metals the size plays an important role. The excitation of a collective electron oscillation in a bulk metal by light is not possible directly because of a mismatch in momentum. For small particles this constraint vanishes. The strong interaction of the visible light with the free electron gas of the nanoscale metal is responsible for the fascinating optical properties of small metal particles.

Although many of these effects have been known to scientists for a long time, the research interest in this field increased drastically during the last decades. This is when colloid science became nano science. But changing the name does not change the science essentially. Modern analytical tools and powerful computers allowed for an accurate characterization of the small structures and a precise theoretical prediction of their properties, respectively. Hence, it was possible to optimize known synthetic procedures and develop new ones much faster because of a detailed understanding of the underlying mechanisms.

In the beginning of this work an introduction to the fascinating optical properties of noble metals will be given. Focussing mainly on gold nanostructures, different influences like the size and the size distribution of the particles on their response to the electromagnetic radiation will be discussed.

The second part of the present work deals with the aqueous synthesis of spherical gold nanoparticles. Due to the ease of preparation and their superior stability these materials have a broad range of applications. In the frame of this work a new seeded growth synthesis could be developed that yields highly uniform spherical particles over a large range of sizes. Furthermore it was possible to reveal the growth mechanism of these particles utilizing electron microscopy and optical investigations coupled with theoretical calculations.

Not only the size but also the shape of the gold nanoparticles is relevant for their optical properties. Therefore the influence of the presence of chloride ions on the shape and size of gold nanostructures will be discussed. It has been found that many different particle morphologies are accessible by controlling the chloride concentration, the reducing agent concentration and the pH, respectively.

In order to practically use the great properties of nanoparticles for certain applications like sensing, light harvesting or waveguiding, a specific assembly into larger or macroscopic structures may be necessary. Particularly for noble metal nanoparticles a close assembly will result in a coupling of the particle plasmons. This coupling causes very large field enhancements between the nanoparticles. In the present work non-ordered assemblies of differently sized gold nanoparticles have been investigated with respect to their optical properties and their suitability as SERS substrates.

For many applications not only the size and the shape of the particles are relevant. Especially when the surface is involved in a certain process, also the molecules adsorbed to the surface become important. However, considering the formation of nanostructures in solution, surface active molecules are crucial for their stability. Supposing there is a molecule that could stabilize the particles in solution and afterwards be removed completely for a certain application, this would be a great advantage. Tetrazoles are a group of heterocyclic organic compounds that decompose completely in solely gaseous products at moderate temperatures. Besides the tetrazole group has similar physical and chemical properties like the carboxyl group. Therefore this class of molecules might be suitable as a stabilizer and easily removable. For that reason the synthesis of silver nanoparticles with different tetrazole derivatives has been investigated.

The last section of this work deals with another great potential of noble metals - their application in catalysis. Again, size matters. Most of the industrial relevant reactions are heterogeneously catalyzed. Therefore the reaction takes place on the surface of a solid catalyst. By decreasing the particle size of a material its specific surface area increases considerably. However, very small particles are less stable. Therefore it is common to use materials with a high surface area as a support for the catalyst. Besides the stabilization, the supporting material can also be of relevance for the catalytic process.

In the frame of the present work zinc oxide aerogels with different morphologies have been synthesized and used as a support. The direct formation of mixed noble metal/zinc oxide gels is a facile way to obtain a support with a high surface area and small, well dispersed noble metal nanoparticles. A possible formation of an intermetallic zinc/palladium phase is probably the reason for the outstanding selectivity of these materials toward the semi-hydrogenation of acetylene.

1. Metal optics

Designing new materials for certain purposes as well as the explanation of the properties of known materials require a sufficient understanding of the respective theoretical background. Looking for example for new optical sensors or structures that are capable to enhance the efficiency of solar cells or light emitting devices, it is necessary to understand the optical behavior of the used materials.

Since the scope of this work mainly deals with noble metal nanostructures, the focus of this chapter will be on the theoretical explanation of their outstanding properties. In the beginning the optical properties of noble metals will be discussed. Therefore it is useful to start with the dielectric function of these metals and how this material specific function is influenced by different factors like size of the structures, surrounding media and charge effects. Furthermore the interaction of the electromagnetic radiation with noble metals as well as a couple of possibilities to model these interactions will be discussed.

1.1. Basics in electromagnetism and solid state physics

The fascinating interactions between electromagnetic radiation and matter especially metals, has encouraged the research interests of scientists countless times during the last centuries. A strong interest to understand the macroscopic properties like the reflectivity of metals and the color of certain metals as well as some special optical effects that are caused by the nanoscale dimension of the material like surface-enhanced Raman scattering (SERS) and surface-enhanced fluorescence (SEF), led to the development of suitable theories to describe these effects.

One of the central concepts to understand the optical behavior of metals are the Maxwell equations in matter. Being one of the basic concepts of electrodynamics they are capable to describe correctly the spatial and time evolution of electromagnetic fields in matter. However, the original set of equations given by Maxwell in the 19th century was only suitable to explain the interaction of electric and magnetic fields and their propagation in free space. It took until the beginning of the 20th century as solid state physics delivered concepts to explain how materials are composed and hence can interact with matter.

1.1.1. The electromagnetic radiation

Since most of the spectroscopic methods are based on the interaction of matter with electromagnetic radiation and the final analysis of the radiation, it is useful to clarify its properties. An electromagnetic wave consists of an electric (**E**) and a magnetic (**B**) field component, which are oscillating in phase and are perpendicular to each other and to the direction of travel, represented by the wave vector **k** (see figure 1.1.1). In vacuum the wave travels with the characteristic speed of light c.

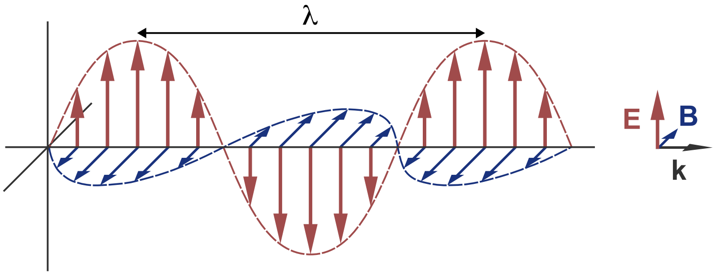

Figure 1.1.1.. The electromagnetic radiation is a transverse wave with an electric (**E**) and a magnetic (**B**) field component that are perpendicular to each other. This wave has a specific wavelength λ and travels in the direction of the wave vector **k**.

The energy of an electromagnetic wave just depends on its frequency and not on its intensity or on its wavelength. Although the wavelength can be related to the frequency ω, this relation depends on the medium, the electromagnetic wave is traveling in. The propagation speed of a plane with constant phase of the traveling wave is called the phase velocity. It is defined as:

$$v = \frac{\omega}{k} \quad \text{with} \quad \omega = \frac{2\pi}{T} \quad \text{and} \quad k = \frac{2\pi}{\lambda}. \tag{1.1.1}$$

Considering now electromagnetic waves in vacuum the phase velocity v is equal to the speed of light c and therefore the dispersion law reads:

$$\omega = ck. \tag{1.1.2}$$

Dispersion in general describes frequency-dependent effects in wave propagation, for example the different angles of refraction for different colors of light traveling through an optical prism. The dispersion law or dispersion relation states how the frequency, the wavelength and the dielectric function ε are connected with each other. Moving from vacuum to other media, the phase velocity varies from the speed of light in vacuum and c in equation 1.1.2 has to be replaced by $c/\sqrt{\varepsilon(\omega)}$.

$$\varepsilon(\omega, k)\,\omega^2 = c^2\,k^2 \tag{1.1.3}$$

This is now the general dispersion relation for a plane wave traveling through an isotropic medium other than the vacuum. In other words this is how the wave responds to the penetrated medium.

1.1.2. Maxwell equations

Together with the Lorentz force law the set of partial differential equations known as Maxwell's equations form the basics of classical electrodynamics. As a first step it might be useful to understand the meaning of all four equations. They all describe properties of the electric and the magnetic field and their interaction. A detailed discussion of Maxwell's equations and their applications can be found in many textbooks.[1–5] Here just a basic overview will be presented.

Equation 1.1.4, also known as Gauss's law, states that the divergence of the electric vector field $\mathbf{D}$ equals the number of free charges in the volume under consideration (ρ_F). With other words it says that in an electric field there are sources and drains for electrical field lines, which are represented by either positive or negative charges. The next equation is Gauss's law for magnetism (1.1.4) which says that a magnetic field $\mathbf{B}$ does not have any sources. With respect to a closed surface under consideration this will mean that the number of magnetic field lines entering the enclosed volume equals the number of magnetic field lines leaving that volume.

$$\nabla \cdot \mathbf{D} = \rho_\mathrm{F} \tag{1.1.4}$$

$$\nabla \cdot \mathbf{B} = 0 \tag{1.1.5}$$

$$\nabla \times \mathbf{E} = -\frac{\partial}{\partial t}\mathbf{B} \tag{1.1.6}$$

$$\nabla \times \mathbf{H} = \mathbf{J}_\mathrm{F} + \frac{\partial}{\partial t}\mathbf{D} \tag{1.1.7}$$

Whilst the first two laws describe just the electric and the magnetic field, respectively, the last two laws describe the interactions of the electric and the magnetic field. Equation 1.1.6 is Faraday's law of induction. It describes the well known effect of induction, which means that a changing magnetic field creates an electric field $\mathbf{E}$. The last equation is Ampère's circuital law with Maxwell's correction (1.1.7). It conveys that a changing electric field or an electric current $\mathbf{J}_\mathrm{F}$ creates a magnetic $\mathbf{H}$-field.

Maxwell's equations are presented above in the form of macroscopic electromagnetism. This form is needed to describe the evolution of electromagnetic fields in the presence of charges, currents and polarizable matter. It contains the two material dependent vector fields the electric displacement $\mathbf{D}$, alternatively called the electric induction or the electric flux density and the magnetizing field $\mathbf{H}$, also called the auxiliary magnetic field or the magnetic field intensity. In other words this form of Maxwell's equations allows to account for external fields and fields that are due to the interaction with matter. Introducing the local polarization of matter $\mathbf{P}$ and the local magnetization $\mathbf{M}$ the four macroscopic fields can be linked further.

$$\mathbf{D} = \varepsilon_0 \mathbf{E} + \mathbf{P} \tag{1.1.8}$$

$$\mathbf{H} = \mu_0^{-1} \mathbf{B} - \mathbf{M} \tag{1.1.9}$$

To finally be able to solve real problems, a connection to material specific constants is needed. They can be introduced by the constitutive relations:

$$\mathbf{J}_\mathrm{F} = \sigma \mathbf{E}, \quad \mathbf{B} = \mu \mu_\mathbf{0} \mathbf{H}, \quad \mathbf{P} = \varepsilon_\mathbf{0} \chi \mathbf{E}. \tag{1.1.10}$$

Now the material properties can be described via the phenomenological coefficients for the conductivity σ, the permeability μ and the electric susceptibility χ.

Applying the right geometry dependent boundary conditions to this set of equations, it is possible to accurately describe the evolution of the electromagnetic fields in the system under consideration. However, just for very few cases there exists an analytical solution to the set of differential equations. For all other geometries they have to be solved numerically.

1.1.3. Obtaining the dielectric function of metals from solid state physics

In the last section it was shown that an external electric field causes a polarization inside a medium. The material specific dielectric function ε directly connects the external field with the electric displacement field **D**, which accounts for effects of free charge in the medium, and the polarization density **P**.

$$\mathbf{D} = \varepsilon_0 \mathbf{E} + \mathbf{P} = \varepsilon_0 \varepsilon \mathbf{E} \tag{1.1.11}$$

In optics the material specific function that describes the propagation of light through a medium is the index of refraction. Both quantities are complex valued and directly connected to each other.

In order to develop a form for the dielectric function of a metal one can start with the simplest model that is suitable to describe the general structure of metals. It assumes a rigid lattice of positively charged metal ions and a freely moving electron gas in between. An external electric field can deflect the electrons relative to their equilibrium position. This can be described by Newton's equation of motion (1.1.12). In the following just the one dimensional case will be discussed, which makes it easier to understand the main concept.

$$F = m \cdot a = m \cdot \frac{d^2 r(t)}{dt^2} = \sum_i F_i(r,t) \tag{1.1.12}$$

For an oscillating field the differential equation can be rewritten to give equation 1.1.13 which represents a damped harmonic oscillator.

$$m \left(\frac{d^2 r(t)}{dt^2} + \Gamma \frac{dr(t)}{dt} \right) = e\, E(t) \tag{1.1.13}$$

Here m is the effective mass of the electrons, $r(t)$ is the displacement from the equilibrium position, Γ is a phenomenological damping constant, e describes the effective charge and $E(t)$ is the external oscillating field. The differential equation can be solved using the ansatz 1.1.14 for the oscillating field.

$$E(t) = E\, \mathrm{e}^{\imath \omega t} \quad \text{and} \quad r(t) = r\, \mathrm{e}^{\imath\, \omega\, t} \tag{1.1.14}$$

Applying the definitions for the polarization:

$$P = n \cdot r \cdot e \tag{1.1.15}$$

one ends up with a solution for the dielectric function of a metal, also known as the Drude model for the dielectric function of a metal (1.1.16).

$$\varepsilon(\omega) = 1 - \frac{n\,e^2}{m\,(\omega^2 + \imath\,\Gamma\,\omega)} \tag{1.1.16}$$

Using the definition for the plasma frequency,

$$\omega_p = \sqrt{\frac{n\,e^2}{m}} \tag{1.1.17}$$

and setting the damping to zero, one obtains equation 1.1.18 as the most simple form of the dielectric function of a metal for the non-damped and therefore non-absorbing case.

$$\varepsilon(\omega) = 1 - \frac{\omega_p^2}{\omega^2} \tag{1.1.18}$$

Thus, it can be seen that the dielectric function is a function of the frequency of the incoming electromagnetic radiation. One can conclude that metals respond differently for different frequencies of the approaching oscillating electric field.
Now the obtained expressions for the materials response to the traveling wave 1.1.18 and the response of the plane wave to the material 1.1.3 can be plugged in to the equation for a plane wave,

$$E = E_0\,\mathrm{e}^{-\imath\,(\omega\,t - k\,r)} \tag{1.1.19}$$

to finally get to the expression for a plane wave traveling inside a metal.

$$E = E_0\,\mathrm{e}^{-\imath\left(\omega\,t - \sqrt{\frac{\omega^2 - \omega_p^2}{c^2}}\,r\right)} \tag{1.1.20}$$

The visualization of the amplitude of the electric field at the border from vacuum to inside the metal reveals two different cases (see figure 1.1.2). For light having a frequency larger than the plasma frequency of the metal the wave can penetrate into the metal and travels inside the medium with a different wavelength, determined by the dispersion relation 1.1.3.
If the frequency of the incident light is smaller than the plasma frequency of the metal, the wave can not penetrate into the metal and hence is reflected. It can also

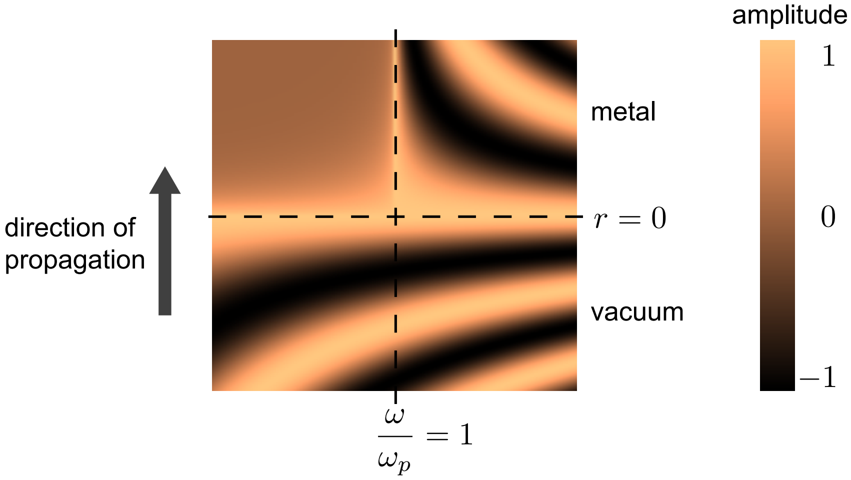

Figure 1.1.2.. Depending on the frequency of the electromagnetic wave incident on a metal surface it will either be transmitted (for $\omega > \omega_p$) or be reflected (for $\omega < \omega_p$).

be seen that the amplitude of the evanescent field vanishes very quickly.

In conclusion it can be said that two major properties of metals can be explained by the above presented and rather simple approach. Metals reflect light in the long wavelength regime, which is very well known and metals become transparent for very short wavelengths, which has been observed for alkali metals and is known as the ultraviolet transparency.

Furthermore all metals should be white, since they reflect all parts of the visible light. However, the above presented derivation is not valid for all metals. Especially in gold and copper the dielectric functions are not solely determined by the free electron oscillation, included in the Drude model, but additionally show interband transitions in the visible region of the light. These transitions influence the dielectric function in a way that they just reflect the lower energy part of the visible spectrum and hence are colored.

1.1.4. Dielectric function of gold

Gold is by far the most studied metal in the field of plasmonics. Although not being aware of the physical principles that are responsible for the coloration of nanometer sized gold particles these materials have been used by men since many centuries. It was not until the 19th century when Michael Faraday started his intensive studies on colloidal gold that people became interested in understanding the reasons for the unusual color of the gold particles.

Fitting Drude parameters to experimental values

In principle it should always be possible to use the experimentally determined values of the dielectric function for all numerical and analytical simulations of the optical properties of gold nanostructures. So where is the need for an analytical expression that has been fitted to the discrete values? There are mainly two reasons.

Using an analytical expression in some numerical simulations (e. g. in FDTD) can lead to savings in time and memory. Furthermore a fit to an expression that contains coefficients with a certain physical meaning will be essential to correct the dielectric function for deviations due to the limitation of the free mean path of the electrons in small particles compared to the bulk value and a changed density of charge carriers, respectively.

There are several approaches in the literature that deal with various possibilities to fit a certain model function to experimental values of the dielectric function of gold. The so called "L4-model" uses a sum of four lorentzians to represent the dielectric function.[6] To be exact, they additionally use a simplified Drude term, which leads to a total of 14 parameters to represent their fit function. Besides, this model is not capable to include any corrections like stated above.

Another work claims to give a fit function, where all parameters have a physical meaning.[7] They use two critical point functions to account for the interband transitions and a full Drude term. Therefore this model should be able to include corrections to the dielectric function. However, having a closer look, it turns out that the parameters for the Drude part are not within a physical sense at all. For wavelengths larger than approximately 650 nm the Drude part of the fit function should represent the dielectric function well, since in this region no interband transitions are present. Unfortunately this is not the case for the parameters presented.

Applying current-density-functional calculations including relativistic effects, it has been shown that there are more than two interband transitions in the energy range relevant for plasmonic modeling.[8] On the other hand it is not very useful to include four or five interband transitions in a fit function, since the number of parameters will increase significantly and therefore the advantages of using a fit function will become disproportionate.

It was possible to overcome the mentioned problems by combining different methods and extending the fit function with a separation term. One part of the fit function

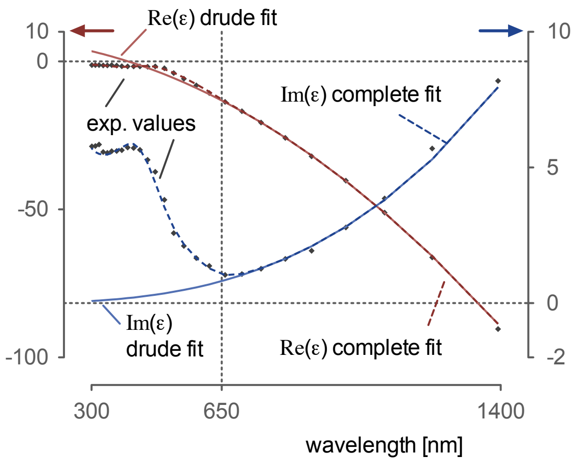

Figure 1.1.3.. The experimental data for the dielectric function of gold by Johnson and Christy[9] can be very well reproduced using equation 1.1.23 together with the parameters shown in table 1.1.1. For wavelengths larger than 650 nm the dielectric function can be solely fitted with the Drude part. Below 650 nm interband transitions become significant, which especially affects the imaginary part of the data.

is the Drude model for the dielectric function of a metal:

$$\varepsilon(\omega) = \varepsilon_\infty - \frac{\omega_p^2}{\omega(\omega + \imath\Gamma)}. \tag{1.1.21}$$

This representation is almost equal to the form derived in section 1.1.3. By introducing ε_∞ one can account for the background polarization of the core electrons given by:[10]

$$\mathbf{P}_\infty = \varepsilon_0 \left(\varepsilon_\infty - 1\right) \mathbf{E}. \tag{1.1.22}$$

The effects of the interband transitions will be incorporated by two lorentzians. These are multiplied by a separation term, whose value changes from one to zero in the range where the interband transitions become negligible.

$$\varepsilon(\omega) = \varepsilon_\infty - \frac{\omega_p^2}{\omega(\omega + \imath\Gamma)} + \frac{1}{\mathrm{e}^{\frac{a-\omega}{b}} + 1} \cdot \left(\sum_{i=1}^{2} \frac{A_i}{\left(\omega - B_i\right)^2 + \imath\omega C_i} \right) \tag{1.1.23}$$

This is now the whole fit function consisting of eleven parameters in total. The results of the global minimum search are presented in table 1.1.1 and figure 1.1.3. To obtain correct and useful parameters for the fit function it is necessary to take great care in finding the global minimum in the optimization procedure. Therefore

Table 1.1.1.. Parameters for the fit of equation 1.1.23 to the dielectric function of gold.

Drude parameters	ε_∞	7.993
	ω_0	8.779
	Γ	0.073
separation parameters	a	1.944
	b	0.082
lorentzian parameters	A_1	-19.864
	B_1	5.909
	C_1	0.243
	A_2	5.963
	B_2	3.480
	C_2	-0.348

the optimization process was split into two steps. First just the Drude part of the dielectric function has been fitted to the experimental values for wavelengths larger than 650 nm. Since this step just includes three parameters to be optimized it is quite easy to find the global minimum by simply choosing appropriate initial conditions. Once the parameters are found they will be fixed during the second step of the fit. Now the complete equation 1.1.23 was used to fit the experimental values in the wavelength regime from 300-1400 nm, which is the relevant range for plasmonic modeling applications. In the second step there are as many as eight parameters left to be optimized. Besides, it is harder to find convenient initial conditions. To handle this problem a mesh of 15000 starting positions has been used and the minimum on each point was evaluated. For local minima the goodness of the fit was compared to finally end up with the global minimum. In optimization problems like in the present case, it is always difficult to find a global minimum. However, the number of mesh points has been successively increased, always resulting in the same minimum.

1.2. Metal optics on the nanoscale

If the dimension of a metal particle becomes equal to or smaller than the wavelength of the interacting light, new optical properties emerge. Due to the spatial confinement to a small volume, the electron gas can oscillate in phase with the external electromagnetic field. Depending on particle size, shape, material and the surrounding medium, resonances of these oscillations can occur for certain excitation frequencies. For silver and gold these resonances are in the same energy range as the visible and near-infrared light, which is why nanostructures of these metals are used for optical applications.

1.2.1. Plasmonics

Today the field of plasmonics is an important part of nanoscience. It deals with all optical phenomena that occur in structures made of mainly gold and silver and that are in the nanoscale size regime. The control of light at the nanoscale opens the door towards many sophisticated applications. These include enhancement phenomena, sensing applications, the use as biomarkers, the fabrication of waveguides, the development of new materials and many more. The term plasmonics is derived from *plasmon*.

A plasmon by definition is the quantum of the collective oscillation of a plasma, which in this case will be the free electron gas in a metal. There are different types of plasmons known, depending on the spatial dimension of the metal and the experimental conditions that excite the electron oscillation. Generally they can be divided into bulk plasmons, surface plasmons and localized surface or particle plasmons. In terms of nanotechnology the most important plasmons are the localized surface plasmons, which can be directly excited by light in contrast to the other types of plasmons.

In the vicinity of the structures the collective oscillation of the electrons causes an electric dipole field which is commonly referred to as electrical near-field. In contrast to the far-field the near-field just depends on the strength of the electron oscillation. The moving electrons can be considered as currents that are directly responsible for the induced fields. However, the far-field depends on the decay of the plasmon. A radiative decay or also known as radiative damping of the plasmon will cause a scattering event, whereas a non-radiative damping which consists of inter- and intraband transitions and the following transformation of the energy into heat will be a pure absorption. The combination of both events results in the extinction, which is the common quantity to characterize the overall far-field properties.

1.2.2. Quasi-static approximation for small particles

For particle sizes much smaller than the wavelength of the exciting electromagnetic radiation, the electric field inside the particle can be regarded to be constant and uniform. Therefore it is possible to treat the problem of the interaction of the exciting

field with the particle within a quasi-static approximation. This means that the spatial field distribution is calculated by assuming a particle or dipole in an static external field. Once the field distributions are known, the harmonic time dependence can easily be added.
Following the solution of Maxwell's equations for the quasi-static problem presented in many textbooks[5], one ends up with an expression for the polarizability of the particle with radius R depending on its dielectric function ε and the dielectric function of the surrounding medium ε_m.

$$\alpha = 4\pi R^3 \frac{\varepsilon - \varepsilon_m}{\varepsilon + 2\varepsilon_m} \tag{1.2.1}$$

The polarizability determines the dynamic response of the electrons to an external electric field and is a measure for the change in the electron distribution. Hence, it will be maximal for the case of a resonant excitation. This will happen whenever $|\varepsilon + 2\varepsilon_m|$ is minimized. It is obvious that for a given material the resonance position is also highly dependent on the dielectric function of the surrounding medium. Using the dielectric function for a free-electron metal 1.1.18 and assuming vacuum as the surrounding medium the resonance position can be found at frequency

$$\omega_r = \frac{\omega_p}{\sqrt{3}}. \tag{1.2.2}$$

In the frame of this approximate model it is also possible to determine the scattering and absorption cross section (C_{sca} and C_{abs}) of a particle with $R \ll \lambda$.

$$C_{\text{sca}} = \frac{k^4}{6\pi}|\alpha|^2 = \frac{8\pi}{3}k^4 R^6 \left|\frac{\varepsilon - \varepsilon_m}{\varepsilon + 2\varepsilon_m}\right|^2 \tag{1.2.3}$$

$$C_{\text{abs}} = k\,\mathrm{Im}[\alpha] = 4\pi k R^3\,\mathrm{Im}\left[\frac{\varepsilon - \varepsilon_m}{\varepsilon + 2\varepsilon_m}\right] \tag{1.2.4}$$

Here the concept of a cross section can be understood to be the "effective area" that blocks a certain part of the beam. For metal nanoparticles this area is usually larger than their physical cross section. Because of the strong dependence of the scattering on the particle dimension $C_{\text{sca}} \propto R^6$ it could be very difficult to study small particles in the presence of bigger ones. Their scattering part will just disappear in the large scattering signal of the big particles. Besides, both the scattering and the absorption cross section are directly connected to the polarizability. Therefore a resonance in the polarizability will result in a resonance in the extinction cross section that is the overall effect of scattering and absorption events $C_{\text{ext}} = C_{\text{sca}} + C_{\text{abs}}$. The extinction cross section can be directly connected to the extinction measured in UV/Vis spectroscopy via the Beer-Lambert law.

$$E = \log_{10}\left(\frac{I_0}{I}\right) = \frac{C_{\text{ext}} \cdot l \cdot N}{\ln(10)} \tag{1.2.5}$$

Here I_0 and I are the intensities of the beam before and after the sample, respectively. The particle concentration is denoted by N and l is the sample thickness. As a consequence of equation 1.2.5 it is possible to observe the resonance of the collective electron oscillation in macroscopic ensemble measurements.

1.2.3. Exact solution of the electrodynamic calculation of metal nanospheres

As stated already above, the interaction of an electromagnetic wave and a small metallic sphere can be described accurately by solving Maxwell's equations with the respective boundary conditions. For larger particles the quasi-static regime does not hold anymore due to significant phase changes of the driving electromagnetic field over the particle volume and needs to be extended considerably.

In 1908, Gustav Mie was the first who gave an analytic solution of the problem with respect to light scattering.[11] Although motivated by the wish to understand the colors of colloidal gold solutions, the developed theory holds also for non-metallic materials represented by a material specific dielectric constant. The often used term Mie Theory is somewhat misleading since it is not an independent theory but an analytical solution of Maxwell's equations for a certain geometry. Mie solved the problem by adapting it to the geometry and consequently using spherical coordinates to apply the boundary conditions. Furthermore he expanded the incident plane wave and the scattered fields in vector spherical harmonics. A detailed derivation can be found in the book by Bohren and Huffman.[5] Here just the main results, that are necessary for the treatment of the problems discussed later in this work, will be summarized.

In the exact solution higher orders are included. The order of the multipole is given by L, whereas dipole fields correspond to $L = 1$, quadrupole fields to $L = 2$, octupole fields to $L = 3$ and so on. Now the extinction and scattering cross sections can be obtained by a summation over all multipole contributions.

$$C_{\text{ext}} = \frac{2\pi r^2}{x^2} \sum_{L=1}^{\infty} (2L+1) \operatorname{Re}\left[a_L + b_L\right] \tag{1.2.6}$$

$$C_{\text{sca}} = \frac{2\pi r^2}{x^2} \sum_{L=1}^{\infty} (2L+1) \left(|a_L|^2 + |b_L|^2\right) \tag{1.2.7}$$

$$C_{\text{abs}} = C_{\text{ext}} - C_{\text{sca}} \tag{1.2.8}$$

Both the extinction and the scattering cross section depend on the so called Mie coefficients a_L and b_L, which can be calculated for the different multipoles from the Riccati-Bessel cylindrical functions ψ and ξ.

$$a_L = \frac{m\psi_L(mx)\psi_L'(x) - \psi_L(x)\psi_L'(mx)}{m\psi_L(mx)\xi_L'(x) - \xi_L(x)\psi_L'(mx)} \tag{1.2.9}$$

$$b_L = \frac{\psi_L(mx)\psi_L'(x) - m\psi_L(x)\psi_L'(mx)}{\psi_L(mx)\xi_L'(x) - m\xi_L(x)\psi_L'(mx)} \tag{1.2.10}$$

In the literature it is also common to indicate the outcome of the calculations as extinction, scattering and absorption efficiencies $Q_{\text{ext}} = Q_{\text{sca}} + Q_{\text{abs}}$. The efficiencies are the extinction, scattering and absorption cross sections normalized to the real physical cross section. Besides there are some textbooks that use σ instead of C for the cross sections.

$$Q_i = \frac{C_i}{\pi R^2} \tag{1.2.11}$$

It has been shown that the Mie theory can be extended to be used for infinite cylinders, prolate and oblate particle geometries, for multilayered spherical shells and even for clusters of many spheres.[12–15] Geometries different from spheres can be calculated by changing the coordinate system from spherical coordinates, used in the original approach by Mie, to one that matches the symmetry of the geometry. The problem of scattering by clusters of many spheres is treated within the generalized Mie theory (GMT)). Briefly, a kind of self consistent field approach is used to solve the scattering problem. In the first step every sphere in the cluster is modeled separately by just applying the electromagnetic field of the incident plane wave. In the next steps a superposition of all incident and scattered fields is used for the calculation until the change in the individual fields is smaller than a given error.

Although the outcome of the Mie theory is an analytic solution it would by very time consuming to evaluate all the multipole fields by hand. Therefore numerous implementations of the Mie solutions in different computer languages are available today. The most prominent one has been written in FORTRAN 77 and was published by Bohren and Huffman.[5] For most calculations done in the frame of this work a modified MATLAB implementation of this original code has been used.

1.3. Influences on the optical properties of gold nanospheres

The optical properties of gold nanospheres can be correctly predicted by applying Mie's theory. However, for some special cases appropriate corrections have to be applied. In small particles for example the diameter is on a comparable or smaller length scale than the mean free path of the moving electrons in the bulk. This can be taken into account by correcting the dielectric function. Likewise a change in the electron density in the particles due to charging effects can be incorporated in the dielectric function. Furthermore the influences of size distributions, different embedding media and the effect of a shell around the particle will be discussed.

1.3.1. Size distribution matters for big particles

Calculated extinction and scattering cross sections are valid for a single spherical particle embedded in a non-absorbing isotropic medium. Generally this is not what is measured in practice. Most often the extinction of an ensemble for example an aqueous gold colloid is being investigated. Although the experimental protocols used today can produce uniform gold nanoparticles with a very narrow size distribution, there is still a variation in the particle diameters.

Assuming a log-normal distribution for the particle diameters it is easy to calculate an extinction cross section for a given mean diameter and a respective standard deviation. The influence on the shape of the spectrum and the resonance positions for bigger particles is much higher than for small particles, where standard deviations up to 10 % are almost negligible (see figure 1.3.1).

For large particles the quadrupolar mode is shifted considerably towards higher energies whereas the octupolar mode is slightly shifted to lower energies. The extinction is composed of an absorption and a scattering part. Obviously, the change in the scattering part with respect to a increasing particle size distribution is significantly stronger than the change in the absorption part (see figure 1.3.2). Since the scatter-

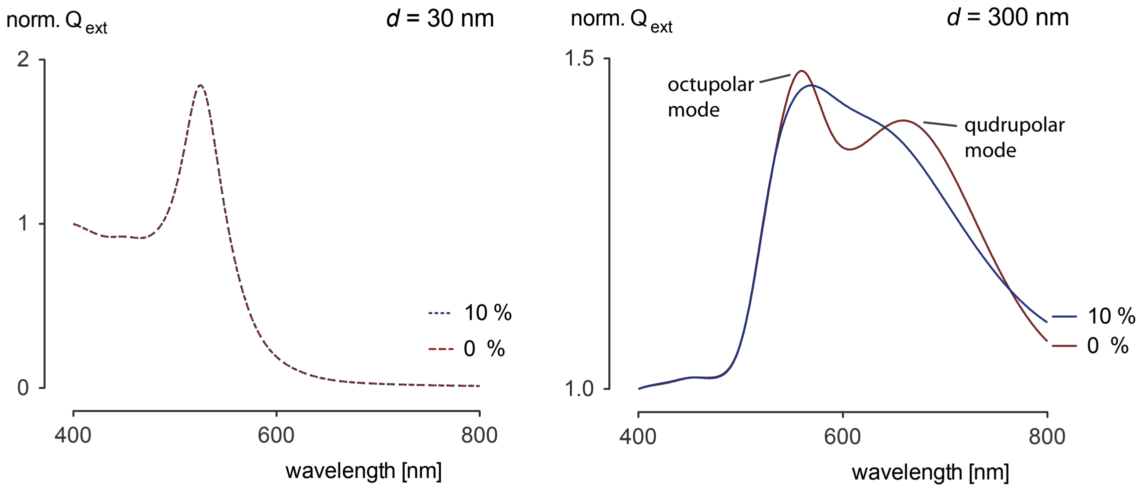

Figure 1.3.1.. For small particles a size distribution of the particle diameters has almost no effect on the optical properties. However, for large particles the extinction spectrum is significantly changed for a changed particle size distribution.

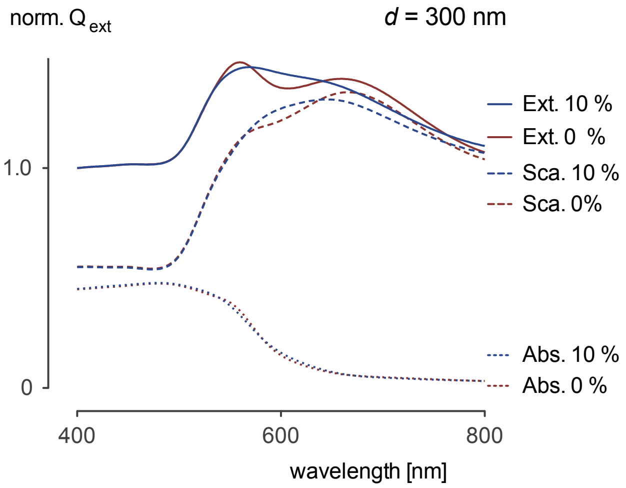

Figure 1.3.2.. The change in the extinction spectrum of large gold nanoparticles for different size distributions is mainly caused by a change in the scattering part of the extinction.

ing part becomes more dominant for larger particles, the change of the particle size distribution influences the overall extinction cross section of the particles.

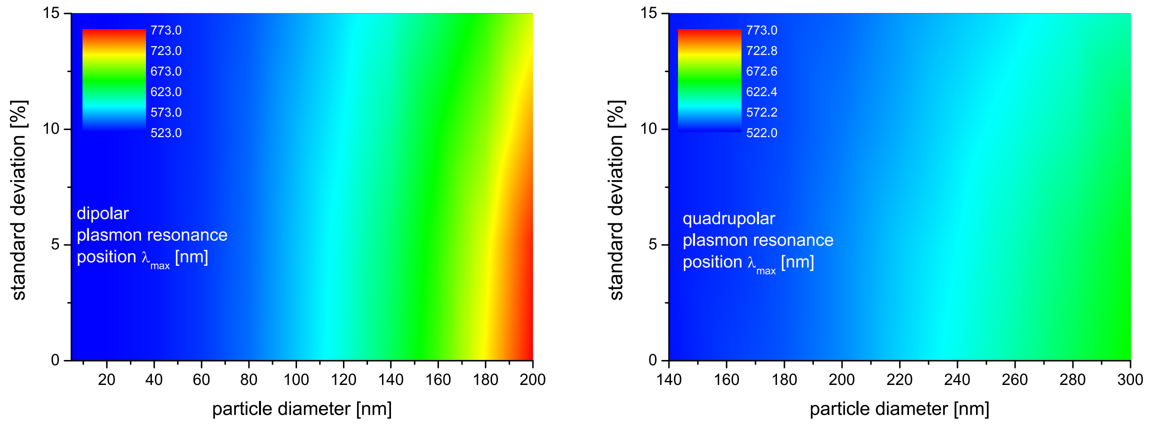

Figure 1.3.3.. Considering the dipolar and the quadrupolar plasmon mode of gold nanoparticles separately, a different dependence of the resonance position on the size distribution of the particles can be found. Whereas the dipolar mode starts being affected by the size distribution at a particle size of about 100 nm the quadrupolar mode shows a significant dependence not until a mean particle size of about 200 nm.

In extension to the quasi-static approximation the extinction, scattering and absorption cross sections are calculated from Mie theory including not only the dipolar field but also higher order multipoles. A separated extraction of the dipolar and the quadrupolar contribution reveals a different sensitivity of the two orders (see figure 1.3.3). It can be seen that the position of the quadrupolar mode hardly changes for different particle size distributions for particle diameters between 140 and 200 nm, while the position of the dipolar mode changes significantly.

1.3.2. Confinement of the mean free path of the electrons in small particles

Every freely moving particle in a closed system will at some point collide with another particle and change its traveling direction, energy or momentum. The average time between these impacts is usually referred to as relaxation time. Depending on the velocity of the particle this results in a specific average distance between the collisions which is called mean free path. If one now focuses on metallic structures the free electrons near the Fermi level are the moving particles. The Fermi energy E_F of a certain metal is therefore directly connected to the specific Fermi velocity v_F of the electrons with effective mass m_e.

$$v_\mathrm{F} = \sqrt{\frac{2E_\mathrm{F}}{m_e}} \tag{1.3.1}$$

Knowing the Fermi velocity and the relaxation time, the mean free path can easily be evaluated. For the metals gold and silver the resulting mean free path of the electrons in the bulk will be around 30-50 nm. In small nanostructures the dimension of the particles will be in the range of the mean free path or even smaller. This consequently leads to an increase in collisions of the electrons with the particle boundary. Hence, the relaxation time will become smaller and thus the damping will become larger (equation 1.3.2). Practically this can be observed in a broadening of the resonance line shape.

$$\Gamma = \frac{1}{\tau} \tag{1.3.2}$$

In small structures an additional contribution $\Delta\Gamma(R)$ to the bulk damping constant Γ_∞ has to be taken into consideration. Kreibig derived that this additional term is proportional to $1/R$.[3]

$$\Gamma(R) = \Gamma_\infty + \Delta\Gamma(R) \quad \text{with} \quad \Delta\Gamma(R) = A\frac{v_\mathrm{F}}{R} \tag{1.3.3}$$

Different theories exist how the electrons at the particle boundary are scattered. The parameter A accounts for the type of scattering event and varies for different theories but is usually in the order of 1.

Now the bulk dielectric function can be corrected for the mean free path effect.

$$\begin{aligned}\varepsilon(\omega)_\mathrm{corr} = \varepsilon(\omega)_\mathrm{bulk} &+ \omega_p^2\left(\frac{1}{\omega^2+\Gamma_\infty^2} - \frac{1}{\omega^2+\Gamma(R)^2}\right)\\ &+ \imath\frac{\omega_p^2}{\omega}\left(\frac{\Gamma(R)}{\omega^2+\Gamma(R)^2} - \frac{\Gamma_\infty}{\omega^2+\Gamma_\infty^2}\right)\end{aligned} \tag{1.3.4}$$

As expected, the correction for the mean free path confinement increases considerably for decreasing particle diameters (see figure 1.3.4). For the smallest particle diameter presented the plasmon resonance almost vanished completely due to a very high damping. The plasmon resonance position, however, is not affected by this correction. It should be mentioned that for very small particles with diameters below 10 nm quantum size effects become relevant as well.

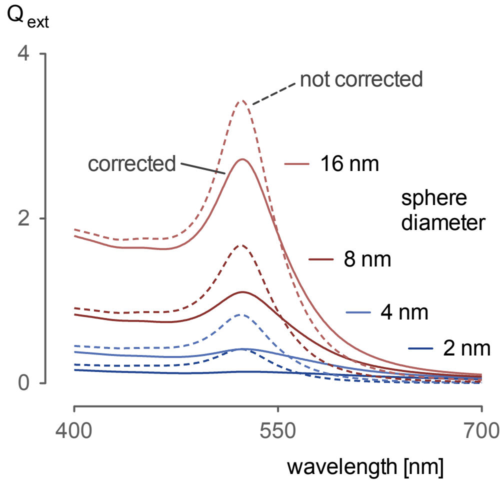

Figure 1.3.4.. It can be seen that the confinement of the mean free path of the electrons influences the plasmonic behavior of the particles significantly. The effect is the larger the smaller the particles are.

1.3.3. Effect of the change in electron concentration

Especially when dealing with aqueous solutions of gold nanoparticles charges become important. It is commonly believed that these particles are charge stabilized. This means that either the net electron concentration in the particle is higher than in the bulk or the charge is just due to ionic adsorbates. Gold nanoparticles prepared by the standard Turkevich method or comparable procedures are considered to be citrate stabilized.[16;17] In this section the effects that will occur when the charge stabilization is based on an increased electron concentration in the particles will be explained.

The electron density n is contained in the Drude part of the dielectric function of gold.

$$\varepsilon(\omega) = \varepsilon_\infty - \frac{n\, e^2}{m\,(\omega^2 + \imath\,\Gamma\,\omega)} \tag{1.3.5}$$

Together with the effective mass m and the elementary charge e it can be combined to the plasma frequency of the bulk ω_p.

$$\omega_p = \sqrt{\frac{n\, e^2}{m}} \tag{1.3.6}$$

Now it is possible to correct the plasma frequency for a change in electron density compared to the determined bulk plasma frequency. A certain percentage change C in n will give:

$$\omega_p(C) = \sqrt{1 + \frac{C}{100}} \cdot \omega_{p;\text{bulk}}. \tag{1.3.7}$$

The corrected dielectric function needed for the calculation of the extinction efficiency will therefore read:

$$\begin{aligned} \varepsilon(\omega)_{\text{corr}} = \varepsilon(\omega)_{\text{bulk}} &+ \frac{1}{\omega^2 + \Gamma^2} \left(\omega_{p;\text{bulk}}^2 - \omega_p(C)^2\right) \\ &+ \imath \frac{\Gamma}{\omega^3 + \omega\Gamma^2} \left(\omega_{p;\text{bulk}}^2 - \omega_p(C)^2\right). \end{aligned} \tag{1.3.8}$$

For gold nanoparticles with a diameter of 10 nm embedded in water the plasmon resonance position changes from 523 nm in the neutral case to 540 nm for an increase in the electron concentration of 10 % and to 509 nm for a decrease in the electron concentration of 10 %, respectively (see figure 1.3.5). Not only the plasmon resonance position changes. The extinction efficiency at the plasmon resonance position increases for a decreasing electron concentration and decreases for an increasing electron concentration. However, in the higher energy region of the spectrum, which is mainly determined by interband transitions, the extinction efficiency increases for increasing electron concentrations and decreases for decreasing electron concentrations. This region is of peculiar interest with respect to the optical determination of the particle concentrations of a gold colloid (see section 2.1.4).

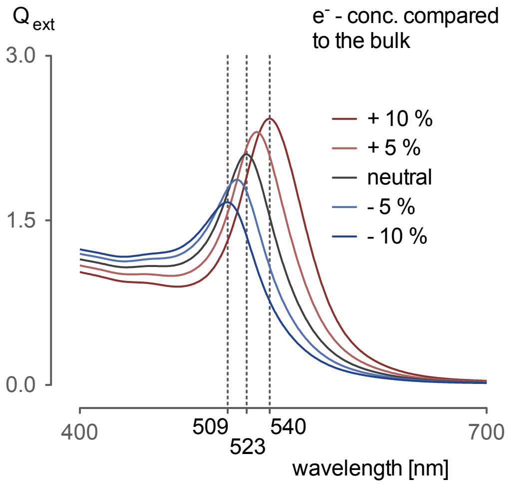

Figure 1.3.5.. Changing the electron concentration in a gold particle with a diameter of 10 nm results in a strong shift of the plasmon resonance position.

In practice it has been observed that the amount of excess electrons depends on the surface to volume ratio of the particles. Therefore it is proportional to the inverse of the particle diameter. The following equation has been found to adequately describe the plasmon resonance position of aqueous citrate stabilized gold nanoparticles. Especially for particles smaller than 20 nm normal Mie theory predicts resonance positions at longer wavelength than where they are observed. For very small particles quantum size effects will play an important role. However, in particles bigger than 10 nm they are believed to be less influential. Therefore it seems reasonable to attribute the deviation of the resonance position observed in practice to that predicted by Mie theory to the change in the electron concentration in the nanoparticles compared to the bulk.

The following radius dependent correction for the plasma frequency has been determined empirically.

$$\omega_p = \sqrt{1 + \frac{0.3}{R[\mathrm{nm}]}} \cdot \omega_{p;\mathrm{bulk}}. \tag{1.3.9}$$

Using this correction in the above given form for the dielectric function (equation 1.3.8) the extinction efficiencies for differently sized particles have been calculated. The dependence on the particle diameter gives a stronger blue shift of the plasmon resonance position for smaller particles than for bigger ones. The found resonance positions match well with those found in experimental studies.

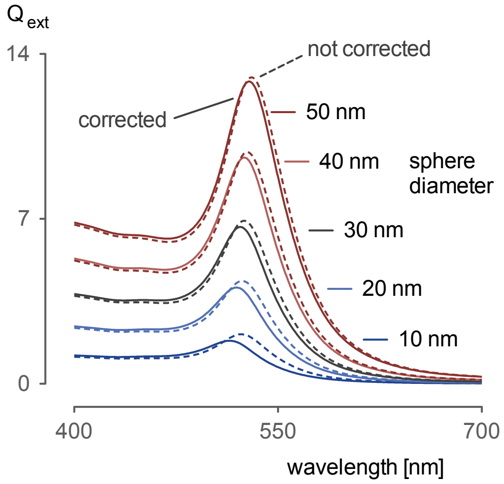

Figure 1.3.6.. Using equation 1.3.9 to account for a particle size dependent change in the electron concentration an increasing influence on the plasmon resonance position can be found for smaller particles.

1.3.4. Influence of the embedding medium

In section 1.2 it was already presented that the resonance position of the particle plasmon depends on the dielectric function of the surrounding medium. Applications of gold nanostructures will for example include their integration into devices. There and in all other uses they are embedded in a certain medium. In the following the effects of changing the refractive index of the surrounding medium on the optical response of the gold nanoparticles will be outlined.

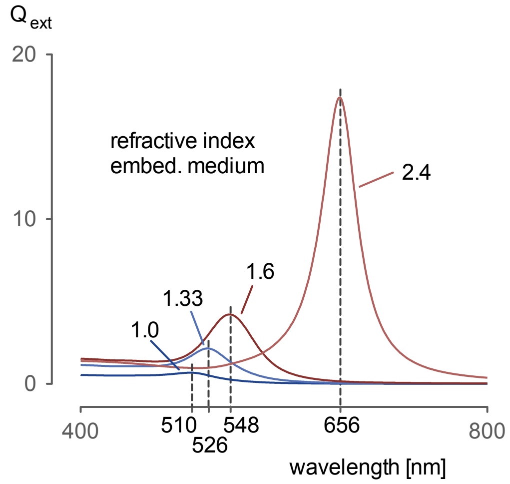

Figure 1.3.7.. The extinction efficiency of a 30 nm gold nanosphere increases significantly for higher values of the index of refraction. This is accompanied by a shift of the plasmon resonance position towards lower energies of about 160 nm.

Not only the plasmon resonance position but also the extinction efficiency depends strongly on the kind of environment. In air the refractive index will be approximately 1. Changing the refractive index to 1.33 in water, 1.6 in flint glass up to 2.4 in diamond, a strong red-shift accompanied by a very large increase in the extinction efficiency can be observed (see figure 1.3.7). The increase in Q_{ext} will be about one order of magnitude and the shift of the plasmon resonance position is almost 160 nm. However, the enormous increase in the extinction efficiency is not only due to the refractive index of the embedding medium. A higher index of refraction causes a red-shift of the plasmon resonance. In the visible range the dielectric function is affected by the response of the free electron gas and by the interband transitions. Whereas the interband transitions become significant for higher energies, the dielectric function of gold in the red and near-infrared region is mainly due to the response of the free electron gas. At the plasmon peak these electrons are resonantly oscillating. If the resonance frequency is in the same region as the interband transitions of gold, then the plasmon resonance will be damped dramatically in strength and also be red-shifted.

In order to investigate the real influence of the embedding medium on the extinction efficiency and the plasmon resonance position of a metal sphere, the dielectric function of gold was just represented by the Drude part. Therefore the interband transitions have been neglected.

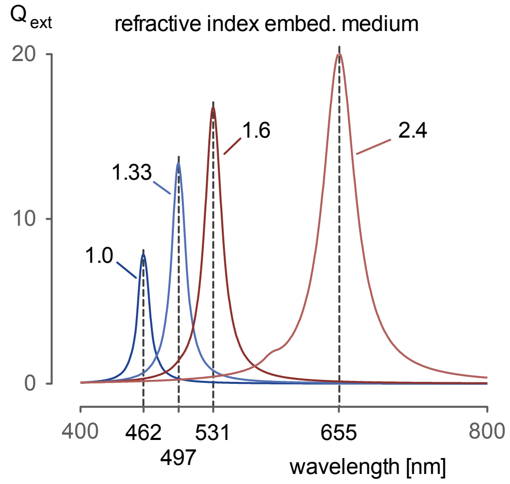

Figure 1.3.8.. If the material properties of the gold nanoparticles are just represented by the Drude part of the dielectric function, the plasmon resonance position still experiences a considerable red-shift for higher indices of refraction, but the change in the maximum extinction efficiency is less pronounced than for the case of the full representation.

It can be seen that the plasmon resonance position is still shifted to lower energies for an increasing refractive index of the surrounding medium (see figure 1.3.8). Nevertheless the increase in the extinction efficiency is considerably smaller when using just the Drude part of the dielectric function of gold rather than using the complete one. This is because of the lack of damping of the plasmon resonance due to interband transitions. The found line shapes for the plasmon resonances are almost perfect lorentzians. A critical evaluation of the results is still appropriate, since the Drude part of the dielectric function of gold also varies over the range of wavelengths under consideration.

1.3.5. Optical properties of core shell structures

If spherical nanoparticles are composed of more than one material, they still can be treated using Mie's solutions to Maxwell's equations as long as they show spherical symmetry. To be exact, the material distribution inside the particle has to have a spherical symmetry. Hence, although for example Janus particles are spherical, the material is separated to the two hemispheres and therefore the needed spherical symmetry of the material is lost. For particles made of an alloy of different metals, just the appropriate dielectric function of the alloy has to be used. Since the symmetry of the material in core shell systems stays still spherical, an analytic solution of the scattering problem for these structures can be obtained. The materials of the core and the particular layers can be metals, semiconductors and dielectrics.

Between the different layers new boundaries emerge. This has to be accounted for by the appropriate boundary conditions applied in the solution of Maxwell's equations. A recurrence solution for a z-shell structure ($z = 1, 2, 3, ...h$) has been developed by Kreibig and colleagues.[18] The Mie coefficients a_L and b_L now read:

$$a_L = -\frac{m_z\psi_L(m_z x_z)[\psi'_L(x_z) + T^h_L\chi'_L(x_z)] - \psi'_L(m_z x_z)[\psi_L(x_z) + T^h_L\chi_L(x_z)]}{m_z\xi_L(m_z x_z)[\psi'_L(x_z) + T^h_L\chi'_L(x_z)] - \xi'_L(m_z x_z)[\psi_L(x_z) + T^h_L\chi_L(x_z)]} \tag{1.3.10}$$

$$b_L = -\frac{\psi_L(m_z x_z)[\psi'_L(x_z) + S^h_L\chi'_L(x_z)] - m_z\psi'_L(m_z x_z)[\psi_L(x_z) + S^h_L\chi_L(x_z)]}{\xi_L(m_z x_z)[\psi'_L(x_z) + S^h_L\chi'_L(x_z)] - m_z\xi'_L(m_z x_z)[\psi_L(x_z) + S^h_L\chi_L(x_z)]} \tag{1.3.11}$$

with the recurrence functions:

$$T^z_L = -\frac{m_z\psi_L(m_z x_z)[\psi'_L(x_z) + T^z - 1_L\chi'_L(x_z)] - \psi'_L(m_z x_z)[\psi_L(x_z) + T^z - 1_L\chi_L(x_z)]}{m_z\xi_L(m_z x_z)[\psi'_L(x_z) + T^z - 1_L\chi'_L(x_z)] - \xi'_L(m_z x_z)[\psi_L(x_z) + T^z - 1_L\chi_L(x_z)]} \tag{1.3.12}$$

$$S^z_L = -\frac{\psi_L(m_z x_z)[\psi'_L(x_z) + S^z - 1_L\chi'_L(x_z)] - m_z\psi'_L(m_z x_z)[\psi_L(x_z) + S^z - 1_L\chi_L(x_z)]}{\xi_L(m_z x_z)[\psi'_L(x_z) + S^z - 1_L\chi'_L(x_z)] - m_z\xi'_L(m_z x_z)[\psi_L(x_z) + S^z - 1_L\chi_L(x_z)]} \tag{1.3.13}$$

For the case of no layer ($z = 0$) the expressions reduce to the general Mie solutions (see equations 1.2.9 and 1.2.9) as $T^z_L = 0$ and $S^z_L = 0$. The order of the different multipoles are denoted by L and the corresponding Riccati-Bessel functions are ψ, χ and ξ. For each shell the size parameter is defined as $x_z = k_z R_z$ with R_z being the radius of the whole cluster with z shells. The ratios of the wave vectors read

$m_z = k_{z+1}/k_z$.
Although the recurrence formulas for the Mie coefficients for multilayered particles are clear structured, it is hard to get a feeling of what the effects of different layers are. Of cause the possibilities of combining different materials and numbers and thicknesses of layers, respectively, are countless. Therefore just two examples that play an important role in modern nanoscience, because of their superior use in different occasions, will be discussed here.

It was in 1996 when Liz-Marzan, Giersig and Mulvaney presented for the first time a facile and reproducible protocol to produce gold nanospheres with a silica shell.[19] Ever since this work has been cited more than 900 times and there are now numerous applications of this kind of structures. They can be used for example in a new and very sensitive SERS technique called SHINERS (shell-isolated nanoparticle-enhanced Raman scattering)[20] and as Raman labels by incorporating a Raman reporter molecule in the silica shell.[21;22]

The inverse of the previous mentioned structure was introduced just two years later by the group of Naomi Halas. They produced particles with a thin shell of gold on silica cores.[23] Their outstanding optical properties have been explained in the light of a plasmon hybridization theory.[24] Especially for applications in the field of cancer imaging and therapy these gold nanoshells are very promising structures.[25]

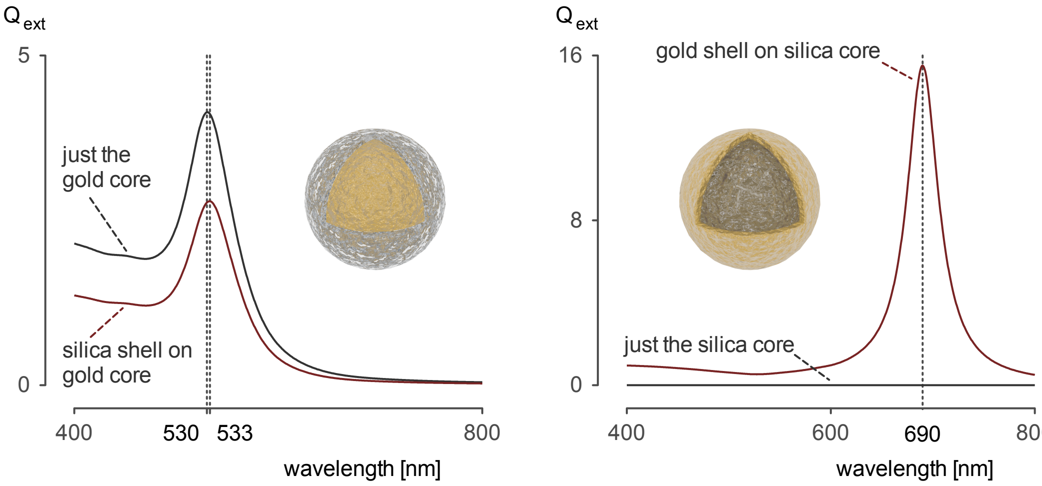

Figure 1.3.9.. The plasmon resonance position of a gold nanoparticle with a diameter of 50 nm will be damped and slightly red-shifted upon the attachment of a 5 nm thick silica shell. Pure silica particles do not absorb light in the visible region of the light. Whereas particles with a 5 nm gold shell on a 50 nm silica core show a strong resonance at a wavelength of 690 nm.

A dielectric shell on a metal nanoparticle will cause a damping of the particle plasmon resonance. For a gold nanoparticle with a diameter of 50 nm and a silica shell of 5 nm a slight red-shift of 3 nm and a decrease in the extinction efficiency of about 40 % can be found compared to the gold nanoparticle without a shell (see figure 1.3.9 left).
The response of a 50 nm silica particle in the visible region of the electromagnetic spectrum is negligible. However, a 5 nm thin shell of gold causes a very strong resonance at a wavelength of 690 nm (see figure 1.3.9 right). Since nanoshells have an inner and an outer gold surface their plasmon can be explained by a hybridization theory. The plasmon of a solid gold nanosphere will represent the outer surface and a the plasmon of a hollow structure in a gold surrounding will represent the inner surface. These two plasmon modes can hybridize into a plasmon with lower energy and one with higher energy. The one with higher energy is a so called “dark state” and cannot be observed in light scattering experiments.[24] Nevertheless, the plasmon mode with lower energy is extremely strong and is red-shifted compared to a particle plasmon of a solid gold nanoparticle.

1.3.6. Coupled gold nanoparticles

Among all the different geometries that one can think of, a dimer made of two spherical nanoparticles is of cause the most simple form of an assembly. To understand the effects that are caused by the interaction of different particles it seems natural to start with the discussion of the optical properties of a dimer. The near- and far-fields of the different gold nanoparticle dimers have been calculated in the frame of the Generalized Mie Theory, using the GMM-FIELD program written by Ringler and the GMM programm by Xu, respectively.[26;27]
It can be seen that the coupling of the particle plasmons increases significantly for separations smaller than one-tenth of the particle diameter (see figure 1.3.10). The near-field in the gap will be enhanced by almost two orders of magnitude compared to the single particle case. These strong field enhancements are often referred to as “hot spots”. For particle separations smaller than approximately one nanometer, the electric field can not be evaluated classically because of quantum size effects that become important for these separation distances.[28]

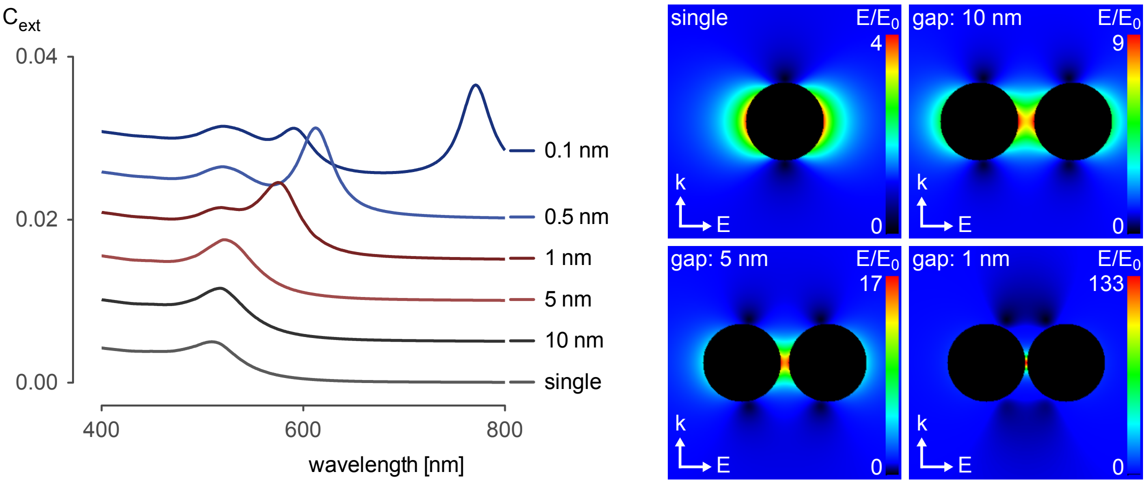

Figure 1.3.10.. A decrease of the gap between two 50 nm gold nanoparticles causes a red-shift of the dipolar plasmon resonance position and increases the absolute value of the local electric field in the gap considerably. The near-field has been evaluated for an excitation wavelength of 633 nm.

1.4. Simulation of the optical properties of non-spherical nanostructures

The Maxwell equations can only be solved analytically for spherical particles, using the procedure proposed by Mie. Although there are extensions of this approach to also treat different geometries like ellipsoids and infinite cylinders, most of the structures found in modern nanoscience can not be modeled. If there is no analytical solution for Maxwell's equations for a complex structure then they have to be solved numerically. Many different methods have been developed during the past decades to model the optical far- and near-field properties of arbitrary particle geometries.
With the use of modern computer technology these numerical methods become available for many scientists and are therefore widely used. Nowadays in computational electrodynamics various approaches to approximate Maxwell's equations for the propagation of electromagnetic fields in the presence of arbitrary shaped objects are known. Common techniques to treat scattering problems in nanotechnology are the "Finite Differential Time Domain" (FDTD) method, the "Finite Elements Method" (FEM), the "Boundary Element Method" (BEM), the "Multiple Multipole" (MMP) method and the "Discrete Dipole Approximation" (DDA) method. All methods include a discretization of the modeling space. Depending on the method and the

accuracy needed to solve the problem, the number of grid points is considerably high. Consequently there is a large demand on computer memory and CPU power. Therefore many problems can just be solved within an acceptable time by making use of super computers, parallel computers or high performance clusters. In the following part the main ideas of the three most common methods in computational electrodynamics regarding their application in plasmonics will be discussed.

1.4.1. Finite-difference time-domain method

The original method was already introduced by Yee in 1966 but not before 1980 it was referred to as FDTD method.[29;30] From Maxwell's equations it is known that the E-field depends on changes in the H-field and vice versa (see section 1.1.2). In FDTD the modeling domain is divided into grid points. At each point the E- and H-field is calculated iteratively over time, whereas the derivatives of the Maxwell's equations are approximated by finite differences. From the final steady state solution one obtains the E- and H-field at each point in the modeling space.

In principle all materials and shapes can be treated with FDTD methods, as long as they can be represented by their dielectric function. Additionally to the object of interest and the surrounding medium, appropriate boundaries of the simulation space have to be applied to prevent reflections of the electromagnetic radiation from the boundaries. Usually this is realized by introducing either absorbing boundary conditions (ABC) or a "perfectly absorbing" material in a so called perfectly matched layer (PML).

Since the FDTD algorithm just produces a near-field solution, a time-consuming post processing might be needed to obtain far-field information. Besides, the FDTD method is very powerful and its sources of error are well understood. The possibility to use non-uniform meshing further extends its strength, as a large simulation space can be used and still have a very fine meshing in the areas of large field gradients.

There are several software implementations of this method available. LUMERICAL is probably the most widely used commercial software. Besides there exist a couple of open source implementations, whereas the best known code developed at the MIT is called MEEP.[31]

1.4.2. Boundary elements method

The boundary element method (BEM) or also referred to as method of moments (MOM) is a numerical technique to solve linear partial differential equations. The method can be used in electrodynamics to solve Maxwell's equations in frequency space. In simulations applying the BEM a discretization of the whole space is not necessary. Instead the particle boundaries are discretized as a two-dimensional mesh of vertices and faces. On this mesh the integral equations are solved to obtain surface charges and surface currents. All internal and external fields are determined by this charges and currents and therefore it is possible to calculate numerically the near- and far-field properties.

A freely available software to solve electromagnetic scattering problems using the BEM approach has been introduced by Hohenester and colleagues from the University of Graz. They implemented a BEM code as a Toolbox for MATLAB. The program is very easy to use, but is limited in possibilities of target generation and is also very slow due to the incorporation of the code into the MATLAB framework.

1.4.3. Discrete dipole approximation

This method has been originally developed to model scattering properties of interstellar grains. It, however, became very popular to be used in modern nano-plasmonics. A big advantage of this method is that only the object under consideration has to be discretized and the embedding medium can be implemented by its dielectric constant. Therefore it saves memory compared to methods where the whole simulation space has to be discretized.

In the DDA the target is represented by a cubic array of polarizable point dipoles. The dielectric function of the target determines the polarizability α_i of each point. Now the induced dipole P_i has to be evaluated for every point in the array. Therefore a quasi self-consistent field approach is used. The induced dipole depends on the local electric field $E_{\mathrm{loc},\,i}$.

$$P_i = \alpha_i E_{\mathrm{loc},\,i} \tag{1.4.1}$$

The local field at each point is a superposition of the incoming field of the excitation source and of the combination of the dipole fields of all other elements. Once all induced dipoles are determined it is possible to calculate a variety of far-field properties like scattering, absorption and extinction cross sections as well as the near-field.

Draine and Flateau developed the most popular implementation of the DDA.[32;33]

The code is open source and has been written in FORTRAN. First published in 1982 the code has ever since been extended and updated. Several discretization routines are included as well as the capability to treat structures with one dimensional or two dimensional periodicity.

1.5. Enhancement phenomena due to plasmonic structures

One of the most relevant properties of plasmonic nanoparticles is the large enhancement of the electric field in the vicinity of these structures. They can potentially be used to increase the efficiencies of both light-emitting and light collecting devices, like LEDs, OLEDs and solar cells. Besides an improvement of the sensitivity of spectroscopic methods, especially Raman and fluorescence spectroscopy, could be achieved by the specific employment of noble metal nanoparticles.

1.5.1. Surface-enhanced Raman scattering

In 1974, during the collection of Raman spectra of pyridine on rough silver electrodes, Fleischmann found an enormous increase in intensity, which he attributed to the large surface area and the resultant high coverage of adsorbed molecules.[34] It was not until three years later, as van Duyne interpreted the results correctly and proposed a surface enhancement mechanism.[35] The tremendous development of nanotechnology and the huge number of possibilities to control the particle size and geometry gave rise to many applications of the SERS effect.

Nowadays, the enhancement mechanism is mostly understood. The Raman scattering intensity is known to be proportional to the square of the induced dipole moment. The dipole moment depends on the polarizability and the electric field strength (see equation 1.5.1). Therefore an increase in intensity is possible via either changing the polarizability of the Raman scatterer or the surrounding electric field.

$$P \propto |p|^2 = |\alpha E_{\mathrm{loc}}(\omega)|^2 \tag{1.5.1}$$

The interaction of electromagnetic radiation and metal nanostructures will cause a particle plasmon. Especially at the resonance frequency this electron oscillation will generate high electric fields in the vicinity of the metal structures. The increased electric field strength affects the Raman process twice. First a photon of the exciting electromagnetic wave will be absorbed. The corresponding intensity of the generated dipole will be proportional to $|E_{\text{loc}}|^2$. The oscillation of this dipole causes now the emission of the Raman radiation. Since Raman scattering is a one-photon process and assuming that the energy of the emitted photon is close to the energy of the exciting photon, the second part of the overall process also depends on $|E_{\text{loc}}|^2$. This gives a final dependence of the Raman scattering intensity on $|E_{\text{loc}}|^4$ for a Raman scattering molecule placed in the local electric field E_{loc}. Because of its origin this part of the enhancement is called the electromagnetic part and usually contributes most to the overall SERS effect.

If molecules are chemically adsorbed on the surface of a metallic particle the molecule and the metal wave function can overlap. This causes a charge transfer from either the molecule to the metal or vice versa depending on the relative position of the energy levels. The charge transfer causes a change in the polarizability, which will effect the intensity of the induced dipole and hence the overall Raman scattering intensity. Commonly this is referred to as the chemical part of the SERS effect.

1.5.2. Surface-enhanced fluorescence

Since fluorescence and Raman scattering are completely different processes, the origins for the SERS effect cannot be applied one-to-one to explain enhanced fluorescence. Fluorescence is a two photon process, composed of an absorption and an emission. For the absorption the same dependence on the local electric field found for SERS can be applied, because they are in principle equal. However, the emission in fluorescence is a spontaneous emission and not a dipole emission like in Raman scattering. For a spontaneous emission the Einstein coefficient A predicts the lifetime of the excited state. The lifetimes can be changed due to the local electric field. Furthermore the non-radiative lifetime can also be changed because of a charge transfer from the molecule to the metal, which in principle will result in the quenching of the fluorescence.

In conclusion, this means that the first part, the absorption of a photon, can be directly influenced by the local electric field, whereas for the second part, the spontaneous emission, just the lifetimes and hence the quantum yield of the fluorescence process are affected. For fluorophores that in the non-enhanced case show high quantum yields already, a further improvement due to plasmonic structures is almost impossible.

2. Aqueous gold nanoparticle syntheses - improvements and new insights

In this chapter the focus will be on the aqueous synthesis of gold nanoparticles. First a new seeded growth method to obtain gold nanoparticles over a large range of sizes will be presented. The method produces particles with uniform spherical shape and narrow size distributions. Using ascorbic acid as a reductant and sodium citrate as stabilizer biocompatible and easy to exchange substances have been utilized. The investigation of the growth process via TEM measurements revealed the formation of small gold clusters on the surface of the seeds, which subsequently grow and result in a "blackberry-like" intermediate shape of the gold nanoparticles. Applying heat caused an intraparticle ripening process, which finally leads to a smooth spherical particle shape. Furthermore, the optical properties of the resulting gold sols are compared to theoretical calculations using Mie theory and the DDA method, respectively.

The second part of this chapter deals with the influence of the chloride ion concentration on the final particle size and morphology of gold nanoparticles synthesized in aqueous media. An increase in the chloride ion concentration in the classical Turkevich synthesis resulted in larger and elongated particles. A complete removal of the chloride ions from the reaction mixture, by changing the gold precursor from hydrogen tetrachloroaurate to gold hydroxide, enabled the access to particle morphologies other than spherical. The formation of decahedral, "desert-rose-shaped" and star-shaped particles has been possible.

2.1. Seeded growth approach for uniform gold nanoparticles*

Gold sols have been known and used for centuries. Their optical properties are well understood and during the last decades they have become widely used as model systems due to their ease of preparation and superior stability. Although the literature offers a wide variety of different gold nanoparticle synthesis,[37–41] some problems still remain to be overcome, particularly in preparing larger particles. Shape control is a very important field for the design of plasmonic structures, since the shape has a stronger influence on the optical properties than particle size.[42] Especially in the field of the formation of anisotropic gold nano structures a lot of work has been done.[43–49] The variety of shapes includes spheres, rods, wires, prisms, cubes, stars, tetrapods and others. Most of the approaches are performed in aqueous media and using CTAB (cetyltrimethylammonium bromide) as the stabilizer. For the formation of bigger structures, all of these methods are very likely to lose shape specificity, and time-consuming cleaning steps become necessary.

2.1.1. An overview of seeded growth methods in the literature

Focusing on seeded growth approaches for the synthesis of spherical gold nanoparticles leads again to many different methods that have been published. Starting from a synthesis for gold nanoparticles with small diameters between 2 nm and 8 nm and excellent size distributions in toluene[50] all the way to approaches using gum arabic as the stabilizer that are capable of producing particles with diameters of many hundreds of nanometers up to several microns in diameter.[51;52] Another method by Jana et al. covers sizes of between 5 nm and 40 nm in particle diameter again using CTAB as the stabilizer and sodium borohydride as the reductant.[53] Combining CTAB as the stabilizer and ascorbic acid as the reductant, a valuable method was developed in the group of Liz-Marzan, producing particles with diameters between 12 nm and 180 nm.[54] However, this method includes a post synthetic clean-up to obtain spherical particles only.

Perrault proposed a synthesis using the weak reductant hydroquinone, which produces particles in the size regime of 50 nm to 200 nm in diameter.[55] Besides the relatively high polydispersity and low shape stability for bigger particles, this method produces benzoquinone, which is toxic and hazardous to the environment. A so

---

*Parts of this section have already been published.[36]

called “one step seed mediated growth method” was developed by Niu and is capable to deliver gold nanoparticles with sizes between 30 nm and 150 nm utilizing the reducing agent 2-mercaptosuccinic acid.[56] One of the most widely used procedures of growing large gold nanoparticles is that of Natan’s group,[57] using hydroxylamine as the reducing agent. However, by the third growth step this procedure yields a significant number of shapes which are different from spheres. Other methods which are using ascorbic acid, as reported here, have even more problems with the generation of multiple shapes.[58;59] Especially in multistep seeded-growth procedures, it is very common to obtain rods and polyhedral forms in addition to spherical particles.

Although a variety of procedures to produce spherical gold nanoparticles is known, none of these methods can provide all of the features of the here presented new method, like a large range of available sizes, non-toxic and easy to exchange stabilizer and reductant, very good size distributions, no need for post-synthetic clean-up and finally the simplicity of the synthesis.

Despite of a narrow size distribution and a simple synthetic procedure, current research interests are mostly based on post processing of the nanoparticles including a surface modification. The growing field of biological and medical applications[60;61] as well as diagnostics and detection[62] are just a part of examples where easy to exchange ligands are needed. Li et al. recently published a new sophisticated approach of the preparation of SERS-substrates called SHINERS[20] (shell-isolated nanoparticle-enhanced Raman spectroscopy) also utilizing citrate capped gold nanoparticles. Furthermore many core-shell nano-architectures for example for fluorescence enhancement[63] are based on this kind of gold nanoparticles. Another field of application, for the here presented nanoparticles, could be the specific formation of superstructures and artificial molecules through certain and controlled surface functionalizations.[64]

In the light of the wide field of applications, it seems to be useful to have nontoxic and easy to substitute molecules on the surface of the resulting particles. Therefore a biocompatible reductant as well as a weakly bound stabilizer have been chosen. It should be pointed out that prior to this work there has no comparable method been reported in the literature, which covers such a huge size range including the simplicity of the method and the advantages provided by the properties of the reducing and the stabilizing agents. Especially in studies utilizing differently sized gold nanoparticles, it is of great convenience to have all particles produced via the same method.

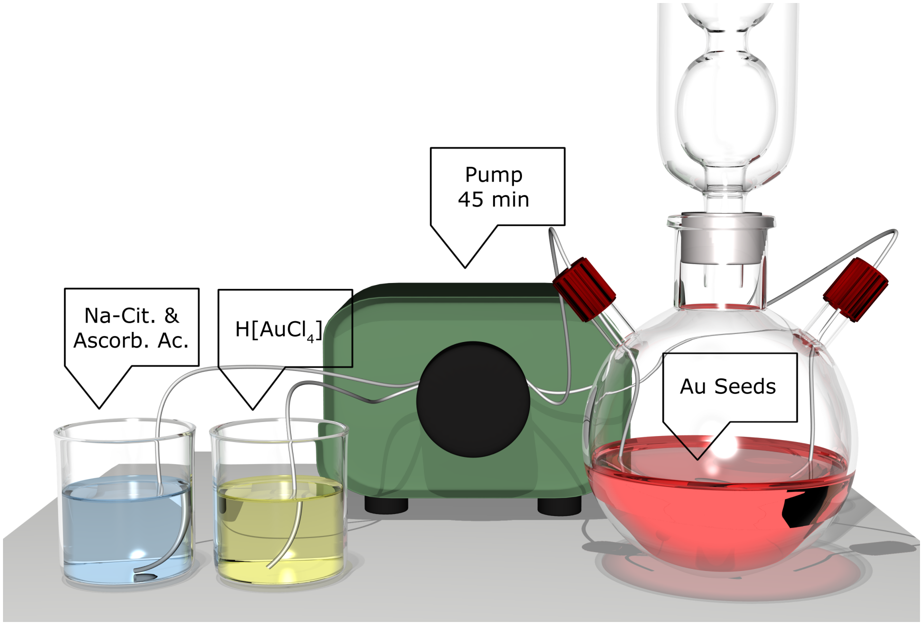

Figure 2.1.1.. With the help of this special experimental setup it was possible to add the gold precursor and the reducing agent solutions separately and very slowly, which was crucial to obtain a homogeneous growth.

2.1.2. Experimental procedure

Seed particle solutions were prepared by the standard citrate reduction method.[17] Briefly, 2.5 ml of a H[AuCl$_4$] solution (0.2 % w/v) in 50 ml of water were heated to boiling and then 2 ml of sodium citrate solution (1 % w/v) were added quickly under vigorous stirring. The solution was kept boiling for five minutes and was then allowed to cool down.

The general procedure for growing the seeds was as follows. A certain amount of seed solution was diluted to 20 ml and placed into a three-necked flask. 10 ml of the precursor solution A, containing H[AuCl$_4$] , and 10 ml of the reducing solution B, containing trisodium citrate and ascorbic acid, were added separately at room temperature through teflon tubes via a peristaltic pump under vigorous stirring over a time of about 45 minutes (see figure 2.1.1). Directly after the addition was complete, the mixture was refluxed for about 60 minutes. Finally the solution was allowed to cool down and UV/Vis and TEM investigations were carried out.

Solution A was prepared by diluting a H[AuCl$_4$] stock-solution (0.2 % w/v) to 10 ml and solution B was prepared by diluting a mixture of an ascorbic acid stock-solution (1 % w/v) and a sodium citrate stock-solution (1 % w/v) again to 10 ml. The relative volume ratios of all three stock-solutions were always 8:2:1. The synthesis of the 150 nm gold nanoparticles was for example via three growth steps.

In the first step 3 ml of seed solution, 2 ml of $H[AuCl_4]$ stock-solution, 0.5 ml of ascorbic acid and 0.25 ml of sodium citrate stock-solution have been used. Afterwards 4.5 ml of the resulting sol was used in the next step with again 2 ml of $H[AuCl_4]$ stock-solution, 0.5 ml of ascorbic acid and 0.25 ml of sodium citrate stock-solution. In the third growth step 20 ml of the last sol, 8 ml of $H[AuCl_4]$ stock-solution, 2 ml of ascorbic acid and 1 ml of sodium citrate stock-solution have been used. By knowing the seed-particle diameter and concentration and assuming a complete turnover with no formation of additional seeds, one can calculate the required amount of gold precursor to achieve a certain particle diameter. Simulations of UV/Vis spectra were done using standard Mie theory. Therefore a modified MATLAB script, on the basis of that by Mätzler[65], which itself is adapted from the FORTRAN code given by Bohren and Huffmann,[5] has been used. The DDA simulations have been done using the DDSCAT code by Draine and Flatau.[32] For gold the dielectric function reported by Johnson and Christy[9] and for water that by Segelstein[66] have been used.

2.1.3. Uniform gold nanospheres and their properties

From the electron microscope images of differently sized gold nanoparticles it can be seen that they are of spherical geometry and have a very low polydispersity. The 30 nm particles have been synthesized using only one growth step, whereas the 69 nm and the 118 nm particles are made using two growth steps and the 150 nm and 294 nm particles were prepared using three growth steps. Even for the largest particles a uniform shape with smooth surfaces and narrow size distributions could be found. The formation of polyhedral shapes is rare and the one cuboctahedral particle in the bottom right micrograph in figure 2.1.2 is included just for completeness. All particles displayed good long-term stability ($>$ 1 month). Although due to their mass the largest particles settle down quite quickly. However they could be redispersed by short sonication with ease.

During the process of developing this synthesis, many reducing agents like just ascorbic acid, just sodium citrate, hydroxylamine and different carbohydrates have been used. However, the by far best results were achieved with the here presented mixture of ascorbic acid and sodium citrate. The temperature for the synthesis has also been carefully optimized.

In order to determine whether the formation of larger particles is due to the aggrega-

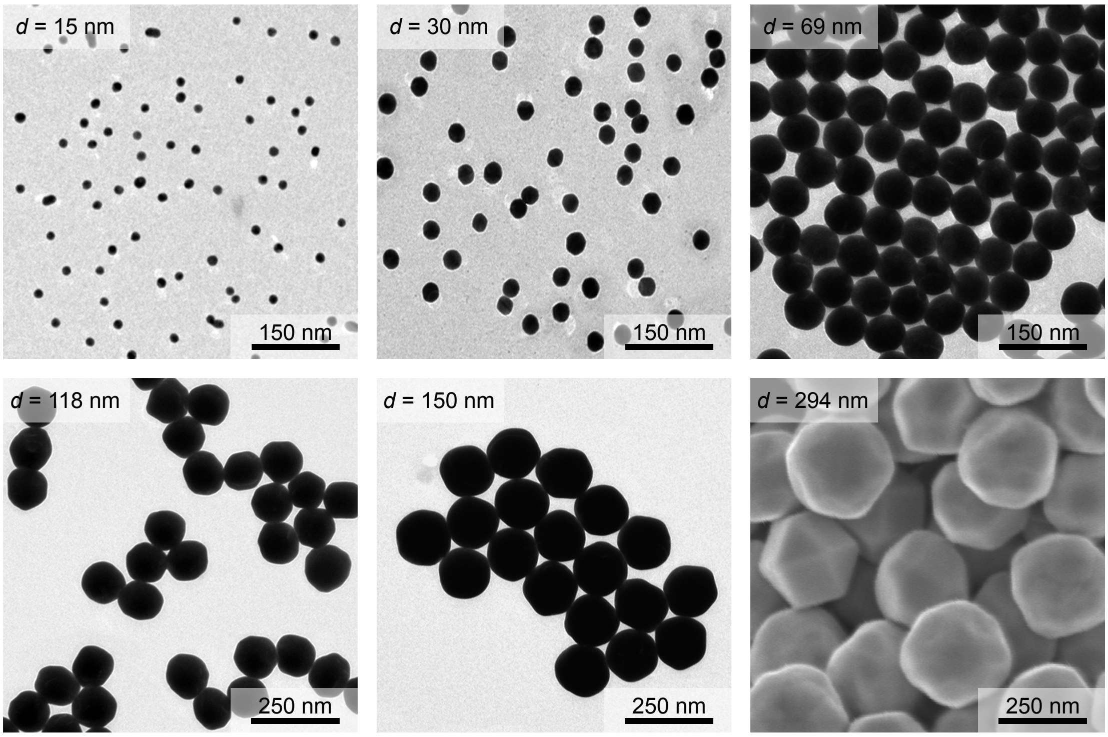

Figure 2.1.2.. TEM and SEM micrographs reveal that the gold nanoparticles obtained with the seeded growth method are of uniform shape and have a very narrow size distribution.

tion of small particles or due to the growth of separated particles, the course of the synthesis was monitored by TEM (see figure 2.1.3). It is observed that many individual nucleations occur on each particle which subsequently grow until the addition of solutions A and B is finished. The resulting particles show a “blackberry-like” morphology. Upon heating of the solutions to their boiling point, a reorganization takes place which finally leads to particles having smooth surfaces.

At this point this feature should be emphasized, since in previous investigations concerning platinum nanoparticles, the surface roughness was preserved even after heat treatment.[67] This surface roughness was responsible for altering the optical response of the particles and could only be accounted for by incorporating a core-shell geometry into the model for calculating the UV/Vis spectra. These corrections are not necessary in the case of the gold nanoparticles presented here.

The transformation from the “blackberry-like” shape to the smooth spheres is believed to be due to minimizing the surface energy of the nanoparticles similar to a Ostwald ripening process. A similar intraparticle ripening process has been reported by Zhao

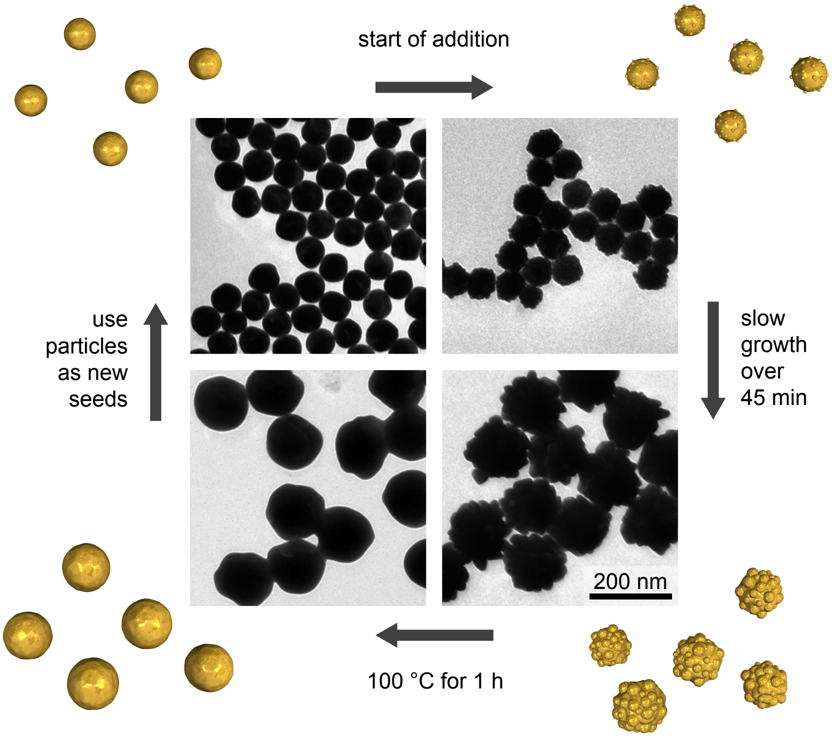

Figure 2.1.3.. During the growth procedure small nucleation sites are formed on top of the seed particles. These sites subsequently grow until the addition of the precursor solutions is finished. A final heating step leads to a smooth particle surface.

et al. in their work about gold nanoflowers.[68] Since the strength of the metal bond in gold is weaker than that in platinum, this atomistic reorganization process is much faster for gold than for platinum nanoparticles.

The most essential part of our synthesis is the slow and separate addition of solutions A and B. Direct and fast injections always lead to the formation of different sizes and multiple shapes such as rods and triangular prisms. Spherical particles with a narrow size distribution could be produced without heating the solution to its boiling point after the addition of A and B was terminated. However, these materials exhibited very rough surfaces (see figure 2.1.3) and tended to coalesce very quickly.

Two limiting factors were observed during the evaluation of the synthetic procedure and could be estimated from experimental results. First, the seed particle concentration, and therefore the total active metal surface, must exceed a certain threshold (about 10^8 particles/ml). Otherwise additional nucleation and non-uniform particle growth takes place. Second, the gold precursor concentration should be below a certain threshold in order to prevent the formation of polyhedral particles. It is believed that these geometries are the result of high chloride concentrations since they are mostly observed for third or higher order growth steps. The influence of halide ions on the growth mechanism and the final particle shape has already been reported.[49] The observations reveal a maximum chloride concentration of about 15 mM to ensure that spherical particles are being formed. This limit might be overcome by washing the gold sols via dialysis but a deeper investigation of this phenomenon will be part of the next section. Evaluating the optical properties of the gold sols reveals that the experimentally obtained and simulated UV/Vis spectra, shown in figure 2.1.4, are in very good agreement. The expected red-shift of the dipolar plasmon resonance for increasing particle diameters could be observed as well as the appearance of the quadrupolar mode at 542 nm for the 150 nm particles and an octupolar mode at 560 nm could be observed for the 294 nm particles.

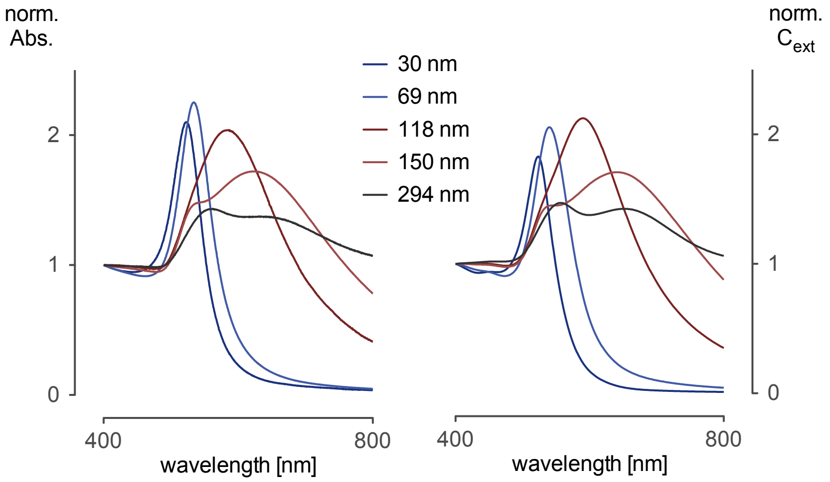

Figure 2.1.4.. The high quality of the particles can also be seen by the comparison of the experimental and the theoretical UV/Vis spectra which are in very good agreement.

However, a discrepancy emerges between the measured and the simulated plasmon resonance positions. Throughout, the measured positions are shifted to higher energies with respect to the simulations, showing an increasing deviation with increasing particle diameter, whereas the deviation of the position of the dipolar mode is larger than that of the position of the quadrupolar and octupolar modes, respectively.

It is well known that experimentally found plasmon positions can deviate from the calculated ones because of additional surface layers, surface defects or a deviation from the ideal spherical shape of the nanoparticles. However, normally these shifts are observed in the opposite direction towards the red. For small particles this deviation can be explained by the changing of the dielectric function of the particles, compared to that of the bulk, because of a change in the electron concentration in the particles (see chapter 1). However, this explains neither the increasing deviation for larger particles nor the surprising difference between the deviations of the dipolar, quadrupolar and octupolar modes.

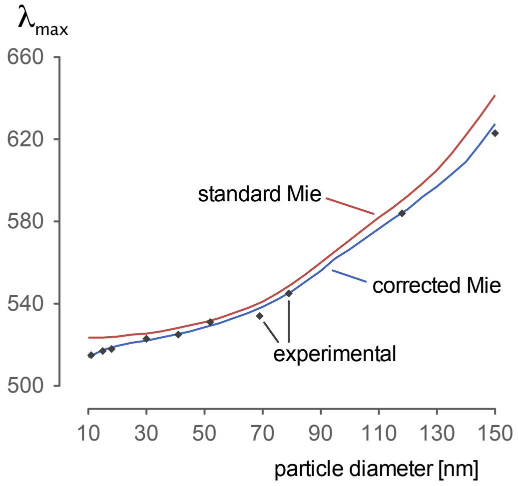

Figure 2.1.5.. An adjustment of the dielectric function of gold and taking account for the size distribution of the particles leads to a much better consistence of the dipolar plasmon resonance positions obtained experimentally and those predicted by theoretical calculations.

The explanation for these phenomena could be found by taking into account the experimentally derived size distributions of the particles and adjust these slightly to give the best fit. Including a correction for the electron concentration, the mean free path of the electrons and the size distribution of the particles, the plasmon resonance positions coincide much more closely with the experimentally found values (see figure 2.1.5 and table 2.1.1). Like already discussed in chapter 1 it was found that assuming a certain polydispersity this changes very little for small particles but becomes more and more significant for increasing sizes, especially if the absorbance is mainly determined by scattering, rather than by absorption. Obviously, the influence of the size distribution on the optical properties is far more intense for particles with a diameter of 300 nm than for that with a diameter of 30 nm. Furthermore, it was found that the change of the absorbance for the particles with a diameter of 300 nm is mainly originated from the change in the scattering part and that the absorption part changes very little. The size distributions also lead to larger shifts for the dipolar mode than for the quadrupolar and octupolar modes, respectively.

Table 2.1.1.. By correcting the dielectric function for the mean free path effect and the electron concentration and taking into account the particle size distribution the plasmon resonance positions calculated theoretically are in very good agreement with those found experimentally.

particle diameter [nm]	type	dipolar mode [nm]	quadrupolar mode [nm]	octupolar mode [nm]
30	exp.	523	-	-
	Mie	526		
	Mie corr.	522		
69	exp.	534	-	-
	Mie	540		
	Mie corr.	538		
118	exp.	584	-	-
	Mie	591		
	Mie corr.	585		
150	exp.	623	542	-
	Mie	642	545	
	Mie corr.	624	545	
294	exp.	-	641	560
	Mie		653	557
	Mie corr.		639	560

The development of the optical properties during the intraparticle ripening

Especially for larger particles the shape has a significant influence on their optical properties. Although the intermediate shape, found during the formation of the spherical gold nanoparticles, also has a spherical geometry, the surface show a considerable roughness. In order to match the structural transformation with the changes in the optical properties, DDA simulations have been conducted.

Therefore the particle morphology found during TEM investigations was reproduced by a large central sphere on which several small hemispheres have been arranged. The structure obtained was then discretized for the DDA simulations to give a dipole separation of about one nanometer. To simulate the ripening process, the radius of the larger sphere in the center has been increased successively until the overall geometry was a flat sphere (see figure 2.1.6). The volume of the structures was equivalent to a sphere with a diameter of 70 nm and was kept constant to ensure an intraparticle ripening process. For the simulations the spheres have been represented by the dielectric function of gold from Johnson and Christy[9] and the surrounding medium was characterized by a refractive index of 1.33 for water.

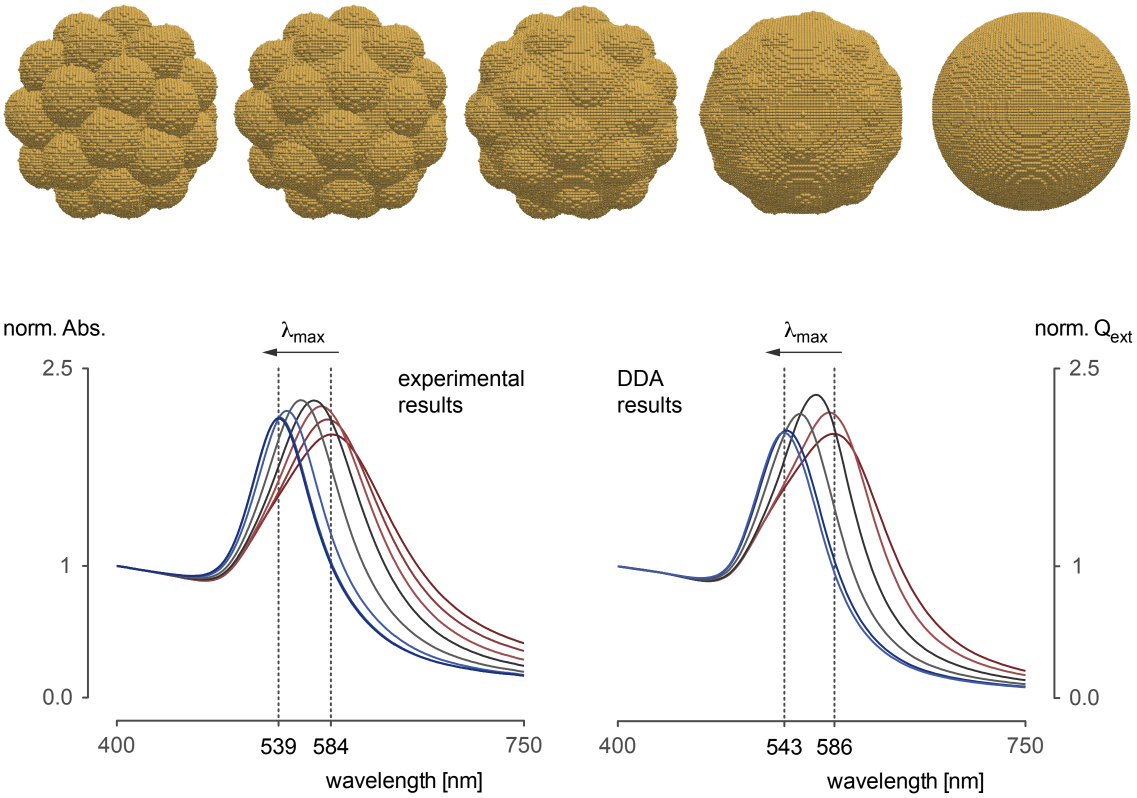

Figure 2.1.6.. Comparison of the development of experimental and theoretical UV/Vis spectra during the intraparticle ripening.

A comparison of the experimentally determined UV/Vis spectra and the results from the DDA simulations show a very good agreement (see figure 2.1.6). The plasmon resonance position was found to undergo a blue shift of about 45 nm during the intraparticle ripening process. It can also be seen that the width of the plasmon band decreases during the development of both the experimental and the theoretical spectra. Furthermore the slight shift towards lower energies of the theoretically obtained resonance positions compared to the experimental ones can be explained with the same arguments like already stated above since there were no corrections for the particle size distribution, the confinement of the free mean path of the electrons and the charge of the particles, respectively. Including all these corrections for the calculation of the spectrum of gold nanoparticles with a radius of 70 nm, a plasmon resonance position of 539 nm can be found which exactly matches the position found experimentally.

For both experimentally and theoretically obtained spectra the plasmon resonance intensity increases during the first half of the ripening process and finally decreases. Due to the reorganization of the particle surface, the surface damping is decreased during the ripening and hence the resonance intensity will increase. But since this is also accompanied by a blue shift of the resonance position, the part of the spectrum where the resonance is located becomes more and more dominated by interband transitions. Again this introduces a damping and therefore the intensity of the resonance decreases.

Overall the excellent consistency of the experimental UV/Vis spectra and the simulated ones confirms the proposed intraparticle ripening process.

2.1.4. Determination of the gold nanoparticle concentration from UV/Vis spectra

For planning the synthesis of larger particles using the seeded growth approach, the seed particle concentration should be known as accurately as possible. But also for biological applications, for example in the determination of cellular uptakes of nanoparticles, in procedures where the surface has to be modified and in many more areas it is more than useful to have an easy and accurate tool to determine the concentration of gold nanoparticles in solution.

Haiss proposed a simple procedure to determine the size and the concentration of gold nanoparticles in aqueous solutions.[69] Therefore he calculated the extinction cross-section of the gold nanoparticles following Mie's theory and corrected the dielectric function of gold for the mean free path effect. From the extinction cross section and the measured absorbance he calculated the gold concentration and compared the results with the initially used gold concentration. Later Khlebtsov extended this work by discussing the effect of different experimentally determined dielectric functions of gold and incorporating also non spherical particle geometries using T-matrix simulations.[70] Earlier he already proposed an empirically determined calibration curve to obtained an equivolume diameter of the gold nanoparticles in a solution.[71] However, all of these works give no comparison of their results to different techniques used for the determination of the gold concentration.

In this section the concentrations of gold nanoparticle solutions obtained from UV/Vis spectra will be compared with results from ICP-OES investigations. The concentrations obtained from UV/Vis spectra will be determined following the method proposed by Haiss. Additionally the extinction cross-section of the gold nanoparticles will be determined by correcting the dielectric function not only for the mean free path effect but also for the change in the electron concentration like presented in chapter 1. In the second method the particle size distribution of the gold colloids will also be included.

With the aid of the Beer-Lambert law it is very straightforward to calculate the concentration of an analyte from the measured absorbance. Only the wavelength and substance specific extinction coefficient has to be known.

$$E = -\lg \frac{I}{I_0} = \epsilon_\lambda \cdot c \cdot l \tag{2.1.1}$$

The ratio of the intensity of the incident radiation I_0 and the intensity of the radiation after passing the sample I depends on the extinction cross-section C_{ext}, the path length l and the volume density of the nanoparticles N.

$$\frac{I}{I_0} = \mathrm{e}^{-C_{\mathrm{ext}} \cdot l \cdot N} \tag{2.1.2}$$

From the last two equations the extinction coefficient ϵ_λ can be evaluated to

$$\epsilon_\lambda = \frac{C_{\mathrm{ext}} \cdot N_{\mathrm{A}}}{\ln 10} \tag{2.1.3}$$

with $N_{\mathrm{A}} = N/c$ being Avogadro's constant.

Knowing the particle size of the gold nanoparticles in the solution the extinction cross-section can be calculated from Mie's theory. The concentration that can be determined for a certain absorbance measured will be the concentration of particles per volume. To convert this concentration to a molar concentration of the total gold in the sample, the number of gold atoms per particle needs to be known. This can easily be calculated from either the lattice parameters of the gold unit cell or the molar mass and the density of gold. Both methods lead to the same result and the number of gold atoms n_{at} in one particle with radius R in nanometer will be:

$$n_{\mathrm{at}} = 247 \cdot R^3. \tag{2.1.4}$$

Table 2.1.2.. Comparison of the gold concentrations obtain from different methods.

particle diameter	▬ Haiss ▬ ICP-OES ▬ this work	gold concentration in mM/l
4 nm	Haiss	0.274
	ICP-OES	0.183
	this work	0.252
20 nm	Haiss	0.254
	ICP-OES	0.223
	this work	0.231
36 nm	Haiss	0.224
	ICP-OES	0.205
	this work	0.213
67 nm	Haiss	0.150
	ICP-OES	0.148
	this work	0.150

It can be seen that the concentrations determined from UV/Vis spectra overestimate the actual gold concentration obtained from ICP-OES investigations (see table 2.1.2). However, including corrections for the electron concentration and the particle size distribution gives better results than without. The largest mismatch of the actual gold concentration and the ones obtained from absorbance measurements was found for very small particles. It is well known that the optical properties of metal nanoparticles in this size regime are significantly influenced by quantum size effects.[28;72] Since quantum effects have not been included in the present study, this deviations are not surprising.

The amount of the overestimation of the concentrations obtained from absorbance measurements decrease for increasing particle diameters. Therefore it is unlikely that the overestimation is due to matrix effects, which should be the same for all samples. Perhaps the damping due to the confinement of the mean free path of the electrons is smaller than estimated by the theory applied. This would also explain the very good agreement of all three methods for the concentration of the largest gold nanoparticles where the mean free path effect is not significant anymore.

2.2. The role of chloride in gold nanoparticle syntheses

This year a comprehensive study of the role of halide ions in the seed mediated synthesis of gold nanostructures was published by the Mirkin group.[73] They found a significant influence of the halide ions both on the reaction rate and on the passivation of certain surfaces and hence a strong dependence of the final particle shape on the halide ion concentration. Already four years earlier they could attribute the formation of differently shaped gold nanoparticles while using the same synthesis protocol to the different iodide residues in CTAB from different suppliers.[49] Another work showed the importance of the chloride ions on the ripening of gold nanoflowers into gold nanospheres.[68] Until now the role of halide ions is not completely understood in all systems used for noble metal nanoparticle synthesis.

Within this section the influence of chloride ions on the particle shape in one-step syntheses of gold nanoparticles and on the ripening process in the seed mediated procedure presented in the previous section will be discussed.

2.2.1. More chloride than usual

In this part it will be shown, that an increase of the chloride ion concentration in a classic citrate reduction protocol will strongly affect the particle size, shape and particle size distribution. Furthermore it was found that an increase in the chloride ion concentration promotes the intraparticle ripening process.

Effect of added chloride ions in the seeded growth synthesis

During the work on a seeded growth approach for large monodisperse gold, presented in the previous section, it was found that a final heating step was crucial to obtain a smooth particle surface. During this step an intraparticle ripening took place where the gold atoms on the outside rearranged to minimize the surface area of the particles. Without this heating procedure no surface smoothing could be observed.

However, by adding a small amount of chloride ions during the synthesis (5 mM final concentration) and stirring the solution over night, particles with almost the same optical properties as obtained from the conventional method could be synthesized.

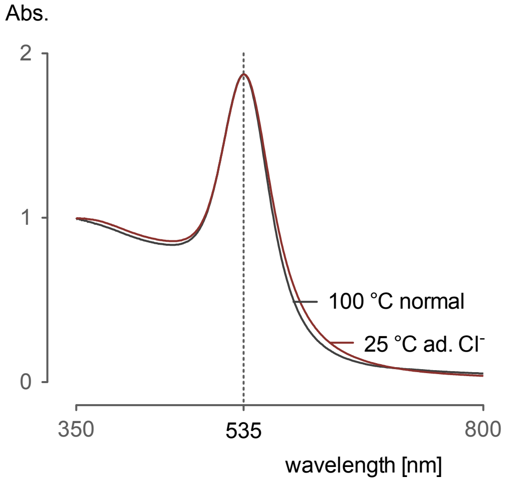

Figure 2.2.1.. For an increased chloride concentration during the seeded growth synthesis of gold nanoparticles the intraparticle ripening took place at room temperature already leading to particles with almost the same quality compared to those prepared conventionally.

The particle morphology can be directly connected to the UV/Vis spectra of the respective gold sols like discussed already. Therefore one can conclude that the increased concentration of chloride ions accelerates the intraparticle ripening procedure at room temperature.

It is known that during an intraparticle ripening process of CdSe nanocrystals atoms move from one facet to another within the same particle.[74] Assuming a similar mechanism for the ripening of the gold nanoparticles leads to the conclusion that the chloride ions promote the movement of the gold surface atoms. It seems very likely that the chloride ions bind to the gold surface atoms and hence lower the binding energy to the rest of the lattice which makes a movement easier.

Effect of added chloride ions in the standard citrate reduction method

Although known for almost 60 years, the classical Turkevich method[16] to produce citrate stabilized gold nanoparticles is still under tremendous discussion. Over the last years the influence of the gold precursor to citrate ratio, the pH of the solution, different reaction temperatures and even the order of mixing the precursor solutions have been under investigation.[17;75–78] However, there have been no intense researches on the role of chloride during the synthesis of gold seeds using the citrate reduction method prior to this work. The results presented in the following have also been found by another group and have been published recently.[79]

To synthesize the particles 2.5 ml of a 5 mM H[$AuCl_4$] solution was mixed with 46.5 ml of water and heated until boiling. To the boiling solution 1 ml of a 1 % (w/v) sodium citrate solution was injected very quickly under vigorous stirring. The chloride concentration was changed by adding a certain amount of a 1 M sodium chloride solution before the injection of the sodium citrate.

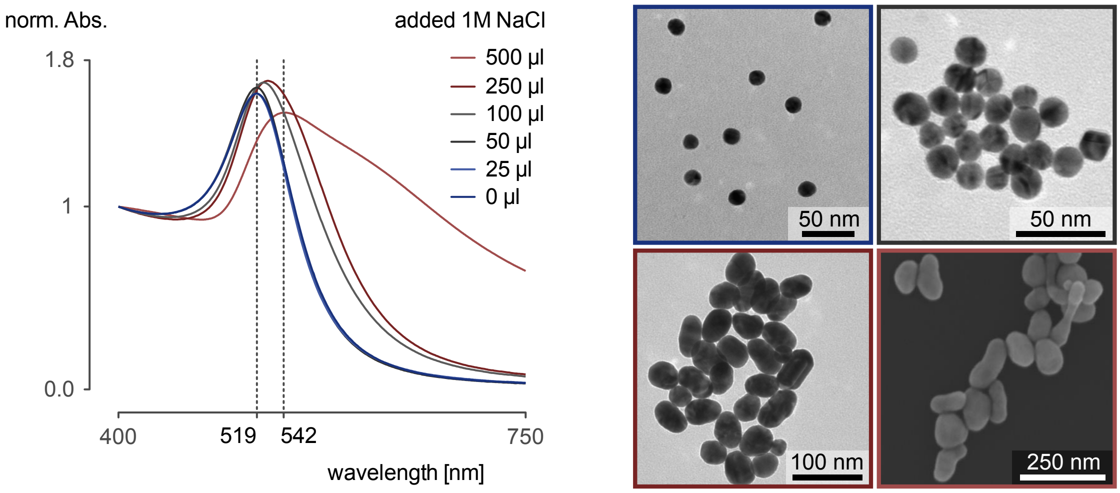

Figure 2.2.2.. An increase of the chloride concentration in the standard citrate reduction method leads to the formation of larger particles with an increased aspect ratio. The corresponding UV/Vis spectra show a red shift of the plasmon resonance position accompanied by a broadening of the band.

The particle size changed from 15 nm for the standard procedure without additional chloride ions to about 85 nm for the highest chloride concentration. Simultaneously the aspect ratio of the obtained particles increased and the size distribution broadened considerably. From the UV/Vis spectra the increase in particle size can be seen by the increase and red-shift of the plasmon resonance band. For the sample with the largest particles, that show aspect ratios varying from 1:1 up to 1:3, a broad shoulder in the low energy regime of the spectrum is present. This can be attributed to the longitudinal plasmon mode of the elongated particles.

At the moment there is still controversy of how exactly the particles are formed during the citrate reduction process. The most widespread concept is that, after the reduction of Au^{3+} species to Au^0, small gold seeds are formed that very quickly arrange into large networks of nanowires with a diameter of about 5 nm. Finally after a growth and a segmentation of the wires larger spherical nanoparticles are formed.[80] A different work claims that there is no formation of any network but rather a multi-step mechanism of different nucleation and coalescence events.[81] However, these results were, unlike stated in the work, not obtained under classical Turkevich conditions but at lower temperatures and also with a different procedure of mixing the gold precursor and the sodium citrate solutions.

Following the first theory and keeping in mind that chloride ions were found to drastically influence the mobility of gold surface atoms the results found in the experiments can be explained satisfactorily. If the intraparticle ripening rate is increased then already larger fragments of the intermediate network will arrange into single particles. This explains both the larger sizes and the elongation of the particles obtained for higher chloride ion concentrations present.

2.2.2. Less chloride than usual

For the syntheses presented in this section the chloride ions have been removed completely by changing the gold precursor from hydrogen tetrachloroaurate to gold hydroxide. It was found that many different particle shapes are accessible by just changing the concentrations of the gold precursor, the reducing agents and the temperature.

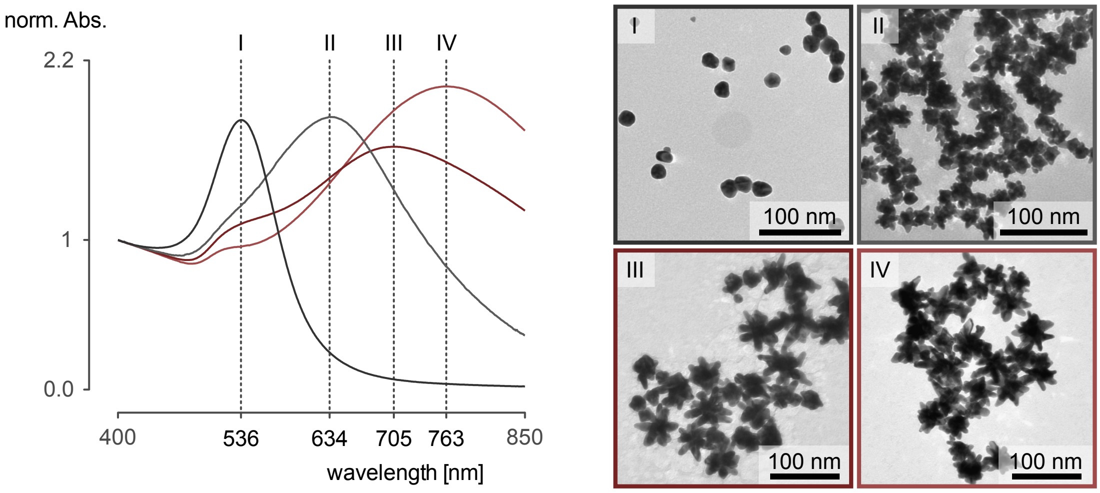

Figure 2.2.3.. Changing the concentrations and ratios of gold hydroxide and ascorbic acid the arm length of the star-shaped gold nanoparticles can be tuned. This variation of the morphology causes a significant shift of the plasmon resonance position.

The new precursor gold hydroxide is not directly soluble in water. Therefore 20 mg of the hydroxide have been dissolved in 20 ml of a 0.1 M sodium hydroxide solution at 80 °C over a time of 2 h. The increase in solubility is due to the formation of sodium tetrahdroxoaurate. Afterwards the pH was lowered to the desired value by adding a cation exchange resin. Finally the solutions were centrifuged to remove any solid residues. The obtained gold hydroxide solution was stable for several days and stored in the dark. In a typical experiment a certain amount of the gold hydroxide solution was diluted with water to give a total volume of 2 ml. Afterwards a desired volume of a reducing solution, which was either a 1 % (w/v) ascorbic acid solution or a mixture of a 1 % (w/v) ascorbic acid and a 1 % (w/v) citric acid solution, was injected quickly under vigorous stirring.

The particle morphology that was accessible most reproducibly was star-shaped or flower-like. These particles could be synthesized at room temperature using a gold hydroxide solution with a pH of 8 and the addition of an ascorbic acid solution. In general the arms of the stars become longer for an increased amount of ascorbic acid added to a fixed gold concentration. However it was found that the concentration of the gold hydroxide is also crucial.

It is believed that the formation of the shapes found is due to a diffusion controlled mechanism. High gold concentrations and low ascorbic acid concentrations led to the formation of almost spherical particles. In this case the reduction will be slow and the large amount of gold precursor ensures a steady supply of material for the particles to grow uniformly. For lower gold concentrations and an increased amount of ascorbic acid the reduction will be faster and the diffusion of new material to the particles will be slower. This results in a dendritic particle shape. It should be noticed that the absence of chloride ions prevents an intraparticle ripening and therefore the shape will remain in the state as formed.

The change of the particle morphology from almost spherical in shape to star-shaped results in a shift of the plasmon resonance position of more than 200 nm (see figure 2.2.3). To prove the dependence of the plasmon resonance shift on the particle shape DDA simulations have been performed. Therefore a core of 30 nm in diameter with ten equally distributed arms with a diameter of 20 nm each and a length ranging from 5-30 nm has been used as a model particle. The dipole separation for the simulations was 1 nm. For the particle the dielectric function from Johnson and Christy[9] has been used and the embedding medium was characterized by a refractive index of 1.33.

Changing the particle morphology from almost spherical to star-shaped causes an increase in the extinction efficiency and a shift of the plasmon resonance position towards lower energies (see figure 2.2.3). The results of the DDA simulations are in

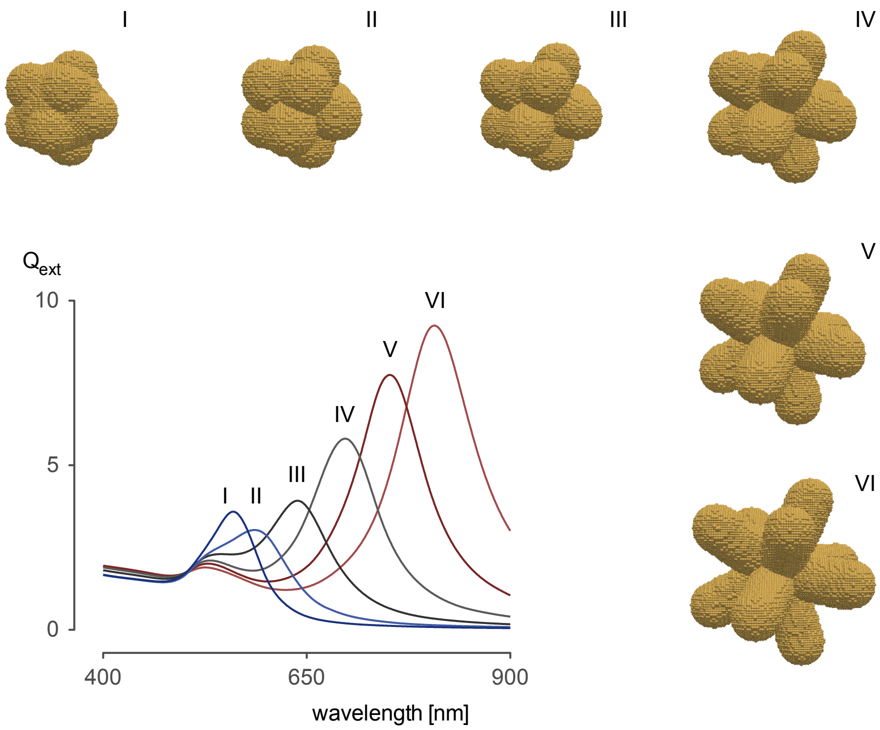

Figure 2.2.4.. From DDA simulations it can be seen that by extending the arms of the star-shaped particles the plasmon resonance position can be shifted to lower energies.

good agreement with the experimental findings. Deviations between theoretical and experimental spectra, like the different widths of the bands, can be attributed to the size distribution of the particles and the distribution of the number and size of the arms per particle.

Besides the star-shaped structures it was also possible to obtain decahedral and “desert-rose-shaped” particles. The latter have been synthesized as follows. The pH of the alkaline sodium tetrahydroxoaurate solution has been lowered to value of 6. Afterwards 1 ml of this solution was diluted with water to give a final volume of 2 ml. Then 25 µl of the ascorbic acid solution was injected quickly at room temperature. For the synthesis of the decahedral gold nanoparticles 0.5 ml of a gold precursor solution with a pH of 8 has been diluted to again a total volume of 2 ml. This solution was heated to boiling and 50 µl of a solution containing a 1:1 mixture of ascorbic acid and sodium citrate was injected.

TEM investigations reveal that the pentagonal gold nanoparticles obtained from the above synthesis have an edge length of about 20 nm. Besides larger bulky and some

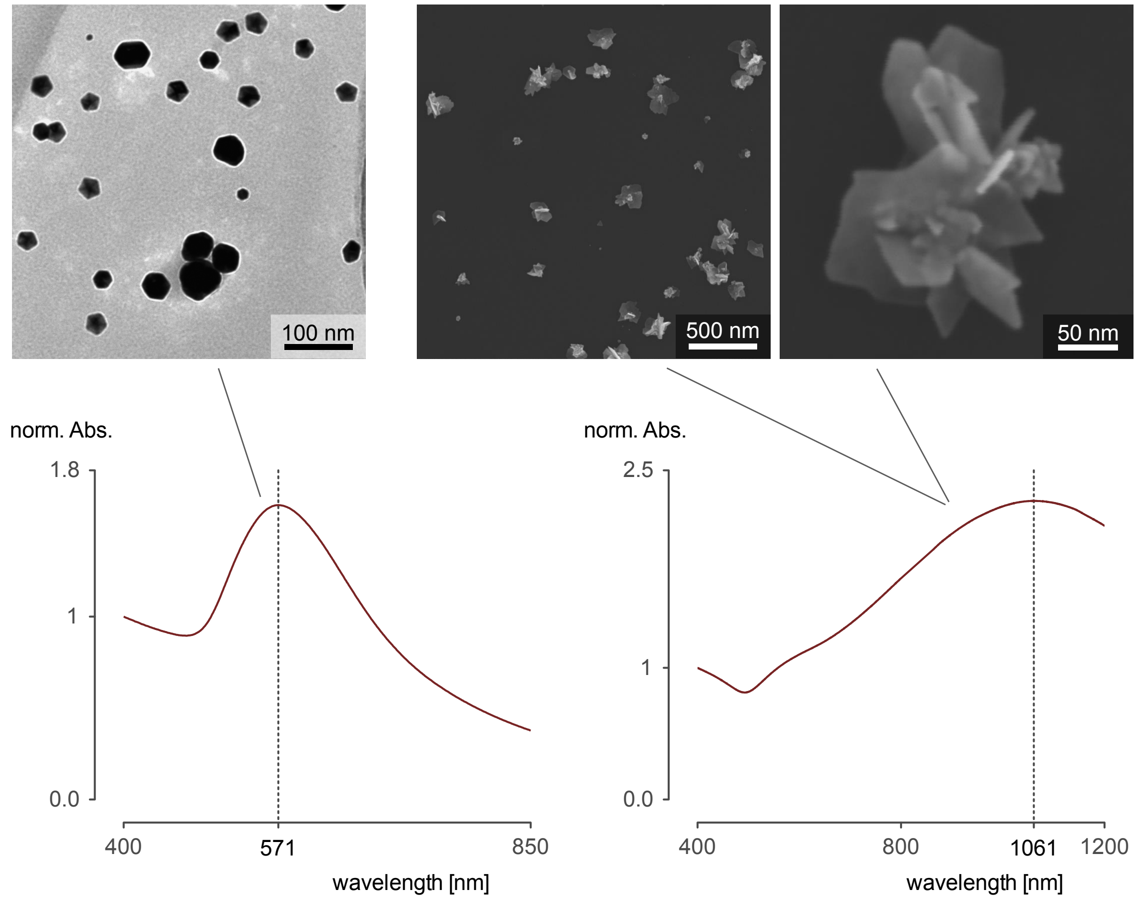

Figure 2.2.5.. TEM and SEM micrographs and UV/Vis spectra of decahedral and “desert-rose-shaped” gold nanoparticles.

hexagonal shaped particles the overall content of nanodecahedra formed is about 75 %. From the UV/Vis spectra of the decahedral gold nanoparticle solutions it can be seen that the plasmon resonance is shifted to lower energies like compared to spherical particles of the same size. This is in agreement with previously found results.[82]

The “desert-rose-shaped” particles consist of nanoplates that are about 10 nm thin and up to several hundreds of nanometers in lateral expansion. They show a very broad plasmon resonance in the near-IR region. The broadening can be attributed to the rather poor size distribution.

A pentagonal symmetry like found in decahedra is just possible if the particles show a five-fold twinning. This becomes favorable if the energy saving due to the exposure of just [111]-type faces is larger than the expense in energy for the twinning. Neglecting all surface interactions the [111]-type faces in gold crystals show a lower surface energy than the [100]- and [110]-type faces, respectively.[83] Surface effects are more significant for small particles because of the higher surface to volume ratio. So far just very small metal nanoparticle seeds that show a pentagonal symmetry have been synthesized in aqueous media.[84] It is believed that the savings in energy become less if there is an interaction between the gold surface atoms and some strongly complexing agents like chloride ions. This could at least be true for aqueous systems. Even larger decahedral gold nanoparticles than those presented here could be synthesized in organic solvents by the group of Liz-Marzán.[85] They showed that for the formation of the pentagonal particles the initial seeds have to have also a five-fold symmetry. Although this method is quite different from the present one, it is most probable that an initial formation of pentagonal seeds takes place which successively grow into larger particles likewise.

The growth of plate like structures is commonly believed to be because of a formation of twin planes on [111]-type faces.[86] This is very likely for gold since the stacking fault energy is lower than in most metals. A further growth into larger plates is preferred because an ad-atom has only limited stability on a [111]-type face due to the presence of only three nearest atomic neighbors. A formation of "desert-rose-like" shapes would be possible via the suggested mechanism if the initial seed consists of multiply twinned crystals.

In conclusion, it can be said that most probably the type and form of the initial nuclei is crucial for the formation of the particles with decahedral and "desert-rose-like" shape. More work has to be done to fully understand the origin of the different structures and to increase the reproducibility of the syntheses.

2.3. Résumé

In this chapter a simple method via a seeded growth approach to synthesize gold nanoparticles covering a large size range is presented. The particles show good shape and size uniformity as well as good long term stability. The two key features that lead to the low polydispersity and the formation of only spherical particles were the applied mixture of ascorbic acid and sodium citrate as reducing and stabilizing agents as well as the whole process of the separated and slow addition of reducing and precursor solutions followed by a heating step. The UV/Vis spectra are compared to those predicted by simple Mie theory calculations and the deviations observed are

explained by taking into consideration the size distributions of the particle sols and the corrections to the dielectric function. Furthermore the growth mechanism was clarified with the help of TEM investigations.
In the second part of this chapter the influence of chloride ions on the formation and the ripening of gold nanostructures is shown. It was found that an increase in the chloride concentration both promotes the intraparticle ripening process in the seeded growth method and influences the particle size and form in the standard citrate reduction method. Furthermore it was possible to obtain star-shaped, decahedral and “desert-rose-shaped” gold nanostructures by completely removing the chloride ions from the solution.

3. Non-ordered assemblies of gold nanoparticles

During the last decades various methods to synthesize nanoparticles of different materials and a rich diversity of particle shapes have been developed. Many of them show extraordinary properties deviating from the bulk properties. Probably the best examples will of cause be the quantum size effect in semiconductor nanoparticles as well as the plasmonic effects that could be observed in differently shaped noble metal nanoparticles. However, in order to practically use these great properties for certain applications like sensing, light harvesting, waveguiding or catalysis, a specific assembly of the nanoparticles into larger or macroscopic structures may be necessary. In this chapter two different assembly strategies for gold nanoparticles will be presented. The first one is an immobilization of differently sized gold nanoparticles into non-ordered films, aiming for structures with high near field enhancement. Furthermore a procedure to form freestanding, quasi two-dimensional porous nanosheets will be depicted.

3.1. Hierarchical assembly of gold nanospheres

In 2003 Stockman and colleagues proposed an assembly of self-similar silver nanoparticles to be a very efficient structure to drastically enhance the electric near-field of an incident electromagnetic wave.[87] They could show theoretically that certain types of the so called “nanolenses” exhibit field enhancement factors of more than 2000. Since the SERS enhancement factor scales with the fourth power of the electric field, the electromagnetic part of the overall enhancement will already be in the order of 10^{13}. The additional chemical enhancement, which is usually in the range of 10-1000, will lead to a total enhancement factor of up to 10^{16}. This is even one order of magnitude higher than what was reported for single molecule detection.[88]

During studies of the immobilization of citrate stabilized gold nanoparticles on func-

tionalized glass substrates, it was found that the saturated surface coverage is always about 30 %, regardless of the particle diameter. Therefore the mean interparticle distance becomes larger for bigger particles. Now the idea arose to fill the free space between the large particles immobilized on the glass substrate with smaller particles. After filling the remaining free space with a third size of particles, a large number of sites on the substrate should have the geometry of the proposed "nanolenses".
The formation of "nanolens" arrays on other substrates than glass slides will offer a large number of potential applications. The particles could for example be attached to silica spheres together with a Raman reporter molecule. These structures can be used for example as biomarkers.[89] By the integration of the "nanolens" structures in capillaries or porous oxides it should be possible to built highly sensitive SERS sensors.[90]

3.1.1. Preparation of the nanoparticle films

For the fabrication of the non-ordered nanolens arrays citrate stabilized gold nanoparticles of different sizes have been used. The particles were prepared according to the method described in chapter 2. In order to immobilize the particles, the layer-by-layer (LbL) technique has been utilized.
At first microscope glass slides were cut into pieces with a size of 1 × 2 cm. The glass substrates were cleaned by sonicating them first in isopropanol for 15 min and then in water for 15 min. Afterwards they were rinsed with water extensively and immersed into a warm fresh prepared piranha solution (a mixture of concentrated sulfuric acid and 30 % hydrogen peroxide with a ratio of 1:2) for another 30 min. Despite an additional cleaning effect the last step was needed to make the surface of the substrates highly hydrophilic.
Now the hydrophilic surface carried an excess of negative charges, that can be used to functionalize it with a cationic polymer. Two different polymers, polydiallyldimethylammonium chloride (PDDA) and polyallylamine hydrochloride (PAH), that are well known for LbL applications have been used. However, for the substrates functionalized with PDDA an increased destabilization of the gold colloids during the immobilization process of the nanoparticles was observed. Therefore just PAH was used in the further experiments.
The hydrophilic substrates were rinsed with water excessively and then placed into an aqueous solution containing 0.1 % w/v of PAH and 0.5 M NaCl. The sodium chloride concentration controls the roughness of polyelectrolyte layers.[91;92] After 30 min the

substrates were removed from the polyelectrolyte solution and excessively rinsed with water again.

Without letting the water evaporate, the substrates were placed into a solution of citrate stabilized gold nanoparticles with desired size. The beakers with the glass substrates and the gold colloid were sealed and shaken gently over a time of at least 24 h to ensure a saturated coverage. Afterwards the substrates were rinsed with water again and placed into a solution of particles with a smaller size. This procedure was repeated to immobilize particles of the smallest size desired. Finally the substrates were rinsed with water again and let dry under air.

For the UV/Vis spectroscopic characterization the substrates were carefully aligned perpendicular to the incident beam, since the extinction of the layers was found to be strongly angle dependent. Because both sides of the substrates are functionalized with particles, the particles on one side have been wiped down with a moist tissue prior to the measurements. The spectra obtained were corrected by the absorbance of the blank glass substrates. To probe the SERS efficiency of the substrates they were immersed into a 0.1 % (*v*/*v*) ethanolic solution of *p*-aminothiophenol (*p*-ATP) for 2 h to insure the formation of a monolayer of the test molecules on the surface of the gold nanoparticles. After the removal of the excess *p*-ATP, by intense rinsing with ethanol, the substrates were allowed to dry in air. The Raman spectra were obtained on a Renishaw RM-2000 Raman microscope using a 633 nm laser with a power of 17 μm/cm^2 at the sample. The beam was focused through a 50× objective with a numerical aperture of 0.75. The coverage of the films has been determined by evaluating SEM micrographs with the help of the program IMAGEJ.[93]

3.1.2. Higher coverage for large SERS signals

For the evaluation of the SERS activity different films have been investigated. The results, containing the kind of the particle film and the corresponding coverage and SERS intensity, are summarized in table 3.1.1. It can be seen that the SERS intensity increases for films made of larger particles and also for films with differently sized particles leading to a higher surface coverage. However, a drastic increase in the SERS intensity for the films made of three differently sized particles could not be observed.

Optical properties of films made of a single particle size

As already stated above, the coverage in saturated films of gold nanoparticles of a single size is always about 30 % (see table 3.1.1). However, the optical properties

Table 3.1.1.. Coverage and SERS intensities of different gold nanoparticle films.

diameter of particles forming the film	coverage	SERS intensity of the 1078 cm^{-1} band
78	0.304	12174
55	0.300	8174
35	0.271	5582
16	0.314	596
78 / 35	0.354	18793
78 / 35 / 16	0.389	19792
55 / 27	0.375	14212
55 / 27 / 12	0.349	16146

of the films for different particle sizes vary significantly. The overall absorbance increases for increasing particle diameters. This can be attributed to the increasing total amount of the gold. Keeping the cross sectional area constant, the total volume of the gold nanoparticles will scale with the ratio of the diameters of the differently sized nanoparticles, since the volume of a spherical particle depends on the third power of the diameter and the cross sectional area depends on the second power of the diameter.

For all films investigated a plasmon band at about 515 nm and another broader band in the red or near-infrared region of the spectrum could be observed. The second band has previously been attributed to interparticle coupling within the two-dimensional films and the resonance at 515 nm is usually assigned to the single particle response.[94;95] The origin of the plasmon bands can also be discussed in the light of the optical properties of chain-shaped aggregates, that are commonly formed during the aggregation of gold nanoparticles.[96–99] A coupling of the particles along the chain causes a longitudinal plasmon mode. Depending on the chain length the position can vary but is always at lower energies than the corresponding transverse mode which is approximately at the same position as the single particle plasmon mode.[3;100]

The blue-shift of the single particle resonance position in the films compared to the plasmon resonance of the particles in solution can be explained by the change in the refractive index of the embedding medium. Although the effect of the particle size on the resonance position is smaller for a smaller index of refraction of the surrounding medium, the position should still change for different particle sizes. This was not observed though. A possible reason for this effect could again be the coupling between

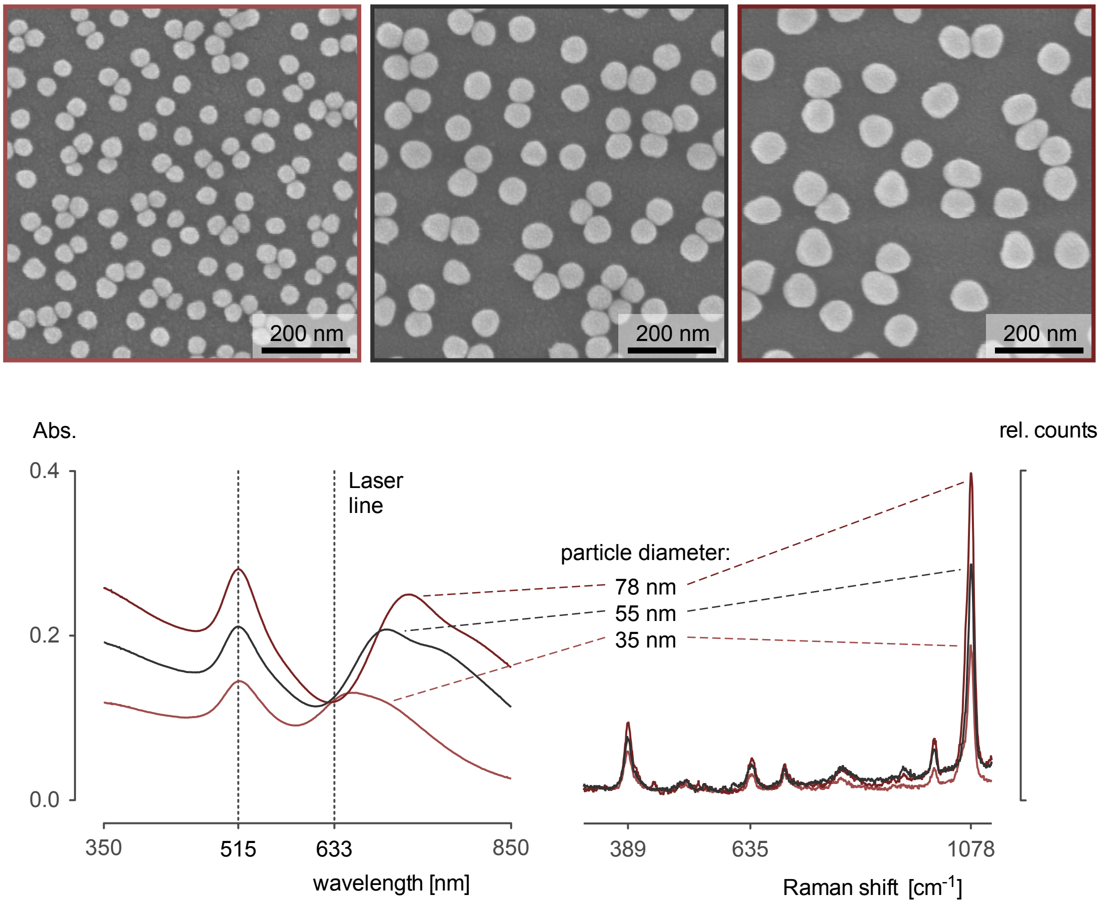

Figure 3.1.1.. The absorbance as well as the SERS intensity of the gold nanoparticle films increases for increasing particle diameters.

all the particles in the film, which will also affect the position of the dipolar mode or transverse mode of the particles like stated in plasmon hybridization theory.[101]
From the UV/Vis spectra it can be seen that all three films that are made of a single particle size have about the same absorbance at the wavelength of the laser used in the Raman experiments. Nevertheless the intensity of the SERS spectra are increasing for increasing particle diameters (see figure 3.1.1). One reason is the stronger SERS enhancement for larger single gold nanoparticles.[102] A useful measure will be the averaged enhancement factor that incorporates the mean electromagnetic field enhancement on the overall particle surface rather than just the highest field enhancement. For the particle diameters discussed here an increase in the average enhancement factor at the wavelength of 633 nm can be found for increasing particle diameters.[4;103] Another, possibly even more significant reason for the increase in

the scattering intensity will be the coupling of the particles. During the deposition process the films of larger particles show more agglomerates resulting in higher electric field enhancements and hence higher SERS intensities.

Optical properties of films made of different particle sizes

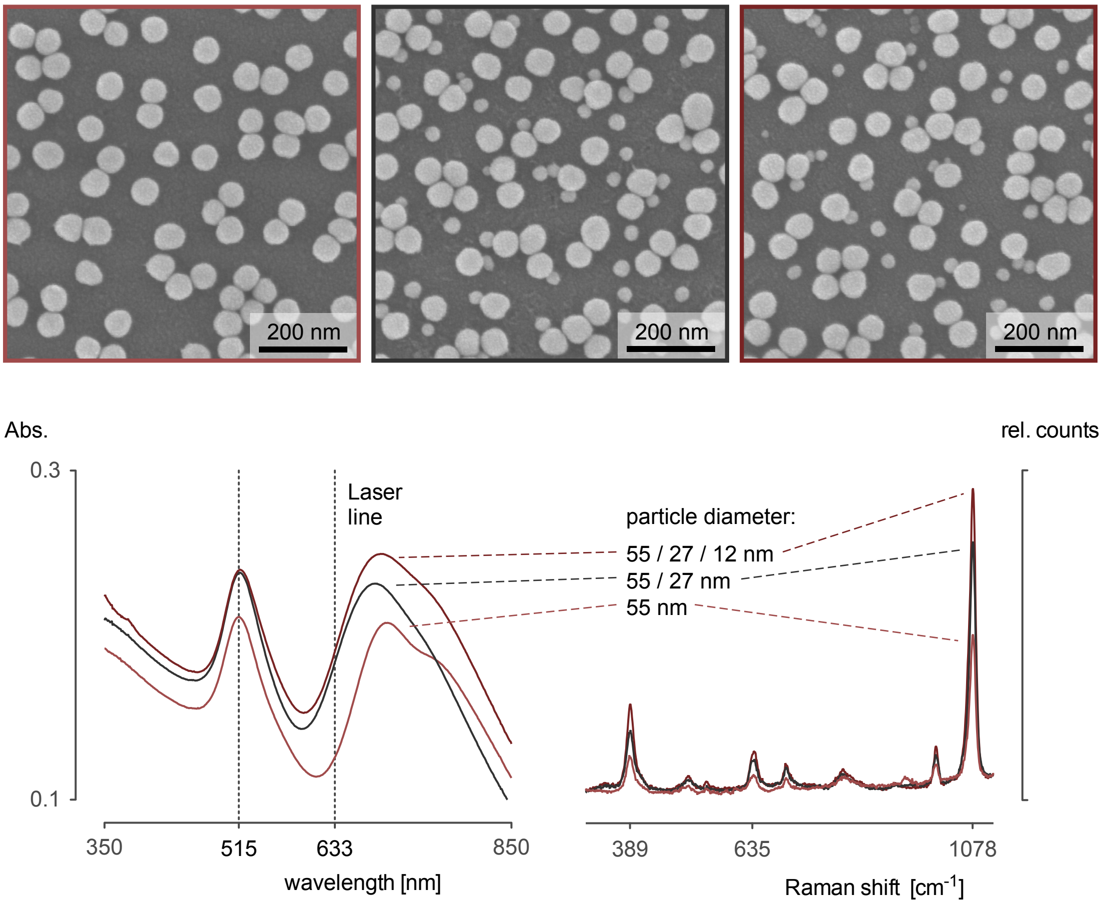

Figure 3.1.2.. It can be seen from the SEM micrographs that the desired structures could not be achieved. However, the overall absorbance and the SERS intensity increase for an increasing particle coverage.

To achieve the desired assemblies of self similar spheres a multistep deposition has been performed. Within a single film the particle size was therefore decreased by a factor of approximately two in each step. The diameters of the particles for the films presented were 78, 35 and 16 nm for the first film and 55, 27 and 12 nm for the second film. For both films the SERS intensity of the 1078 cm^{-1} band increased for each step, although the coverage of the complete second film decreased slightly compared to the second step of deposition (see figure 3.1.2 and table 3.1.1). This is very likely to be due to an error in the evaluation of the SEM pictures since just a small region of the film can be observed. The overall absorbance increases and thus also the amount of gold in the film has to be larger.

It can be seen from the SEM micrographs that the desired structure could not be produced. Therefore it was also not possible to achieve a significant increase in the SERS intensity for the films made of different particle sizes. The increase found could be explained by a higher surface coverage and a slightly higher degree of agglomeration. The UV/Vis spectra show that the plasmonic response of the films made of different particle sizes is comparable to these made of a single particle size.

Calculation of the SERS enhancement factors

The near-field around the particles in the films can be characterized by the SERS enhancement factor. Since the measurements are always on ensembles of particles just an ensemble averaged enhancement factor (EF) can be obtained. Therefore the intensity of the Raman band at 1078 cm^{-1} of the test molecule *p*-ATP has been used. The band can be assigned to the C−S stretching vibration.[104] The enhancement factor is the ratio of the intensities of the Raman band in the enhanced and the not enhanced case, normalized by the respective number of scattering molecules measured.

$$\mathrm{EF} = \frac{I_{\mathrm{SERS}}/N_{\mathrm{ads}}}{I_{\mathrm{bulk}}/N_{\mathrm{bulk}}} \tag{3.1.1}$$

The number of molecules that contribute to the intensity of the enhanced case can be calculated from the surface of the gold nanoparticles in the area of the laser beam (diameter of the focus is approximately 2 μm) and the area that is occupied by a single *p*-ATP molecule (0.2 nm^2).[105] For the non-enhanced case the number of molecules that contribute to the scattering intensity can be calculated from the sampling volume and the molecule density in the bulk, whereas the molecule density can be determined from the density (approximately 1 $\mathrm{g/cm}^3$) and the molar mass ($\mathrm{M}_{p-\mathrm{ATP}}$ = 125.2 g/mol). The sampling volume is strongly system dependent and is therefore more difficult to obtain. For its calculation a method proposed in the literature has been used.[106]

The Raman microscope that has been used for the measurements has a confocal setup. Hence the sampling volume is strongly dependent on the thickness of the focal plane. This thickness depends on the numerical aperture of the objective, the size of the used pinhole and the wavelength. Light from the center of the focal plane travels to the detector with a minimum of attenuation and therefore molecules located in this region give a maximum contribution to the Raman signal. However, also molecules located slightly below or above the center of the focal plane will contribute to the overall Raman scattering intensity. Of course the scattering part of a layer of molecules that is further away from the center of the focal plane will be weaker.

In order to determine the contribution of the molecules in a certain distance from the focus, Raman spectra of a silicon wafer have been recorded with different degrees of defocussing. Assuming that the penetration depth of the laser beam is very small for silicon, the Raman intensity arises just from a very thin layer of the top silicon atoms. Now the intensity of the transverse optical phonon mode of silicon at 520 nm was measured for different separation distances. Therefore the microscope stage was moved in micron steps away from the focus. It could be found that the dependence of the intensity from the distance can be very well approximated with one side of a Lorentzian curve.

For a transparent sample this would be the dependence of the contribution of a thin layer of molecules at a certain distance to the center of the focal plane to the overall Raman intensity. Hence, the integral over this curve will give the whole Raman scattering intensity of a transparent bulk sample with the laser beam being focused on the surface. By introducing an effective penetration depth it is possible to calculate the number of molecules contributing to the Raman intensity. The effective penetration depth will be the hight of a cylinder with diameter of the focal spot. The molecules in the volume of this cylinder are assumed to all contribute to the overall intensity equally and with the maximum intensity found for the molecules in the focus. This means that the effective penetrations depth can be defined as the length that multiplied by the maximum intensity is equal to the area under the Lorentzian curve. For the spectrometer used this effective penetration depth could be determined to 6.6 µm. Hence the number of molecules N_{bulk} in equation 3.1.1 is approximately 10^{11}.

From the Raman intensity found for the bulk measurements (187 counts) and the SERS intensities given in table 3.1.1 the averaged SERS enhancement factors can be calculated. For the films made of a single particle size these are $1.7 \cdot 10^4$, $1.6 \cdot 10^5$, $2.3 \cdot 10^5$ and $3.4 \cdot 10^5$ for the 16, 35, 55 and 78 nm films, respectively. Taking the increased coverage into consideration the maximum SERS enhancement factor could be determined to $4.3 \cdot 10^5$ for the film made of particles with a diameter of 78, 35 and 16 nm and is just slightly higher than for the film consisting of 78 nm only. The enhancement factors found are in good agreement with previously published ones.[107]

3.1.3. Theoretical consideration of the optical properties of the gold nanoparticle films

In order to accurately describe the origin of the optical properties of plasmonic structures it is often useful to apply theoretical modeling techniques. In the present case it can be seen that the plasmonic resonance in the red and near-infrared region is not due to a long range coupling of well separated particles in a two-dimensional film, but rather due to particle agglomerates. Furthermore the experimentally found plasmon resonance at 515 nm should be at lower energies for films made of separated particles.

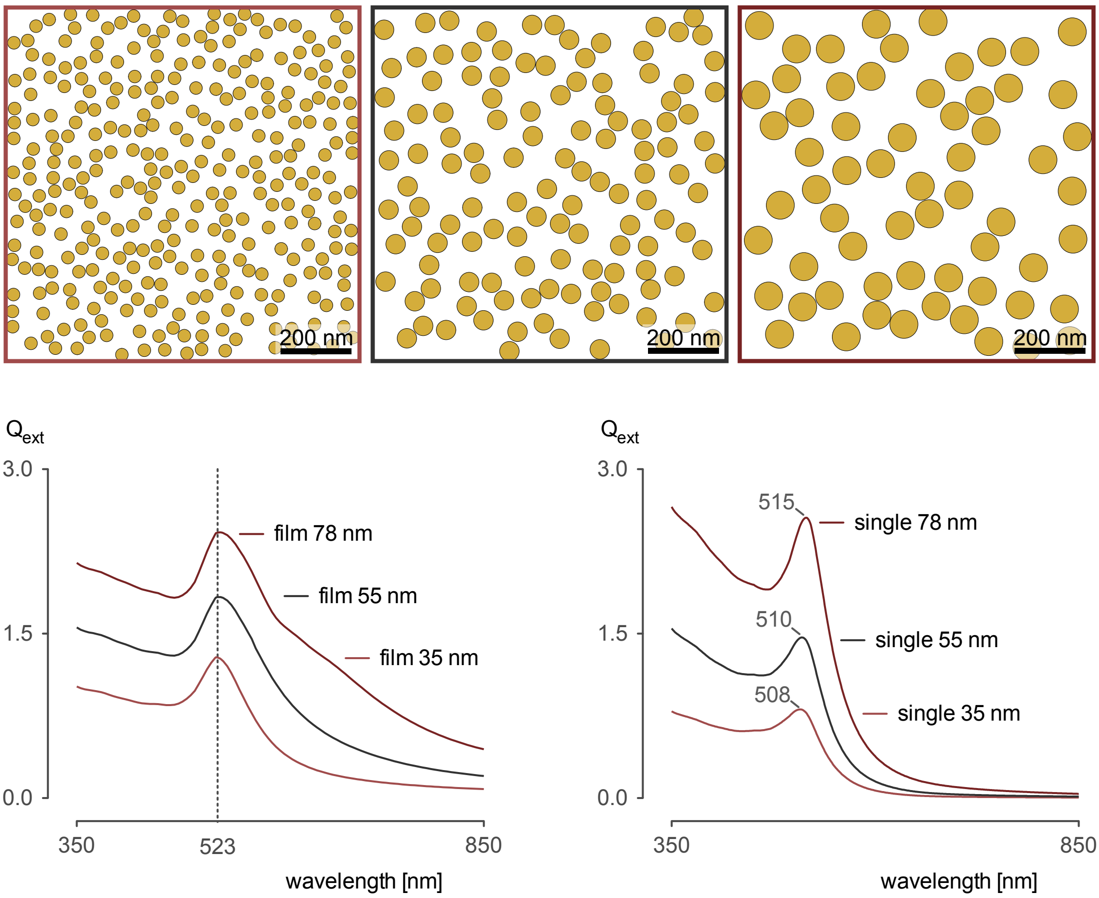

Figure 3.1.3.. For the theoretical simulations of the films a broadening of the single particle plasmon band towards lower energies can be seen. Resonances in the red and near-infrared region can not be explained.

To generate the films used for the modeling, particles with diameters of 35, 55 and 78 nm have been randomly arranged on an area of $1 \times 1\,\mu\text{m}^2$ assuming hard spheres and neglecting any particle interactions to give a total coverage of 30 % for each film. The simulations of the optical properties of the generated films were performed using the GMM software by Xu.[27]

Similar to the experimental results, all nanoparticle films show the same plasmon resonance position (see figure 3.1.3). However, the theoretical predicted resonance wavelength is at lower energies than found experimentally (515 nm in the experimental case and 523 nm for the simulations). In principle the theoretically derived resonance position should be at higher energies because the glass substrate, which would cause a red-shift, has not been included in the simulation. Most probably the blue-shift can be attributed to the coalescence of the particles aggregated in the film. A conductive connection between particles will cause a blue-shift of the transverse plasmon resonance positions.[108;109] This is a similar effect like found for gold nanorods, where the transverse plasmon mode also experiences a blue-shift for an increasing aspect ratio.[110]

Furthermore an asymmetric broadening on the low energy side of the plasmon resonance position can be seen. Nevertheless, the resonances in the red and near-infrared region of the spectrum can not be explained by the model. Calculating the mean nearest neighbor distances for the films, used for modeling, one obtains 8, 12 and 17 nm for the 35, 55 and 78 nm films, respectively. Like already seen for the calculations of the coupling in gold nanoparticle dimers, these distances will not cause a coupling strong enough to give plasmon resonances in the red and near-infrared region (see chapter 1).

Therefore some chainlike random aggregates of 78 nm gold nanospheres with interparticle separation distances of 1 nm have been modeled (see figure 3.1.4). It can be seen that again the transverse plasmon resonance position remains the same for all agglomerates. But now many resonances appear in the low energy regime of the spectrum. It is easy to imagine that the multitude of different sizes and geometries of agglomerates that contribute to the experimentally measured spectrum will yield a broad resonance in the red and near-infrared region of the spectrum.

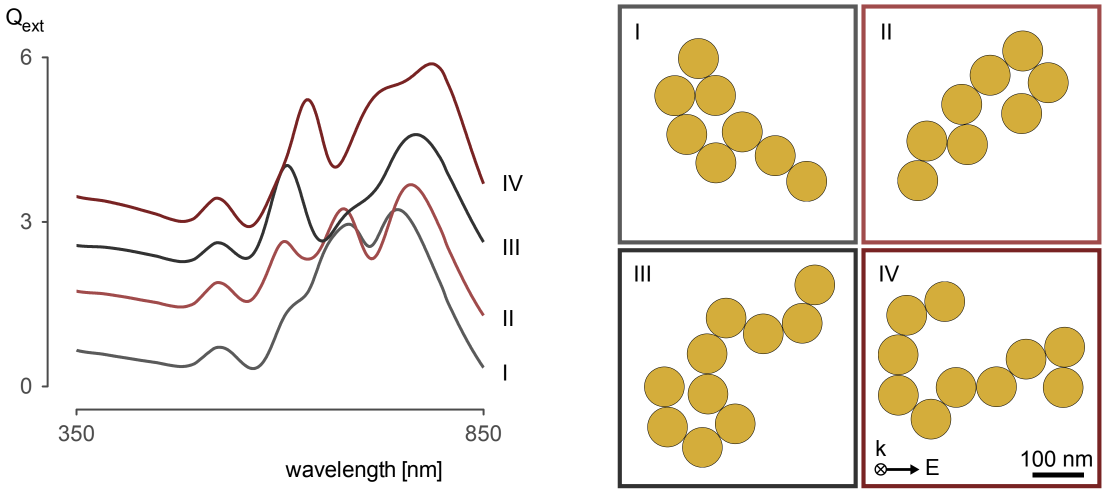

Figure 3.1.4.. The simulated spectra of agglomerates formed by 78 nm gold nanospheres show several resonances in the red and near-infrared region.

3.2. Assembly of gold nanoparticles into porous nanosheets

Porous structures are particularly suitable for sensing and catalysis applications due to their high surface to volume ratio. Especially recent developments in the formation of porous aerogel structures formed by the controlled destabilization of nanoparticle solutions have attracted attention. The formation of three dimensional aerogel structures made of semiconductor nanocrystals, metal nanoparticles or mixtures of both has been reported.[111–114]

Two-dimensional assemblies of nanoparticles are usually realized via trapping the particles on a liquid-air or liquid-liquid interface.[115–117] An assembly of nanoparticles into free floating two-dimensional sheets has also been reported.[118] For citrate stabilized gold nanoparticles it has been found that it is possible to introduce a latent destabilization of the particles by adding ethanol to the colloids. The nanoparticle solutions are still stable but upon the overlay of the solutions with an non-polar solvent the particles spontaneously self-assemble at the liquid-liquid interface.[115] This method produces a monolayer of particles at the interface that even extends up the non-polar solvent/glass interface. Within the layer the particles are still separated.

To form porous gold nanosheets, this destabilization procedure has been modified. The gold nanoparticle solutions used, have been prepared by either a citrate reduction or borohydride reduction method.[17;53] For the formation of the two-dimensional assembly, the gold colloids have been overlaid carefully with n-butanol and were then kept at 60 °C for 1 week. Afterwards most of the n-butanol was removed carefully with a syringe. Then the solution was washed several times with water, to remove the remaining gold particles, salts and the rest of the butanol which successively dissolved in the aqueous phase. Finally the samples were freeze dried to obtain quasi two-dimensional, self supporting and porous gold nano sheets.

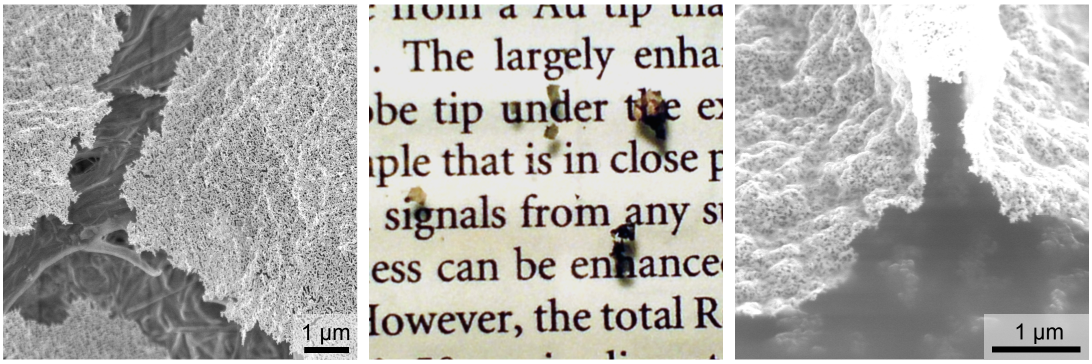

Figure 3.2.1.. SEM micrographs show that the several millimeter large self-supporting films are porous and have a thickness of below 20 nm. From the photograph the transparency of the films can be seen.

During the freeze drying process the sheets were split which led to a final size of several square millimeters. The material is semi transparent and has a brownish black color (see figure 3.2.1). Under a certain viewing angle a copper like shiny reflection can be seen. The SEM micrographs reveal that the layers are porous and very thin. A thickness could not be determined exactly but was estimated to be smaller than 20 nm.

Since butanol is sparsely soluble in water it serves as destabilizing agent and simultaneously forms a second phase above the water phase. The concentration gradient of the butanol in water makes sure that the gold particles are first destabilized at the interface. The destabilization itself is due to a decrease of the surface charge density of the gold nanoparticles. If the particles with a lowered surface charge density move to the interface, the remaining surface charges will arrange on the water side and the blank gold surface will be covered by the organic phase.[115] The elevated temperature promotes the formation of an interparticle connection as well as the overall destabilization rate.

Interestingly, attempts to apply the controlled destabilization procedure to citrate stabilized silver colloids were not successful. The silver nanoparticle solutions could not be destabilized and remained unchanged for several days. After two to three weeks the color of the colloids changed from clear yellow to bluish green. TEM investigations revealed that this was due to a change of the particle morphology from spherical to triangular prismatic. A similar transformation has already been reported before and was attributed to a photo induced conversion.[119] The influence of the added alcohol on the surface charge density of the silver nanoparticles is probably much smaller because of an silver oxide layer that can form around the particles under ambient conditions.

First experiments to overcome this limitation could produce small areas of silver films on the interface. Therefore the surface of the silver nanoparticles was reduced to metallic silver by the addition of sodium borohydride under an argon atmosphere. Afterwards ethanol was added to the silver nanoparticle solution followed by an overlaying of the solution with n-heptane. Within several hours a formation of silver nanoparticle monolayers at the solution interface could be observed. These layers could not be freeze dried to give porous films like found for the gold case, but resulted in a black powder.

3.3. Résumé

It could be shown that, using the LbL technique, it is possible to increase the overall coverage of gold nanoparticle films by immobilizing particles with different diameters. This led to a higher absorbance of the films and a higher enhancement of the SERS signal of the Raman probe. The intended “nanolens” structures and the associated large enhancement factors could not be accomplished. This is probably due to an electrostatic shielding of the free space on the substrates. The large gold nanoparticles still cary a negative charge which makes it hardly possible for the also negatively charged smaller nanoparticles to reach the free surface regions. With the help of theoretical simulations it was possible to explain the optical response found in the UV/Vis spectra.

Besides, a new technique to assemble gold nanoparticles into self-supporting, transparent and porous nanosheets has been developed. The films are several millimeters large while having a thickness of just below 20 nm.

4. Tetrazol stabilized silver colloids[†]

Metallic nanoparticles have attracted considerable interest both by fundamental researchers as well as by industry.[61;114;121–123] Until today a huge variety of different types of compounds has been investigated for their use as capping agents for nanoparticles. However, tetrazole derivatives constitute a peculiar class of heterocyclic organic compounds that until now has not been commonly used for that purpose. They represent a promising new group of ligands in nanochemistry which unites many desired properties such as high coordination ability and a broad range of available derivatives.[124–126] Moreover, a thermally induced decomposition of tetrazoles leads to a high percentage of gaseous products. This might be an interesting feature for future applications in coatings, since the removal of capping agents provides a tremendous potential to improve charge transfer, sensing and catalytic properties of the nanoparticles and their assemblies.[127] The tetrazole unit itself is a bioisostere to the carboxylate group and thus an interesting compound for pharmaceutical research.[128]

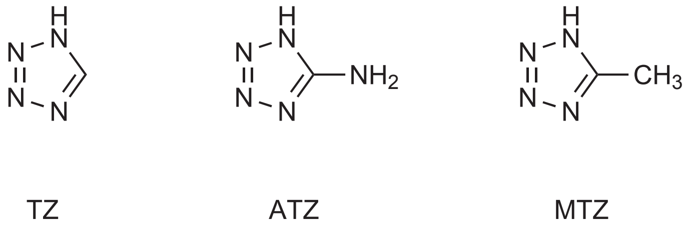

Figure 4.0.1.. Structural formulas of 1H-tetrazole, 5-amino-tetrazole and 5-methyl-tetrazole.

A synthetic procedure to fabricate silver nanoparticles stabilized by tetrazole (TZ), 5-amino-tetrazole (ATZ) and 5-methyl-tetrazole (MTZ), respectively, will be presented in the following part. The new stabilizing agents were combined with the metal precursor silver nitrate and the reductant sodium borohydride, both well established in

---

[†] Parts of this chapter have already been published.[120]

silver nanoparticle syntheses.[129] Using either ATZ or MTZ as the stabilizing agents, it was found that the synthesized particles tend to agglomerate slowly, which allows controllable in situ monitoring of the changes in the optical properties utilizing UV/Vis and Raman spectroscopy. The analysis of the data obtained was additionally supported by TEM measurements. The degree of agglomeration determines the plasmonic behavior of the nanoparticles, as well as changes in the SERS spectra of the tetrazole stabilizers. When TZ was used as a stabilizing agent no agglomeration could be observed. However, after several days the solutions became clear in color and a new substance, that could be determined as a silver tetrazole salt, precipitated as small needlelike crystals.

4.1. Aqueous synthesis of tetrazole derivative stabilized silver sols

For the synthesis of ATZ and MTZ stabilized silver colloids, a silver nitrate solution (0.2 % *w/v*), containing between 3 and 12 µmol of silver nitrate was added to a boiling solution of 0.05-1 mmol of a certain tetrazole derivative in 30 ml of water. Immediately afterwards, 2 ml of the reducing solution, containing 3 mg of sodium borohydride, were quickly injected. Depending on the desired state of aggregation, the reaction needs to be quenched, via quick cooling, directly after the injection of the borohydride or within a few minutes. Big aggregates were removed by use of 5 µm pore size PTFE syringe filters.

In the aqueous synthesis of the tetrazole stabilized particles solvent free tetrazole is needed. Pure tetrazole is a white crystalline solid, which is explosive and flammable. Therefore it is shipped as a solution in acetonitrile. The tetrazole has been obtained from the solution by carefully evaporating the solvent in a rotary evaporator. A typical procedure was as follows: In 30 ml of water 0.2 mmol of solid tetrazole were dissolved and afterwards heated to about 40 ℃. Then 0.34 ml of a 0.2 % silver nitrate solution was added under vigorous stirring, immediately followed by a quick injection of 2 ml of a freshly prepared 0.15 % sodium borohydride solution. Finally the solution was heated to its boiling point and refluxed for several minutes until the turbid solution turned into clear yellow.

4.2. Observation of different agglomeration kinetics for MTZ and ATZ stabilized silver colloids

The two ligands used show slightly different stabilizing properties. However, in general the agglomeration state of the resulting nanoparticles is mainly determined by the reaction time. Independent of the stabilizer the particle size distributions are rather poor. The range of the diameters of the silver particles is between 2 and 16 nm.

Using MTZ as stabilizer, it is possible to adjust the degree of agglomeration of the particles in the final silver sol by quenching of the reaction at different points in time after injection of the sodium borohydride solution. Direct quenching (only several seconds after the injection) results in a yellow solution with single silver particles, which is stable for weeks. Whereas longer intervals between the injection and the cooling give successively orange, red and purple solutions, containing dimers, trimeres and larger agglomerates, respectively (see figure 4.2.1). The resulting solutions are stable for days.

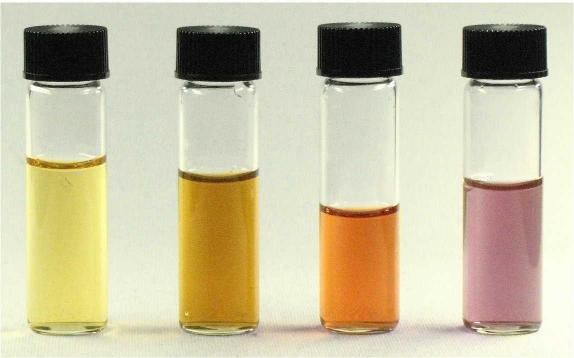

Figure 4.2.1.. The different agglomeration states of the MTZ stabilized silver colloids can easily be distinguished by eye.

For the silver sols stabilized with ATZ a slightly different process needs to be applied. The reaction has to be quenched directly after the injection of the sodium borohydride solution. Otherwise the agglomeration process will proceed until the complete destabilization of the colloid. The directly quenched colloid is stable for approximately one week. In order to start the agglomeration process slowly, the quenched solution was concentrated by vacuum evaporation at 30 mbar and 50 °C until a slight darkening of the yellow color of the solution appeared. From that point the aggregation started and proceeded over a time of one to two days.

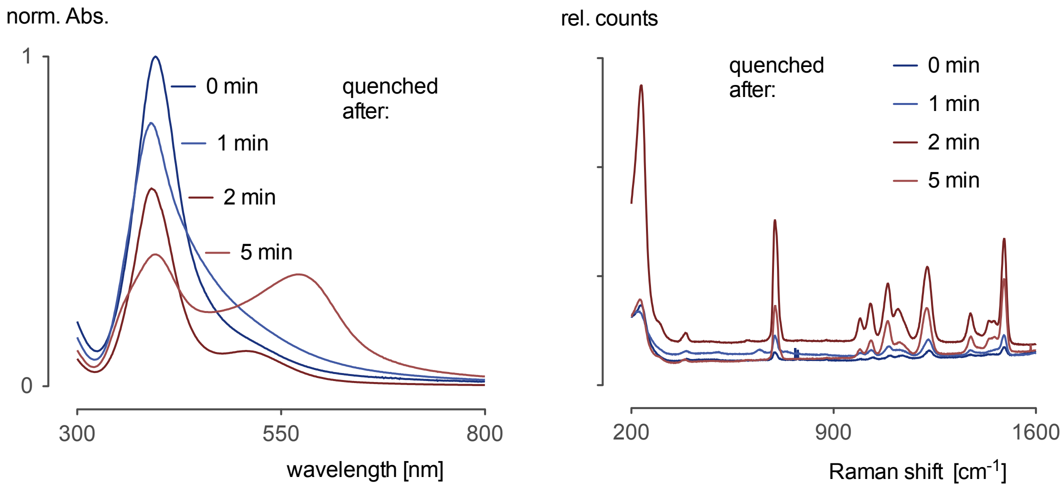

Figure 4.2.2.. With an increasing degree of agglomeration the intensity of the SERS spectrum of the stabilizer MTZ increases considerably. Finally the silver nanoparticles precipitate, which leads to a decrease of the signal. A higher state of agglomeration can also be identified by the developing second peak in the UV/Vis spectra.

The different agglomeration stages of both ligands have been investigated using UV/Vis and Raman spectroscopy. On the basis of the corresponding UV/Vis-spectra (see figure 4.2.2) of the MTZ-stabilized silver colloids shown in figure 4.2.1, the different agglomeration states are clearly comprehensible. For the yellow solution a single peak at about 395 nm originating in the surface plasmon resonance of single silver particles could be observed. With increasing agglomeration state this peak is first shifted to the higher energy region which leads to the assumption that the agglomeration starts with the bigger particles. Additionally there is a broadening of that peak and for the red and violet solutions another peak at lower energies, which is due to interparticle coupling, has been observed.

For the silver sol, stabilized with ATZ, the contour plot in figure 4.2.3 shows the changes in the UV/Vis-spectra over time due to the agglomeration process. The dominating plasmon band at 390 nm in the absorption spectrum as well as the TEM-investigations revealed that at this stage mainly single silver nanoparticles are present. Thereupon more and more dimers and trimers are formed which are responsible for the increasing and red-shifting peak between 450 nm and 550 nm. Finally both peaks decrease and bigger network-like structures are formed. The slight blue shift of the plasmon band at 390 nm in the final solution leads to the assumption that the networks are mainly formed by the bigger particles and the slight yellowish color

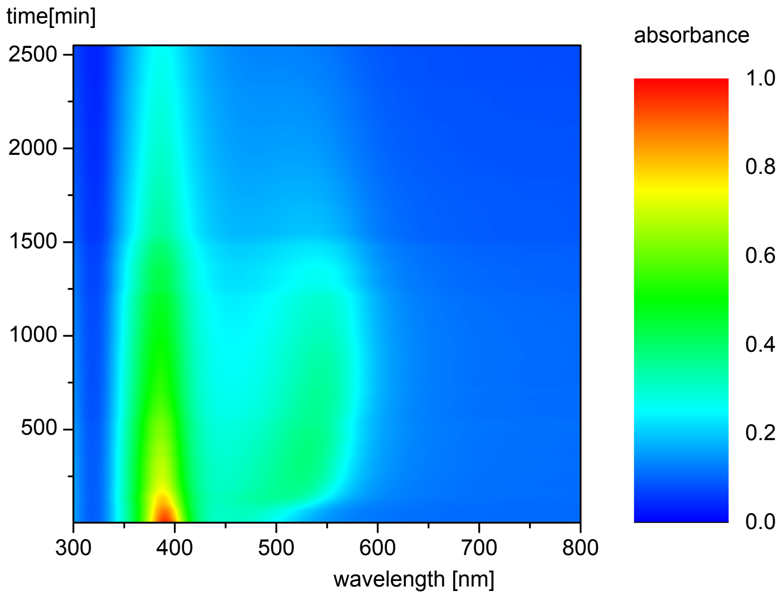

Figure 4.2.3.. The contour plot of the UV/Vis spectra recorded over a period of 42 h clearly shows an appearing second peak which is due to the plasmon coupling of the agglomerating ATZ stabilized silver nanoparticles. The final decrease of the absorbance over the whole spectral range is because of the precipitation of the big agglomerates.

of the final colloid is due to small silver nanoparticles. UV/Vis-spectra and related TEM-images of different stages during the agglomeration are shown in figure 4.2.4.
In order to investigate the agglomeration process with the aid of Raman spectroscopy the special features of surface-enhanced Raman scattering (SERS) were used.[34;35] It is well known that the Raman scattering intensity of an observed molecule in close vicinity to a nano scaled rough metal surface can be enhanced by several orders of magnitude. The enhancement will be extraordinarily high if the analyte is located inside of a small gap between two metal nanostructures. This is due to an extreme amplification of the electromagnetic field inside these geometries, which are therefore also called “hot-spots” (see section 1.3.6).[130;131]

During the agglomeration process, single particles first loosely bind together, which gives the geometry needed for strong Raman enhancements.[131] Later the particles start to coalesce and the gaps between adjacent nanoparticles are vanishing again. These aggregates increase further in size and finally will precipitate so they will not contribute to the measurement anymore. Hence, by in situ measurements one should see an increasing Raman scattering intensity, which is passing a maximum and

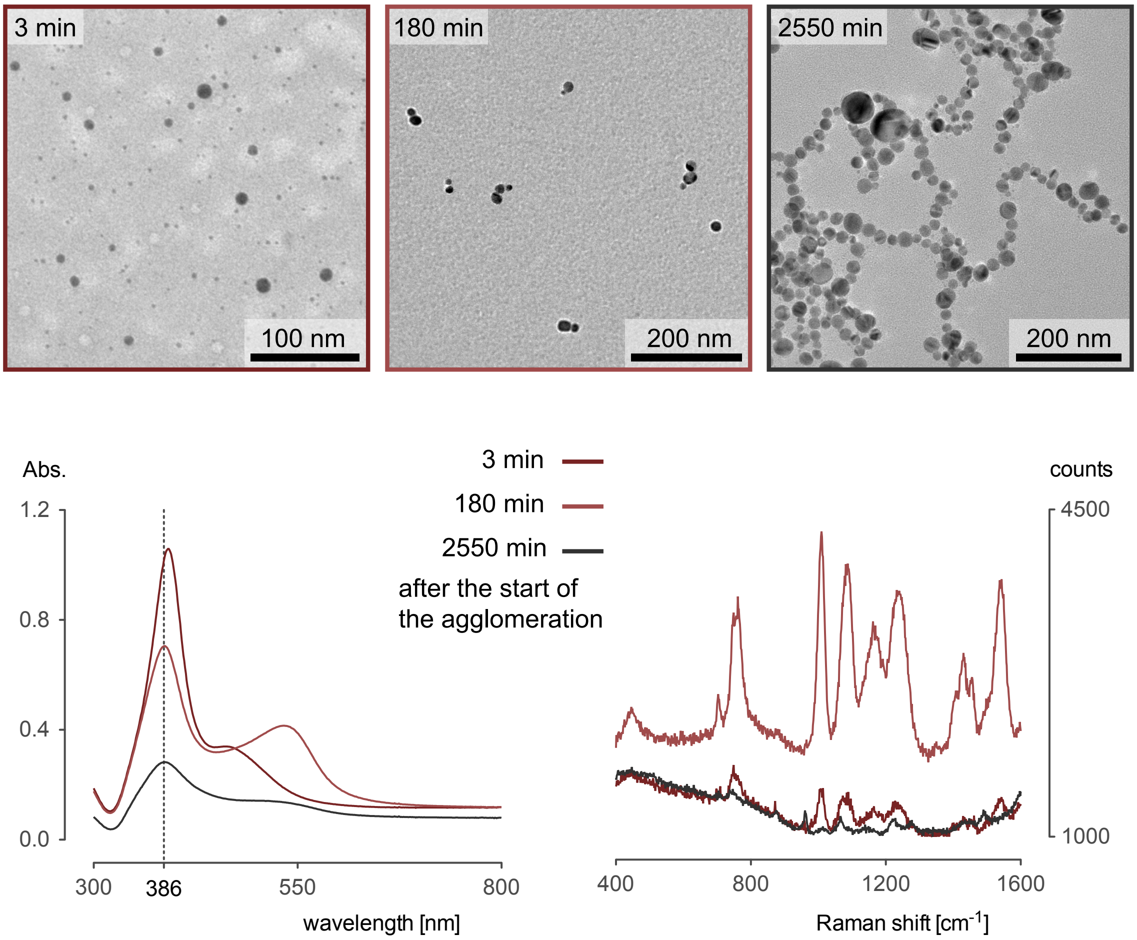

Figure 4.2.4.. TEM images show different agglomeration stages of the ATZ stabilized silver colloids. The formation of small agglomerates causes a high SERS signal of the stabilizer. In the UV/Vis spectra the formation of a new peak in the low energy region reveals the formation of agglomerates.

finally will decrease. That is exactly what has been observed for the agglomeration process of the silver sol stabilized with ATZ as shown in the contour plot in figure 4.2.5. Starting from a Raman scattering intensity of the ATZ in the initial reaction mixture (at 0 min), that is just slightly stronger than that measured in absence of the silver nanoparticles, a significant increase followed by a slow decrease of the Raman intensity are observed upon nanoparticle formation and aggregation. The same results could be found for the silver sols stabilized with MTZ. Comparing the Raman spectra of the MTZ for all different agglomeration stages reveals an increase in Raman scattering intensity from the yellow to the orange and red solutions and a diminishment for the purple solution (see figure 4.2.2).

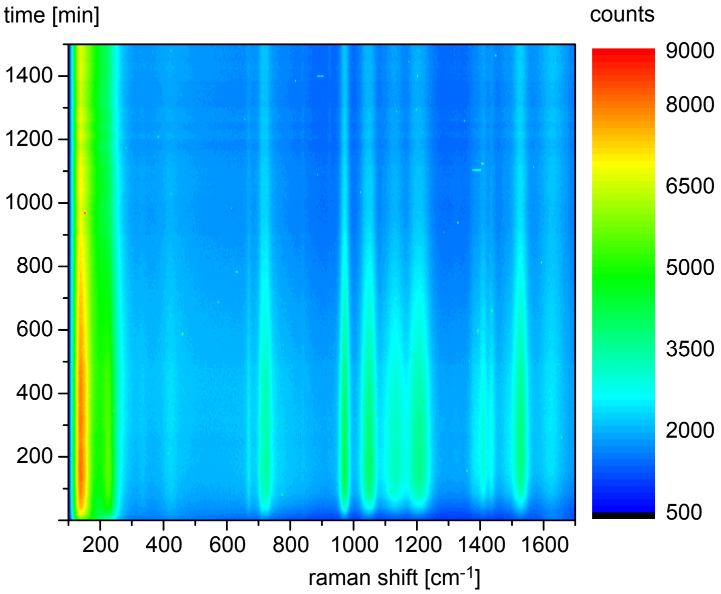

Figure 4.2.5.. In the beginning of the agglomeration of the ATZ stabilized silver nanoparticles the intensity of the SERS signal increases very quickly because of the formation of SERS "hot spots". Due to the coalescence of the particles and the precipitation of the agglomerates the signal intensity decreases slowly over time.

Figures 4.2.2 and 4.2.4 show detailed SERS spectra of MTZ and ATZ stabilized silver sols, respectively. Between 600 cm^{-1} and 1500 cm^{-1} both samples show various bands that are mainly originating from different ring vibrational modes. At 230 cm^{-1} the Ag-N stretching-vibration appears, which proves that the tetrazoles are bond to the nanoparticle surface. The spectrum of the ATZ stabilized sol exhibits an additional band at 1540 cm^{-1}. This could be assigned to the NH_2-scissoring vibration. The lack of the NH mode at 1286 cm^{-1} leads to the assumption that the nitrogen atom at positon "1" in the ring of the ATZ is deprotonated and hence the tetrazole is negatively charged.[132]

Since the tetrazoles are probably bound to the surface via the ring nitrogen atoms, the amine group in ATZ and the methyl group in MTZ are pointing away from the particle surfaces. This could be the reason for the different agglomeration behaviors of the two sols because the amine groups can interact via hydrogen bonds whereas the methyl terminated nanoparticles cannot. Therefore the ATZ stabilized sols agglomerate faster.

4.3. Tetrazole stabilized silver nanoparticles as promising building blocks for SERS substrates

In the last section the presence of the stabilizing agents on the surface has been used to follow the agglomeration process of the particles. An increase in intensity of the Raman spectra of the tetrazole due to the formation of “hot spots” could be observed. However, facing practical sensing applications the surface of the metal nanoparticles should be completely free of any molecules to make it accessible for the analyte molecules. Since tetrazole decomposes already at a temperature of about 160 °C into solely gaseous products, the idea was to thermally remove the stabilizing agents from the surface of the silver nanoparticles to end up with a blank metal surface.

The silver nanoparticles obtained from the above described synthesis show a quite broad size distribution with diameters in the range of 8-25 nm. Their plasmon resonance position was found at 397 nm. The plasmon band is asymmetrically broadened towards lower energies. This can be attributed to the large size distribution and to the partial formation of particle dimers (see figure 4.3.1). A further agglomeration into particle oligomers or bigger networks, like for the ATZ and MTZ stabilized silver nanoparticle solutions was not observed.

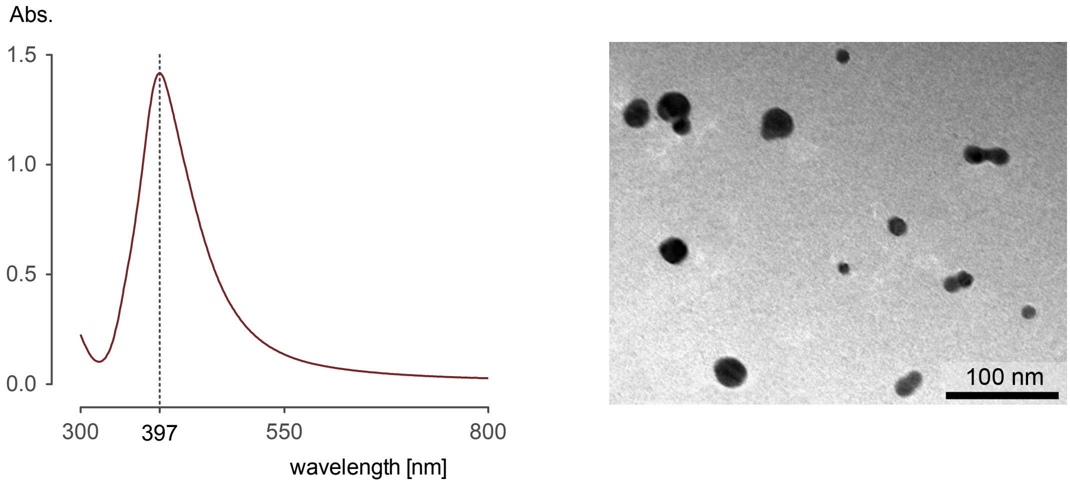

Figure 4.3.1.. A broad size distribution of the tetrazole stabilized silver nanoparticles and the presence of particle dimers cause an asymmetrically broadened plasmon band.

4.3.1. Stability of the silver colloids

Over a time period of about two weeks the yellow color of the TZ stabilized silver colloids dulls until it finally disappears. At the same time small light yellow needle-like crystals precipitate. They are insoluble in water, ethanol and acetone. One of the crystals was dried and prepared for a single crystal X-ray analysis. The new substance was found to crystallize in the monoclinic space group $P121/n1$ (Herrmann-Mauguin). The cell parameters could be determined to:

$$\begin{aligned} \boldsymbol{a} &= 5.7528\,\text{Å} & \boldsymbol{\alpha} &= 90.0° \\ \boldsymbol{b} &= 14.6876\,\text{Å} & \boldsymbol{\beta} &= 94.216° \\ \boldsymbol{c} &= 8.3251\,\text{Å} & \boldsymbol{\gamma} &= 90.0°\ . \end{aligned}$$

From the X-ray analysis the elemental ratio of Ag, C and N is 1 : 1 : 4. This exactly corresponds to a one-to-one ratio of silver to tetrazole. In the structure the silver atoms show different coordination symmetries. They alternately have trigonal planar and tetrahedral coordination geometries, respectively (see figure 4.3.2).

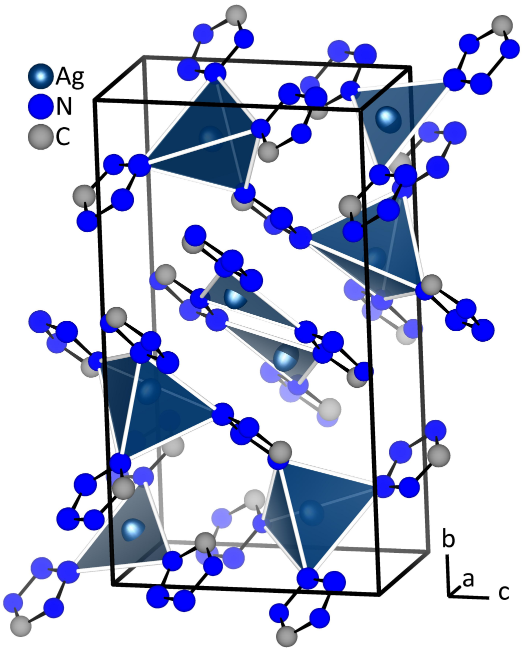

Figure 4.3.2.. The crystal structure of silver tetrazolate shows that silver ions are alternatingly in a trigonal planar and a tetragonal coordination geometry.

It is known that in aqueous solutions of silver nanoparticles the concentration of silver ions increases over time compared to the point just after the synthesis.[133] Probably the dissolved oxygen from the air is capable to oxidize the elemental silver to silver ions. The redox potential is of course dependent on the concentration of the silver ions. Therefore the dissolution of the nanoparticles stops when a certain concentration of silver ions is reached. If now the silver ions together with the tetrazole can form an insoluble silver tetrazolate, the silver ions are removed from the equilibrium of the redox couple. Hence, the silver particles can dissolve completely over time, while the silver tetrazolate is formed.

4.3.2. Formation of silver nanoparticle films

For sensing applications the silver nanoparticles need to be immobilized on substrates. This provides a better reproducibility for quantitative analysis and makes an exposure to the analyte easier. Two different strategies have been used to attach the silver nanoparticles from the aqueous solution to a glass substrate.

One protocol uses an electrostatic attachment of the particles, like known from the layer-by-layer technique. Therefore the glass substrates were cleaned in an ultrasonic bath once with acetone and afterwards twice with water for 15 min each. To obtain a positively charged substrate surface the glass slides were immersed in a 0.5 M solution of the cationic polymer polydiallydimethylammonium chloride. After 30 min the slides were removed and excessively rinsed with water. Now the positively charged substrates were dipped into a tetrazole stabilized silver colloid solution. To ensure a good coverage the substrates were left in the solution for 12 to 24 h.

In another approach the glass slides were cleaned in 10 % Extran solution, boiling water and finally rinsed with ethanol. Afterwards the substrates were immersed in a 3 % 3-aminopropyltriethoxysilane solution in ethanol for 2 h. The substrates were again rinsed with ethanol and dried in stream of nitrogen. With this method a good coverage of the particles on the substrates could be achieved after 3 h of dipping the glass slides into the tetrazole stabilized silver colloid solutions.

Raman spectra of the as prepared films were acquired using a 633 nm He-Ne laser with a power of 17 µW / μm^2 at the sample. The spectrum exhibits a very strong band at 240 cm^{-1} that originates from a silver nitrogen vibration (see figure 4.3.3). All other peaks around 1200 cm^{-1} can be attributed to stretching and in-plane bending ring vibrations of the tetrazole.[134]

After heating the substrates for 2 h at 180 °C to remove the tetrazole from the surface

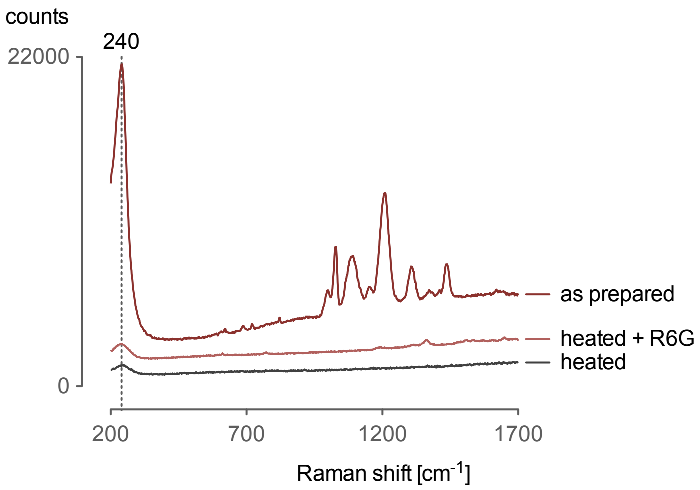

Figure 4.3.3.. The as prepared tetrazole stabilized silver nanoparticles show a high SERS signal of the stabilizer. After annealing the signal intensity is decreased and rhodamine 6G could just be detected in high concentrations, which means that the SERS activity is lost during the heat treatment.

of the nanoparticles another Raman spectrum has been recorded. The overall intensity decreased considerably and all peaks except the one at 240 cm^{-1} disappeared. Obviously the tetrazole had been removed from the surface.

In order to test the enhancement properties of the obtained substrates 10 µl of a methanolic solution of the dye rhodamine 6G (R6G) was dropped on an approximately 1 cm^2 large part of the substrate. After the evaporation of the solvent the Raman spectra were recorded. The concentration of the R6G solution was increased until a signal that could be assigned to vibrational modes of the dye was measured. For a final concentration of 10^{-3} M some very weak signal originating from R6G vibrational modes can be seen as well as an increase in the background intensity. The increase of the background is due to the fluorescence of the dye.

The measured intensity is only slightly higher than on a blank glass substrate. Hence, after the annealing of the substrates, most of the silver nanoparticles are not present anymore since the enhancement of the Raman signal is lost. It is believed that the elemental silver is oxidized during the heating process. An annealing of the substrates in an inert atmosphere leads to the same results. Therefore the silver nanoparticles are presumably oxidized by the tetrazole itself or by one of the products of its decomposition.

4.4. Résumé

It could be shown that tetrazole and its derivatives are possible stabilizing agents in the synthesis of silver nanoparticles. The evolution of physical properties related to different agglomeration stages have been investigated by UV/Vis and Raman spectroscopy as well as TEM measurements. For MTZ the state of agglomeration can be tuned and will be stable for several days, whereas for ATZ stabilized silver nanoparticles the agglomeration process cannot be stopped after it has been initiated. Silver colloids stabilized with TZ show no developing agglomeration effects. However, it can be found, that the silver nanoparticles dissolve over a time of about two weeks and meanwhile an insoluble silver tetrazolate is formed. The attempt to use the tetrazol stabilized silver nanoparticles as efficient SERS substrates could not be accomplished.

5. Formation of zinc oxide/noble metal mixed gels[‡]

In the present chapter the fabrication of different zinc oxide/noble metal mixed aerogels will be presented. It was found that by changing the conditions of the controlled destabilization of the zinc oxide sol, the morphology of the final aerogel can be tuned. The specific surface areas ranged from $44\,\mathrm{m^2/g}$ to $295\,\mathrm{m^2/g}$ and it was possible to load the gels with up to $6\,w\%$ of gold and palladium, respectively. Finally it was found that a sponge-like zinc oxide/palladium aerogel has an outstanding selectivity towards the semi-hydrogenation of acetylene of up to 85 %.

5.1. Why combinations of metal oxides and noble metals are needed?

Economic interests have been always a motivation for scientific research. Nowadays, most of the products from the chemical industry are produced with the aid of catalysts. Therefore it is highly desirable to improve the efficiencies of the known catalysts or to introduce new systems and hence increase the savings of energy and resources. Especially the field of heterogenous catalysis is very interesting since most of the industrial processes use these kind of catalysts.

The combination of metal oxides and metals is one of the most common systems in heterogenous catalysis. They are used as auto exhaust catalysts, for the synthesis of methanol, for hydrogenation reactions, in the water-gas shift reaction and in the steam reforming of methanol, just to name a tiny collection.[135;136] The metal always is directly involved in the catalytic process, whereas the metal oxide can either be just the support, a co-catalyst or responsible for a size selectivity like in zeolites.

In this work the choice of the metal oxide was confined to zinc oxide, due to its

---

[‡] The results of this chapter were mainly obtained within the framework of the master thesis written by M.Sc. Stefan Klosz under the mentoring of the author.

ease of preparation, its non-toxicity and its promising chemical and electronic properties.[137–139] Porous zinc oxide can for example be prepared using solvothermal[140], sol-gel[141;142] or gas phase deposition techniques[143;144]. Following the sol-gel process monolithic zinc oxide aerogels have been obtained.

As noble metals palladium and gold have been chosen in the present study. Whereas palladium, especially for hydrogenation reactions, is a well known catalytically active material, the potential of gold in catalytic applications was only studied extensively during the last ten years.[145;146] It has been found that combinations of zinc oxide and gold can be used for example as photocatalyst[147] or for the catalysis of the CO oxidation[148]. The most common application of zinc oxide and palladium catalysts is in methanol steam reforming.[149–151] It has also been shown that this mixed catalyst is very efficient in promoting the hydrogenation of acetylene.[152] Besides it has been found that with the aid of a zinc oxide palladium catalyst it is possible to partially oxidize methanol to obtain hydrogen and carbon dioxide.[153]

5.2. Experimental procedure to sponge-, flake- and ribbon-like gels

All gels presented in this work were obtained by the controlled destabilization of a zinc oxide sol. By changing the method of the destabilization it was possible to influence the final morphology of the gels. The synthesis of the zinc oxide nanoparticles has been adapted from a method proposed by Althues.[154]

First of all 2.2 g of zinc acetate were dissolved in 100 ml of ethanol under reflux. Afterwards the solution was cooled down to 40 °C and 50 ml of a 140 mM solution of sodium hydroxide in ethanol were added. The solution was then stirred for 2.5 h at the same temperature. Finally the zinc oxide sol was filled into polyethylene bottles and stored in the dark for further use. It was found that the storage of the zinc oxide nanoparticle solution in polyethylene bottles increased their stability from several days to several weeks compared to a storage in glass bottles. Up to now this effect has not been understood completely.

Preparation of sponge-like Solvogels and Aerogels

The sponge-like gels were produced by the destabilization of the zinc oxide sol using hydrogen peroxide. This method has already been applied successfully for the formation of semiconductor and noble metal aerogels, respectively.[111;114] Briefly, 20 ml of the zinc oxide sol were mixed with 3 ml of a 30 % hydrogen peroxide solution under stirring. After 5 h the gelation was finished and the resulting solvogel was washed with acetone 5-6 times over a period of three days. To finally obtain the aerogels the acetone was removed using supercritical CO_2 drying. This was necessary to maintain the pore structure since a conventional drying by simple solvent evaporation will cause a collapse of the structure due to capillary forces.

A loading of the zinc oxide gel was achieved by the *in situ* reduction of a palladium precursor during the gel formation process. Therefore the destabilization was started as described above. One hour later 20 mg of palladium acetylacetonate were dissolved in the turbid mixture under stirring. The palladium precursor was reduced by adding 20 ml of an aqueous 40 mM sodium borohydride solution in four steps. The turbid white solution turned into dark brown and the gel formation was allowed to finish over night without stirring. Finally the solvogel was washed several times with acetone and the aerogel was obtained by supercritical drying.

Preparation of flake-like Solvogels and Aerogels

In contrast to the other morphologies the flake-like gels could just be prepared as mixed gels. Here the destabilization of the zinc oxide sol was initiated by the addition of an aqueous solution of a metal precursor. Therefore 3 ml of a 12 mM solution of either hydrogen tetrachloroaurate or hydrogen tetrachloropalladate in water was added to 20 ml of the zinc oxide sol. The gel formation took place within several hours. For the formation of the aerogel the samples were washed again with acetone and dried with the aid of supercritical CO_2.

Interestingly, the metal precursors are reduced without the need for any additional reducing agents. Furthermore it was found that the formation of a voluminous gel was just possible in plastic vessels. Although the metal precursors were also reduced in glass vessels the zinc oxide/metal solid just precipitated without forming a porous structure.

Preparation of ribbon-like Solvogels and Aerogels

Solvogels and aerogels that are composed of very thin ribbons could be produced by mixing the zinc oxide sol with water. A mixture of water to sol at a ratio of 1:2 was found to be the optimum for the formation of monolithic gels. By adding colloidal solutions of noble metals instead of water it was possible to obtain mixed gels. Therefore the gold and palladium nanoparticle solutions were prepared freshly by the reduction of the respective metal precursors with sodium borohydride. It should be emphasized that no stabilizers are present in the synthesis of the noble metal sols. This has two reasons. First, it was tried to keep the overall content of organic compounds as low as possible since organic residues will impair the catalytic activity of the mixed gels. Second, and more important, the commonly used sodium citrate precipitates in an alkaline ethanolic solution.

For the preparation of the sample ZnO/AuNP, 5 ml of the zinc oxide sol were mixed with 2.5 ml of a gold nanoparticle solution. The gold nanoparticle solution was prepared by diluting 3 ml of a 5 mM solution of $H[AuCl_4]$ to a total volume of 50 ml followed by an injection of 0.5 ml of a freshly prepared 50 mM $NaBH_4$ solution under vigorous stirring. To achieve higher loadings the concentration of the gold nanoparticle solution was increased by reducing the total volume to one-tenth while keeping the amount of the substances constant. The resulting sample is denoted $ZnO/AuNP_{conc}$.

A second method to produce gels with a high loading of gold nanoparticles was the *in situ* reduction of the gold precursor. Therefore 3.75 µl of a 200 mM $H[AuCl_4]$ solution was added to 5 ml of the zinc oxide sol followed by the quick injection of 2.5 ml of a 10 mM $NaBH_4$ solution. The resulting sample is denoted $ZnO/AuNP_{in\ situ}$.

The preparation of the palladium containing samples was analogous to that described for gold. Simply the gold precursor was replaced by the same amount of the palladium precursor. As palladium precursor a solution was prepared by dissolving palladium chloride with four equivalents of sodium chloride to obtain sodium tetrachloropalladate.

5.3. Properties of the different gels

The sponge-, flake- and ribbon-like structures were characterized by electron microscopy, thermo analysis, energy-dispersive X-ray spectroscopy, UV/Vis spectroscopy and nitrogen physisorption.

5.3.1. Structure on the nanoscale and metal loading

SEM investigations reveal the different morphologies of the aerogels (see figure 5.3.1). The sponge-like gels are made of a chain-shaped nanowire network. It was found that the diameter of the chains is approximately 10 nm which is about the same size as the diameter of the initial zinc oxide nanoparticles. This structure is similar to those that have been reported for semiconductor and noble metal aerogels.[111;114] Probably the addition of hydrogen peroxide caused a decrease in the absolute zeta potential of the sol. The resulting destabilization of the sol makes the zinc oxide nanoparticles to arrange into chains because of dipole-dipole interactions. These chains finally formed the porous network.

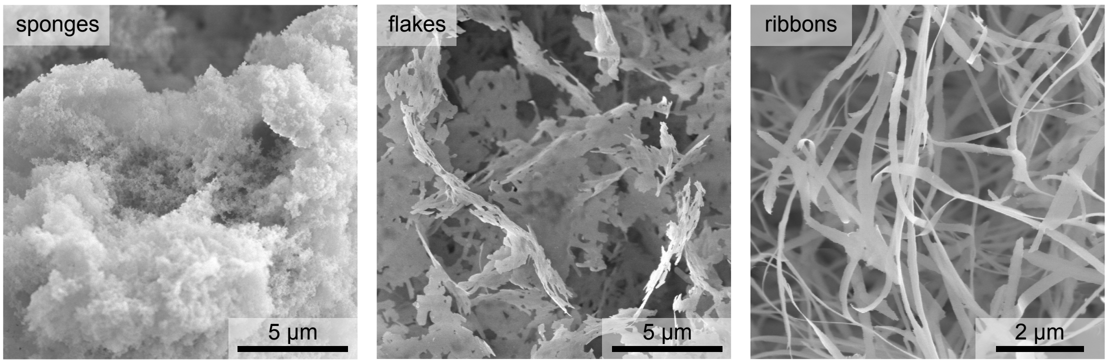

Figure 5.3.1.. SEM micrographs show the different morphologies of the aerogels. The morphology of the respective gels remained unchanged for different noble metal loadings.

The flake-like gels are built of porous sheets with lateral dimensions of several micrometers and a thickness of 10-20 nm. A similar structure was found for the ribbon-like gels. Here the planar structures are of the same thickness but form dense ribbons that are about 200 nm broad and several tens of micrometers long. For both flake- and ribbon-like gels the zinc oxide nanoparticles completely rearrange into new structures. Neither of those show the initial spherical particles as part of their structure. This means that the zinc oxide nanoparticles have to at least partly dissolve and grow into the new morphologies. Probably the addition of water caused a partial hydrolysis of the zinc oxide to zincates. It is assumed that these zincates can undergo a polycondensation and form coordination polymers which built up the planar structures.

Using EDX the relative amount of the noble metals in the gels was investigated (see table 5.3.1). It should be mentioned that the values for the oxygen and the carbon content have to be considered critically. Because of the low atomic mass of these elements the uncertainty in the determination using EDX is relatively high. Another inaccuracy emerges from the porous nature of the materials investigated. It is possible that re-absorption effects distort the outcome of the EDX measurements. However, comparing the obtained mass fractions with each other it is still possible to classify the metal loadings of the respective gels relative to each other. Therefore it can be seen that the metal loading of the ribbon-like gels was higher for the samples prepared *in situ* than for those prepared with a concentrated nanoparticle

Table 5.3.1.. The elemental composition of the samples was investigated using EDX. It was found that metal loadings of more than 6 w% can be achieved using the methods presented.

sample	Zn [w%]	O [w%]	Pd [w%]	Au [w%]	C [w%]
ZnO sponge	64.7	16.3	-	-	19.0
ZnO/Pd sponge	68.0	20.2	3.1	-	8.8
ZnO/AuNP ribbons	55.1	19.7	-	0.3	24.9
ZnO/AuNP$_{\text{conc}}$ ribbons	65.1	17.2	-	4.9	12.8
ZnO/AuNP$_{in\ situ}$ ribbons	62.1	17.2	-	6.1	14.6
ZnO/PdNP$_{\text{conc}}$ ribbons	61.8	19.0	2.1	-	17.2
ZnO/PdNP$_{in\ situ}$ ribbons	61.8	18.5	2.8	-	17.0
ZnO/PdNP flakes	61.3	17.7	6.4	-	14.6

solution. This might be due to an enhanced agglomeration of the prepared concentrated solutions and thus be just because of a lower initial amount of the metal. From TEM micrographs (see figure 5.3.2) of the flake-like gels it can be seen that

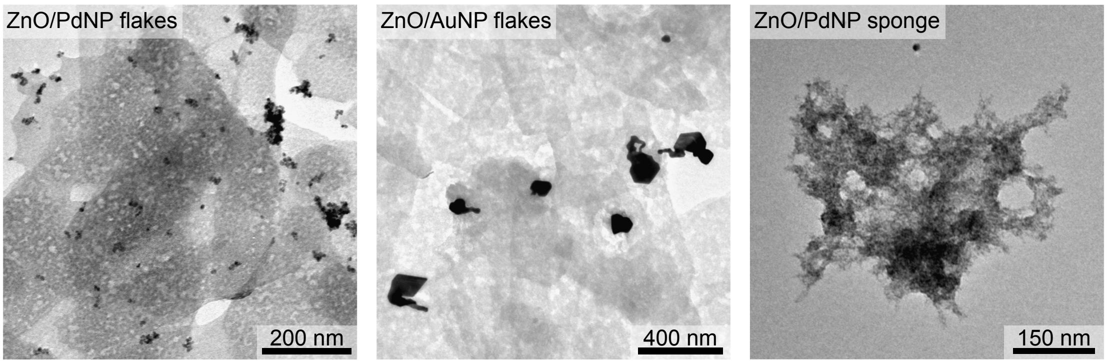

Figure 5.3.2.. From TEM investigations it can be seen that the flakes are formed of interlaced ribbons. Besides the palladium nanostructures on the flake-like gels are much smaller and better dispersed than the gold nanostructures. For sponge-like gels a very fine structure with well dispersed small palladium nanoparticles can be seen.

the gold nanoparticles are much larger (50-200 nm) than the palladium nanoparticles (5-15 nm). This is probably due to a faster nucleation of the palladium nanoparticles. Furthermore it can also be seen that the zinc oxide flakes are actually made of interlaced ribbons. The sponge-like aerogels are build of a very fine network of zinc oxide chains and the palladium is well dispersed across the gel.

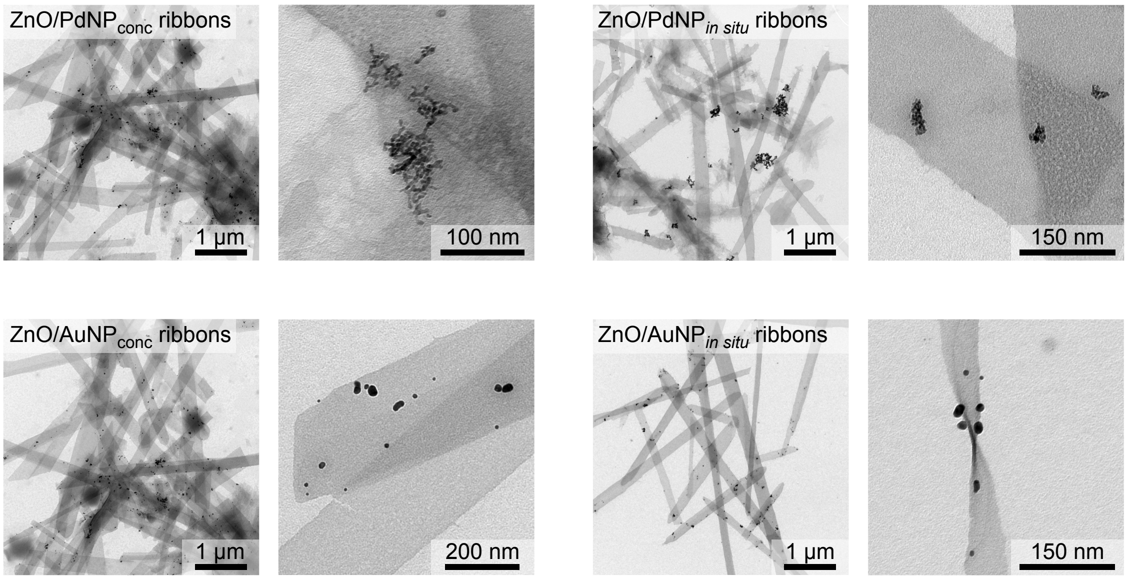

Figure 5.3.3.. Independent of the method, it can be seen from TEM images that the palladium forms very small network-like nanostructures, whereas the gold forms larger single particles on the surface of the zinc oxide ribbons. Furthermore it is obvious that the *in situ* method leads to less dispersed metal nanostructures.

Obviously, the method of how the metal nanoparticles are formed on the ribbon-like gels has an influence on their final structure (see figure 5.3.3). For both metals it can be seen that the particles are more evenly distributed across the zinc oxide ribbons in the case of using a concentrated solution than using the *in situ* method. Furthermore a significant difference in the metal nanostructures was found comparing palladium and gold loaded gels. Gold forms almost spherical nanoparticles with diameters of 10-30 nm. The size and shape do not differ significantly for both loading techniques. For the palladium nanostructures a completely different morphology can be seen. In both methods they form small networks of particles with a size of about 10 nm, whereas these networks are much denser in the *in situ* method. Similar structures for palladium have been reported for palladium aerogels.[155] This is not surprising since the method of the particle synthesis is very similar.

5.3.2. Optical properties of ribbon-like gels

A distinct influence of the metal loading on the optical properties of the solvogels and aerogels can already be seen by eye (see figure 5.3.4). Pure zinc oxide is a direct semiconductor with a band-gap-energy in the UV-region and therefore shows a white color. The strong plasmonic resonances of gold nanostructures in the visible range cause the pink and purple color of the gold containing gels. As discussed earlier in chapter 1 the plasmon resonance position as well as the intensity of the plasmon band depend strongly on the refractive index of the embedding medium. This effect causes the color change between the respective solvogels and aerogels. The relatively small and well separated gold nanoparticles on the gel with a lower gold concentration are responsible for its pink appearance. For gels with a higher gold loading the nanoparticles were larger, less spherical and tended to form agglomerates. Therefore the color is changed to purple.

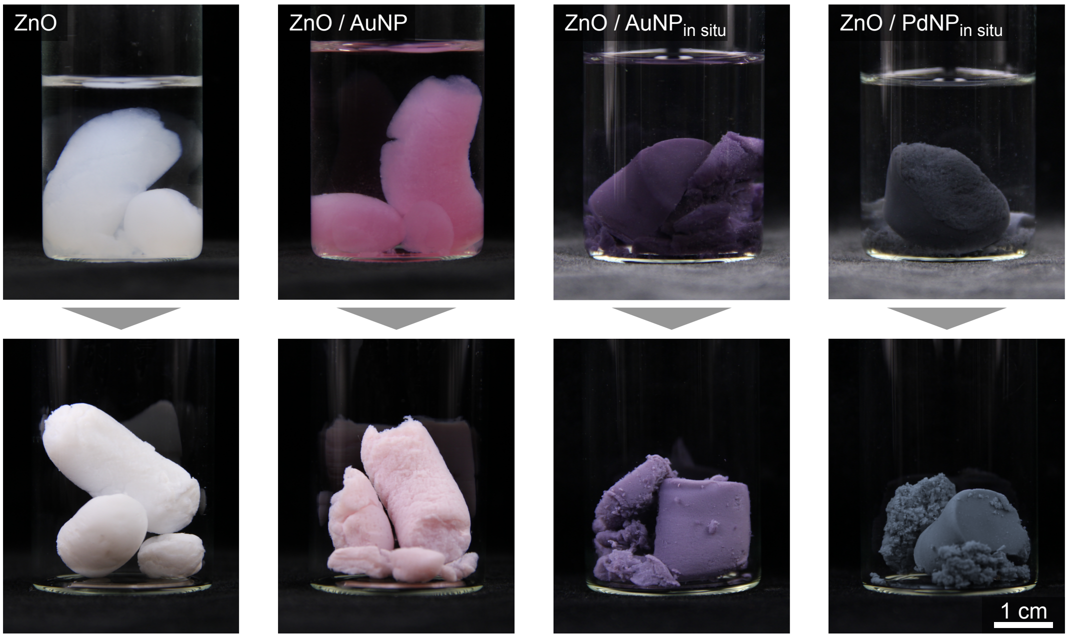

Figure 5.3.4.. It can be seen from the photographs that the shape of the solvogels can be preserved during supercritical drying. Especially the color of the gold sols directly indicates the presence of nanoscale noble metal particles. Scale bar is the same for all pictures and is shown in the bottom right.

Single palladium nanoparticles show a plasmon resonance in the UV-region.[156] However, as it was found from TEM investigations the palladium nanostructures on the gels are small network-like agglomerates. Pure palladium aerogels that are made of these network-like structures are completely black.[155] This is due to an extensive coupling of the single particle plasmons across these agglomerates. The combination of the white zinc oxide with the black palladium structures results in the gray appearance found for the mixed gels.

Absorbance spectra were obtained from diffuse reflectance measurements of the samples in an integrating sphere. The pure zinc oxide gel just shows the expected absorption starting below 400 nm (see figure 5.3.5). For the gels loaded with gold nanoparticles the plasmon band can clearly be identified at about 520 nm. Furthermore it can be seen that the absorbance for the gels with a higher gold concentration is increased significantly. Besides the plasmon band is shifted slightly to the red which is due to larger particle sizes and an increased degree of agglomeration of the gold nanoparticles. Especially in the low energy region the spectra of the two samples with the higher concentration differ from each other. The stronger coupling in this part of the spectrum can be attributed to a more pronounced agglomeration in the *in situ* sample than in the other one.

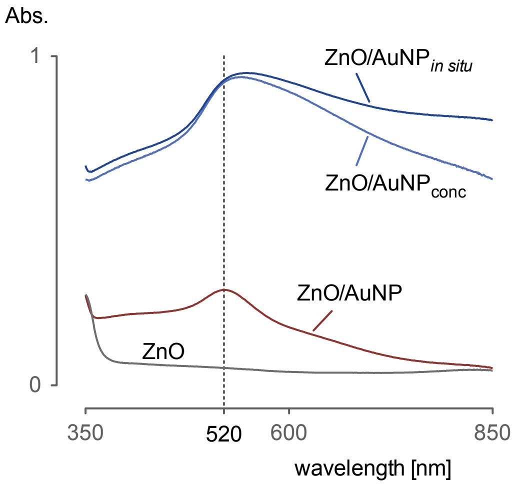

Figure 5.3.5.. From the UV/Vis spectra of the zinc oxide/gold mixed aerogels the plasmon resonance of the gold nanostructures can clearly be seen. Besides the higher loading with gold leads to a higher absorbance.

5.3.3. Specific surface areas and thermal properties of the gels

The surface areas of the aerogels were obtained from nitrogen physisorption isotherms (see figure 5.3.6). Therefore the data between a relative pressure of 0.1 and 0.3 have been fitted to a Brunauer-Emmett-Teller (BET) isotherm. It was found that the flake-like and the ribbon-like aerogels have a comparable specific surface area of about 40-50 m^2/g, whereas the sponge-like aerogels have a surface area of up to 300 m^2/g.

All samples show a type II physisorption isotherm.[157] The strong increase of the adsorbed volume for very high relative pressures indicates the presence of mainly macropores (>50 nm), which is in good agreement with the results from SEM investigations (see figure 5.3.1). For the ribbon-like gel the slope of the isotherm already increases at a relative pressure of about 0.4. This is commonly attributed to the presence of mesopores (2-50 nm). Here it is most probably due to the condensation of the nitrogen in the slit-pores between different ribbons because there are no other kinds of pores identifiable from electron microscopic investigations.

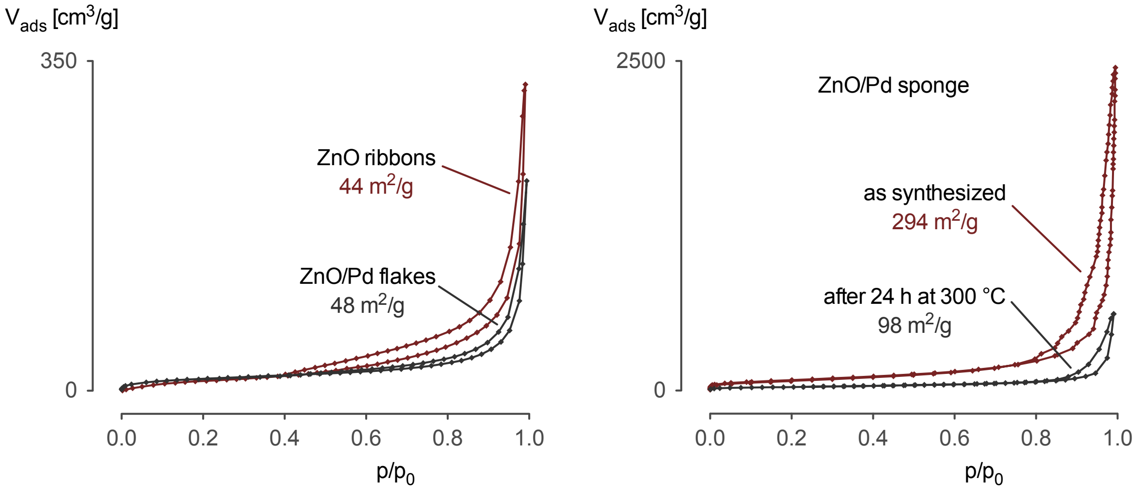

Figure 5.3.6.. The nitrogen physisorption isotherms of all samples are characteristic type II curves. A strong increase of the adsorbed nitrogen volume indicates the presence of mainly macropores in all samples. The specific surface areas were determined using a multipoint-fit of the BET isotherm to the relative pressure range of 0.1-0.3.

For all aerogel samples presented in this work the thermal response was essentially the same. Exemplary the response of the mixed zinc oxide/palladium aerogel $ZnO/PdNP_{in\ situ}$ will be discussed (see figure 5.3.7). For the TG and DTA measurement 16.23 mg of the sample were heated with a rate of 3 K/min under synthetic air.

A relatively low mass loss of about 5 % was observed during heating to about 120 °C. Since there is no significant signal in the DTA curve this is attributed to the removal of loosely bound residues of acetone and ethanol. The major mass loss of about 15 % took place at around 126 °C. This was accompanied by an endothermic response in the DTA curve and is attributed to the removal of adsorbed water from the zinc

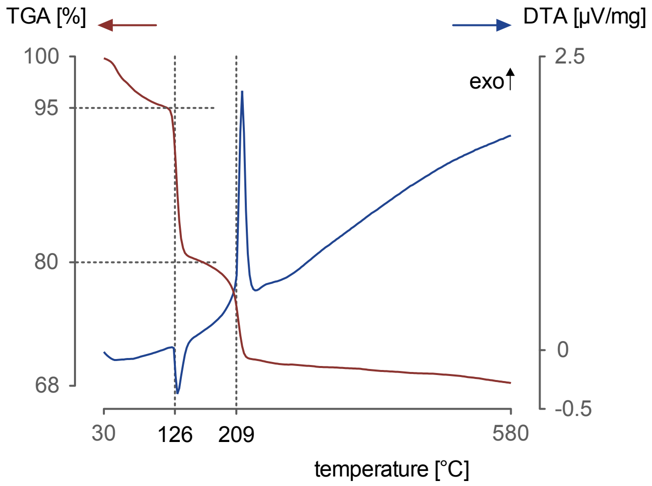

Figure 5.3.7.. From the thermal investigations of a palladium loaded ribbon-like gel two major mass losses can be seen. The first one which is endothermic is attributed to the removal of water and the second exothermic mass loss is believed to be due to an oxidative removal of organic compounds.

oxide structures. The origin of the next exothermic mass loss at 209 °C could not be clarified completely. It is believed that it is an oxidative removal of some organic compounds. However, it was not possible to assign the response to a certain substance. Residues of acetate from the zinc precursor can be excluded since they will decompose at temperatures of around 300 °C.[158;159] Possibly the decomposition of the proposed coordination polymer will be responsible for the mass loss at this temperature but further research is needed to understand the thermal behavior of the aerogels completely.

5.4. ZnO/Pd aerogels for highly selective acetylene hydration

Nowadays polyethylene in all its modifications is the most common plastic. Especially the leading role in the production of packing materials makes polyethylene a highly desirable material. With the use of new polymerization catalysts polyethylene became available very cost-efficiently and the world wide demand is increasing ever since. Normally, the raw-material ethylene is produced by means of the pyrolysis of fossil fuels. This procedure, however, yields a significant amount of by-products. Particularly the formation of acetylene is critical since it will cause a poisoning of the catalysts used in the polymerization of ethylene.

Therefore it is necessary to remove the acetylene, or even better to transform the acetylene to ethylene. Commonly this is achieved in industry with the aid of palladium catalysts.

Because of its high surface area and the relatively large palladium loading the sponge-like structure of a zinc oxide/palladium aerogel was chosen for the investigation of the catalytic activity of the materials presented. TGA investigations revealed that most of the mass loss at elevated temperatures takes place below 300 °C. Hence a preconditioning of the sample at 300 °C for 24 h was performed resulting in a reduction of the specific surface area from 294 m^2/g to 98 m^2/g. This is accompanied by a change of the color of the sample from dark grey to brownish which could be explained by the partial formation of yellow palladium oxide.

For the catalytic measurements a certain amount of the sample was mixed with boron nitride to give a final mass of 420 mg. The mixtures were then placed into a stainless steel tube. First the samples were purged with a stream of helium (40 ml/min) for 30 min. Afterwards the tube was heated to a temperature of 100 °C. At this temperature the stream of helium was charged with 10 % hydrogen to reduce the palladium oxide and to activate the palladium surface. For the investigation of the catalytic activity the samples were heated to 200 °C under helium and the stream of gas was charged with 0.5 % acetylene, 5 % hydrogen and 50 % ethylene, respectively. The composition of the product stream was monitored with a GC-MS over a time of 10 h.

The ZnO/Pd-aerogel shows a very high selectivity of more than 80 % toward the hydrogenation of acetylene to ethylene (see figure 5.4.1). By using only 0.1 mg of the aerogel it was possible to achieve a conversion of 10 % already. This could further be increased to almost 100 % by using a threefold amount of the gel. The selectivity toward the formation of C_4-derivatives was only 6 % for the second measurement. A preferably small amount of this derivatives is strongly desired since they will cause a poisoning of the catalyst.

A comparison of different materials used for the hydrogenation of acetylene shows the outstanding catalytic properties of the ZnO/Pd-aerogel (see table 5.4.1). The data for the other materials have been published by Armbrüster and colleagues.[160] All materials were measured on the same system with comparable parameters. Within the present study only the intermetallic compounds of palladium and gallium show selectivities comparable to those found for the mixed aerogel. However, the total amount of palladium in the new aerogel material is at least three orders of magnitude

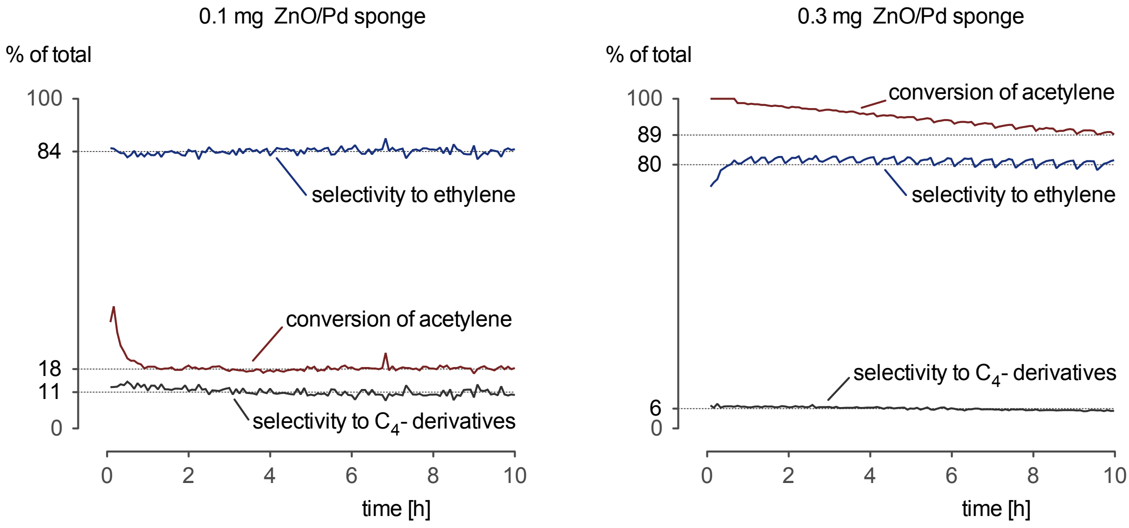

Figure 5.4.1.. From the results of the catalytic investigations at 200 °C it can be seen that the selectivity toward the semi-hydrogenation of acetylene is very high. A threefold increase of the amount of the aerogel led to a conversion of almost 100 %.

smaller than for the palladium/gallium system. Therefore the mixed aerogels are also very promising from an economic point of view. It should be mentioned that a nanoparticular BiRh intermetallic compound is the current benchmark catalyst in the semi-hydrogenation of acetylene showing a selectivity of around 90 %.[161] Because of the extremely expensive rhodium the presented mixed aerogels are still economically favorable.

In the intermetallic compounds of palladium and gallium the high selectivity has been attributed to the presence of isolated palladium atoms.[160;162] In analogy, it is proposed that the high selectivity of the mixed aerogels is due to the formation of a intermetallic zinc palladium phase. It has been shown previously that the combination of zinc and palladium could increase both selectivity and activity in hydrogenation processes and in methanol steam-reforming processes, respectively.[149–153] The assumption of the formation of an intermetallic Zn/Pd phase might be verified by the identification of different oxidation states of the zinc applying XANES or XPS measurements.

Table 5.4.1.. Already very small amounts of the mixed zinc oxide/palladium aerogel show a conversion of almost 100 % with a simultaneous selectivity towards the semi-hydrogenation of acetylene of more than 80 %. Especially with respect to the amount of palladium used this new material is several orders of magnitude more efficient than other catalysts.

sample	mass [mg]	surface area [m^2/g]	conversion [%]	selectivity [%]
PdGa	40.0	0.4	86	75
Pd_3Ga_7	100.0	0.4	99	71
Pd/Al_2O_3	0.15	5.6	43	17
$Pd_{20}Ag_{80}$	200.0	< 0.5	83	49
ZnO/Pd sponge	0.1	96	18	84
	0.3	96	95	80

5.5. Résumé

By controlling the destabilization of an ethanolic zinc oxide nanoparticle solution it was possible to obtain gels with different micro- and nanostructures. The sponge-, flake- and ribbon-like gels could all be loaded with palladium and gold nanoparticles, respectively. For sponge-like aerogels a specific surface area of almost 300 m^2/g could be determined. Smaller but still high surface areas of 40-50 m^2/g were found for the flake- and ribbon-like structures. The gold structures on the gels are made of spherical and elongated nanoparticles with a relatively broad size distribution ranging from about 5-30 nm. In contrast to the individual nanoparticles formed by gold, the palladium nanostructures are made of fine network-like agglomerates.

Finally it was found that a sponge-like zinc oxide/palladium aerogel has an outstanding activity as well as selectivity toward the semi-hydrogenation of acetylene, especially with respect to the amount of palladium used.

Conclusions and Outlook

Shape and size control as well as the control of the assembly of nanostructures are current challenges in nano sciences. Focussing on metal nanostructures all of these aspects have been addressed in the frame of the present work.

It was possible to develop a new aqueous seeded growth method that produces gold nanoparticles with adjustable diameters over a large range of sizes. The spherical particles obtained show very low polydispersities and a good long term stability. Furthermore it was possible to reveal the growth mechanism of these particles utilizing electron microscopy and optical investigations coupled with theoretical calculations. It was found that there is a formation of small nucleation sites on the surface of the seeds in the beginning of the growth process. These sites then subsequently grow into "blackberry-like" intermediate particles. A final intraparticle ripening step leads to smooth and uniform spherical gold nanoparticles. By correcting the dielectric function of gold for charging and the free mean path effect and taking into account the particle size distribution it was possible to accurately model the optical properties of the gold sols obtained using Mie theory.

By controlling the concentration of chloride ions it was possible to influence both the ripening of the "blackberry-like" shaped particles and the morphology of gold nanoparticles. An increased concentration of the chloride ions in the standard citrate reduction procedure leads to larger and elongated particles, whereas the complete removal of the chloride ions made it possible to obtain star shaped, decahedral and "desert-rose" shaped particle morphologies.

Using the layer-by-layer technique gold nanoparticles of different sizes could be immobilized on glass substrates. The surface-enhanced Raman scattering intensity of these mixed films were about 60 % higher than compared to a film made of a single particle size. The optical properties were further investigated by comparing experimentally obtained UV/Vis spectra with generalized Mie theory simulations.

Additionally it could be shown that tetrazole and its derivatives are suitable stabilizing agents in the aqueous synthesis of silver nanoparticles. It was found that depending on the tetrazole derivative used the tendencies of the nanoparticles to agglomerate vary significantly. Different agglomeration stages have been investigated by UV/Vis and Raman spectroscopy. The removal of the ligands used and a resulting improvement of the applicability of the silver nanostructures as SERS substrates is still a challenge.

In the last part of this work the focus was changed from the optical properties of noble metal nanoparticles to their catalytic properties. Therefore gold and palladium nanoparticles have been successfully immobilized on highly porous zinc oxide aerogels. It was possible to synthesize sponge-, flake-, and ribbon-like zinc oxide gels with high specific surface areas. The facile approach of generating mixed metal oxide/noble metal aerogels is very promising for the preparation of highly selective and highly active heterogenous catalysts. First catalytic investigations of a sponge-like palladium loaded zinc oxide aerogel toward the semi-hydrogenation of acetylene showed very high selectivities of up to 85 %.

Especially the last part of the present work opens a huge variety of future work. A detailed understanding of the gelation mechanism would enable a selective preparation of gels with different porosities. Besides the metal loading and the dispersion of the particles on the metal oxide need to be improved. An investigation of the efficacy of the potent material toward other reactions like the methanol steam reforming is also very promising. The to do list could be extended almost infinitely to new materials, metals, morphologies, reactions and of course a combination of all. To cut a long story short, there is still plenty of work to do - as always.

A. List of chemicals used

MilliQ water has been used throughout.

acetone (*for analysis*)	Merck
5-amino-tetrazole (95 %)	Aldrich
p-aminothiophenole (97 %)	Sigma-Aldrich
ascorbic acid (99-100.5 %)	AppliChem
n-butanol (99 %)	Grüssing
citric acid (99 %)	Grüssing
ethanol (*absolute for analysis*)	Merck
hydrogen tetrachloroaurate (99.9+ %)	Sigma-Aldrich
5-methyl-tetrazole (95 %)	Aldrich
palladium acetylacetonate (99 %)	Aldrich
palladium chloride (99.999 %)	Aldrich
polyallylamine hydrochloride	Aldrich
polydiallyldimethylammonium chloride 20 w% in water	Aldrich
rhodamine 6G	Radient Dyes Laser
silver nitrate (99.9+ %)	Sigma-Aldrich
sodium borohydride (99 %)	Riedel-de-Haen
sodium chloride (99.9 %)	VWR, AnalaR NORMAPUR
tetrazole 0.45 M solution in acetonitrile (*purum*)	Fluka
trisodium citrate	Sigma

B. Matlab Codes used in this work

B.1. Calculations of the free mean path effect

```
%
RI_CORE = importdata(’gold_JC.dat’);        %import refr. ind. of Au
RI_SM = importdata(’water.dat’);            %import refr. ind. of H2O
n=81;
D=[2 4 8 16];
id=2;
a=zeros(81,3);                              %allocating a
A=zeros(801,5);                             %allocating A

A(:,1)=400:0.5:800;

for ind=1:4
d=D(1,ind);
r=d./2;

for j = 1:n
    lambda=RI_SM.data(j,1);

    rn=RI_CORE.data(j,2);
    rk=RI_CORE.data(j,3);
    RI=RIcorr(rn, rk, lambda, r);           %mean free path correction

    m = (rn + 1i*rk)/RI_SM.data(j,2);

    x=2.*pi./RI_SM.data(j,1).*d./2.*(RI_SM.data(j,2));

    a(j,:)=Mie(m, x).*pi;                   %determin Qext
end

z=400:0.5:800;
t=RI_SM.data(:,1);
q=a(:,1);
y = interp1(t,q,z,’spline’);

A(:,id)=y;
id = id +1;

  for j = 1:n
    lambda=RI_SM.data(j,1);

    rn=RI_CORE.data(j,2);
    rk=RI_CORE.data(j,3);
    RI=RIcorr(rn, rk, lambda, r);

    m=(RI(1) + RI(2).*1i)./RI_SM.data(j,2);

    x=2.*pi./RI_SM.data(j,1).*d./2.*(RI_SM.data(j,2));
```

```
    a(j,:)=Mie(m, x).*pi;
  end

  z=400:0.5:800;
  t=RI_SM.data(:,1);
  q=a(:,1);
  y = interp1(t,q,z,'spline');

  A(:,id)=y;
  id = id +1;

end

dlmwrite('path.dat',A)                  %write results to file
```

B.2. Calculations of the effect of the embedding medium

```
%code to calculate the influence of the embedding medium on the plasmon
%resonance position, using the refractive index for gold by Johnson and
%Christry and just the drude part of the fit to the experimental values

function MieSpec_appendix(d) %d is the particle diameter in nm

RI_CORE = importdata('gold_JC.dat'); %file with ri data from J&C

EPS8 = 9;                            %Drude parameters for Au from
OMP=8.94;                            %fit to J&C data
OMO=0.072;

RI_SM=[1 1.33 1.6 2.4];              %list of ri of embedding medium

%calculation of the drude ri of gold
lambda = RI_CORE.data(:,1);
OM = 1239.86./lambda;
A1 = real(EPS8-OMP.^2./(OM.*(OM+1i.*OMO)));
A2 = imag(EPS8-OMP.^2./(OM.*(OM+1i.*OMO)));

RI_DRUDE = [sqrt(0.5.*(sqrt(A1.^2+A2.^2)+A1)) sqrt(0.5.*(sqrt(A1.^2+A2.^2)-A1))];

%defining parameters and preallocation
n=size(RI_CORE.data,1);
a=zeros(n,3);

id=2;
A=zeros(801,5);
A(:,1)=400:0.5:800;

%% plotting the spectra for the ri from J&C
figure
hold on
for ind=1:4

ri_sm=RI_SM(1,ind);

    for j = 1:n
```

```
        rn=RI_CORE.data(j,2);
        rk=RI_CORE.data(j,3);

        m=(rn + rk*1i)/ri_sm;

        x=2.*pi./RI_CORE.data(j,1).*d./2.*(ri_sm);

        a(j,:)=Mie(m, x);
    end

z=400:0.5:800;
t=RI_CORE.data(:,1);
q=a(:,1);
y = interp1(t,q,z,'spline');
plot(z,y,'k')

A(:,id)=y;
id = id +1;
end
hold off

dlmwrite('embedJC.dat',A)           %writing results to file

%% plotting the spectra for just drude dielectric function
id=2;
A=zeros(801,5);
A(:,1)=400:0.5:800;

figure
hold on
for ind=1:4

ri_sm=RI_SM(1,ind);

    for j = 1:n

        rn=RI_DRUDE(j,1);
        rk=RI_DRUDE(j,2);
        m=(rn + rk*1i)/ri_sm;

        x=2.*pi./RI_CORE.data(j,1).*d./2.*(ri_sm);

        a(j,:)=Mie(m, x);
    end

z=400:0.5:800;
t=RI_CORE.data(:,1);
q=a(:,1);
y = interp1(t,q,z,'spline');
plot(z,y,'k')

A(:,id)=y;
id = id +1;
end
hold off

dlmwrite('embedDRUDE.dat',A)        %writing results to file
```

B.3. Fit of the Dielectric Function of Gold

```
clear

inp = importdata('Au_evap');    % import ri data from J&C
lambda = inp(5:11,1).*1000;
omega = 1239.86./lambda;        % in eV
reeps = inp(5:11,4);            % just use limited region for drude fit
imeps = inp(5:11,5);


% pure drude fit to red and ir region

H=@(w)abs(w(1)-w(2).^2./(omega.*(omega+1i.*w(3)))-reeps-1i.*imeps);

w0 = [10 3 0.5];

w = lsqnonlin(H,w0,[0 0 0],[15 15 15],optimset('TolX',1e-14,'MaxIter', ...
    100000,'MaxFunEvals',100000,'TolFun',1e-14));

disp(w)         %output of the drude parameters

refit2 = real(w(1)-w(2).^2./(omega.*(omega+1i.*w(3))));

imfit2 = imag(w(1)-w(2).^2./(omega.*(omega+1i.*w(3))));

X2 = lambda;
reeps2 = reeps;
imeps2 = reeps;


% indruducing three interband transitions quasi self consistently

lambda = inp(5:30,1).*1000;
omega = 1239.86./lambda;    % in eV
reeps = inp(5:30,4);        % use full region for overall fit
imeps = inp(5:30,5);

%limits for the paramters

iblb = [-9999 -99 -99 -9999 -99 -99 1 0];
ibub = [9999 99 99 99 9999 99 3 1];


n=1;
Out = zeros(729,9);

% loop to search for global minimum

for a1 = -20:10:20
    for a2 = -20:10:20
        for a3 = -20:10:20
            for a4 = -20:10:20
                for a5 = -20:10:20
                    for a6 = -20:10:20

ib0 = [a1 a2 a3 a4 a5 a6 1.9 0.05]; %initial parameters for interband
                                    %transitions and separation function

F=@(ib)sum((abs(w(1)-w(2).^2./(omega.*(omega+1i.*w(3))) + ...
              (ib(1)./(omega.^2+1i.*ib(2).*omega+ib(3)) + ...
              ib(4)./(omega.^2+1i.*ib(5).*omega+ib(6))).* ...
              (1./(exp((ib(7)-omega)./ib(8))+1)) ...
              - reeps-1i.*imeps)).^2);
```

```
%the routine fminsearchbnd can be downloaded at matworks
ib = fminsearchbnd(F,ib0,iblb,ibub,optimset('TolX',1e-12,'MaxIter',10000,...
                   'MaxFunEvals',10000,'TolFun',1e-12));

Res =    sum((abs(w(1)-w(2).^2./(omega.*(omega+1i.*w(3))) + ...
              (ib(1)./(omega.^2+1i.*ib(2).*omega+ib(3)) + ...
             ib(4)./(omega.^2+1i.*ib(5).*omega+ib(6))).* ...
             (1./(exp((ib(7)-omega)./ib(8))+1)) ...
             - reeps-1i.*imeps)).^2);

Out(n,:) = [Res ib];

disp(n)

n=n+1;

                    end
                end
            end
        end
    end
end

ind = Out(:,1) == min(Out(:,1));

disp(Out(ind,:))        % output of the parameters for the lorentzians and
                        % the separation function
```

B.4. Generation of random sphere films

```
%% Script to generate a random assembly of spheres on a 1x1 micron^2 area
%  where the spheres cover 30% of the substrate
d=100;          %input for sphere diameter
c=0.3;          %desired coverage
ns=round(1000000*c/(pi*(d/2)^2));   %calculate number of spheres needed
B=zeros(ns,2);                      %allocating vector for sphere coordinates
B(1,:)=[round((1000-d)/2) round((1000-d)/2)];   %first sphere in the middle
t=1;
j=2;
while j <= ns && t <1000000
    x=((1000-d)*rand);
    y=((1000-d)*rand);
    P=[x y];
      if sqrt((P(2)-B(:,2)).^2 + (P(1)-B(:,1)).^2)>=d+2
        B(j,:)=P;
        j=j+1;
      end
    t=t+1;
      if t>=1000000
          disp('coverage not reached')
      end
end
%% plot of the generated structure
figure
axis equal
xlim([0 1000])
ylim([0 1000])
hold on
for rect=1:ns
```

```
pos = [B(rect,1)-d/2 B(rect,2)-d./2 d d];
rectangle('Position', pos, 'Curvature',1,'LineWidth',0.1,...
         'facecolor',[0.83 0.68 0.23]);
end
hold off
%% writing an input file for the GMT simulations
F(:,1:2)=B./1000;
F(:,3) = 0.0;
F(:,4) = (d/2)/1000;
F(:,5) = 0.18344;
F(:,6) = 3.4332;
dlmwrite('tmp.k',0.633)
dlmwrite('tmp.k',ns,'-append')
dlmwrite('tmp.k',F,'delimiter','˜','-append')
```

B.5. Generation of random agglomerates

```
%% Script to generate a random agglomerate of spheres
ns=14; %number of spheres in agglomerate
d=78; %diameter of the spheres
s=d+1;
B=zeros(ns,2);
B(1,:)=[0 0];
j=2;

while j<=ns
    xi = 2*rand-1;
    yi = 2*rand-1;
    li = sqrt(xi^2+yi^2);
    fl = s/li;
    x = xi*fl;
    y = yi*fl;
    if sqrt((B(j-1,2)+y-B(:,2)).^2 + (B(j-1,1)+x-B(:,1)).^2)>=s
        B(j,:)=[B(j-1,1)+x B(j-1,2)+y];
        j=j+1;
    end
end
%% writing an input file for the GMT simulations
F(:,1:2)=B./1000;
F(:,3) = 0.0;
F(:,4) = (d/2)/1000;
F(:,5) = 0.18344;
F(:,6) = 3.4332;

dlmwrite('tmp.k',0.633)
dlmwrite('tmp.k',ns,'-append')
dlmwrite('tmp.k',F,'delimiter','˜','-append')
```

B.6. Generation of “blackberry-like” particles

```
R=30;       %radius of big sphere in units of the simulation grid
r=10;       %radius of small sphere in units of the simulation grid

Inp = importdata('32inp');  %import coordinates of n evenly spaced points
x = Inp(:,1).*R;            %on unit sphere from file
y = Inp(:,2).*R;
z = Inp(:,3).*R;

kKR = round([x,y,z]);       %coordinates of small spheres

A=size(kKR,1);              %number of small spheres
Dout=cell(A,1);
%% discretize one small sphere

Din=zeros((2*r+1)^3,3);
    j=1;
    for b=0:2*r
        for c=0:2*r
            for d=0:2*r
                Din(j,1)=-r+b;
                Din(j,2)=-r+c;
                Din(j,3)=-r+d;
                j=j+1;
            end
        end
    end
k=(Din(:,1)).^2+(Din(:,2)).^2+(Din(:,3)).^2<=r^2;
Din=Din(k,:);

%% bringing the small spheres to the positions
for a=1:A
    rx=kKR(a,1);
    ry=kKR(a,2);
    rz=kKR(a,3);
    Dout(a,:)=[Din(:,1)+rx, Din(:,2)+ry, Din(:,3)+rz];
end

%% discretize big sphere

Din=zeros((2*R+1)^3,3);
    j=1;
    for b=0:2*R
        for c=0:2*R
            for d=0:2*R
                Din(j,1)=-R+b;
                Din(j,2)=-R+c;
                Din(j,3)=-R+d;
                j=j+1;
            end
        end
    end
k=(Din(:,1)).^2+(Din(:,2)).^2+(Din(:,3)).^2<=R^2;

Dout(a+1,:)=Din(k,:);

fout=unique(cell2mat(Dout),'rows');

NF = size(fout,1);                                %number of dipoles

F=[(1:NF)',fout(:,1),fout(:,2),fout(:,3)];  %numbering the lines
F(:,5)=1; F(:,6)=1; F(:,7)=1;               %only one material
```

```
%% write results to shape.dat

text=sprintf(['--- file for target option FROM_FILE (homogeneous,isotropic target) '...
              '---
n%d  = NAT
n1.000 0.000 0.000 = target vector a1 (in TF)
n0.000 '...
              '1.000 0.000 = target vector a2 (in TF)
n1. 1. 1. = d_x/d d_y/d d_z/d '...
              '(normally 1 1 1)
n0. 0. 0. = X0(1-3) = location in lattice of "target '...
              'origin"
nJ JX JY JZ ICOMPX,ICOMPY,ICOMPZ',NF]);
dlmwrite('shape.dat',text,'delimiter','');
dlmwrite('shape.dat',FP,'delimiter','
t','precision','%d','-append');
```

B.7. Generation of star-shaped particles

```
R=15;   %radius of big sphere in units of the simulation grid
r=10;    %radius of small sphere in units of the simulation grid

Inp = importdata('10inp');
x = Inp(:,1).*R;
y = Inp(:,2).*R;
z = Inp(:,3).*R;

%% discretize the shape
kKR = round([x,y,z]);       %coordinates of the small spheres

nE = 10;                    %number of extensions

kKE = zeros(size(kKR,1)*nE,3);
jE=1;

for ikK = 1:size(kKR,1)
    for ikE = 1:nE
        Ek = round(kKR(ikK,:) + 1.*ikE.*Inp(ikK,:));
        kKE(jE,:) = Ek;
        jE=jE+1;
    end
end

kKR = [kKR;kKE];
disp(kKR);

P=[kKR(:,1) kKR(:,2) kKR(:,3)];
A=size(kKR,1);              %number of particles
Dout=cell(A,1);
%% discretize one small sphere

Din=zeros((2*r+1)^3,3);
    j=1;
    for b=0:2*r
        for c=0:2*r
            for d=0:2*r
                Din(j,1)=-r+b;
                Din(j,2)=-r+c;
```

```
                Din(j,3)=-r+d;
                j=j+1;
            end
        end
    end
k=(Din(:,1)).^2+(Din(:,2)).^2+(Din(:,3)).^2<=r^2;
Din=Din(k,:);

%% bringing the small spheres to the positions
for a=1:A
    rx=kKR(a,1);
    ry=kKR(a,2);
    rz=kKR(a,3);
    Dout(a,:)=[Din(:,1)+rx, Din(:,2)+ry, Din(:,3)+rz];
end

%% discretize big sphere
zu = 0;
R=R+zu;
Din=zeros((2*R+1)^3,3);
    j=1;
    for b=0:2*R
        for c=0:2*R
            for d=0:2*R
                Din(j,1)=-R+b;
                Din(j,2)=-R+c;
                Din(j,3)=-R+d;
                j=j+1;
            end
        end
    end
k=(Din(:,1)).^2+(Din(:,2)).^2+(Din(:,3)).^2<=R^2;

Dout(a+1,:)=Din(k,:);

fout=unique(cell2mat(Dout),'rows');

NF = size(fout,1);                          %number of dipoles

F=[(1:NF)',fout(:,1),fout(:,2),fout(:,3)];  %numbering the lines
F(:,5)=1; F(:,6)=1; F(:,7)=1;               %only one material
%% write results to shape.dat

text=sprintf(['--- file for target option FROM_FILE (homogeneous,isotropic target) '...
              '---
n%d  = NAT
n1.000 0.000 0.000 = target vector a1 (in TF)
n0.000 '...
              '1.000 0.000 = target vector a2 (in TF)
n1. 1. 1. = d_x/d d_y/d d_z/d '...
              '(normally 1 1 1)
n0. 0. 0. = X0(1-3) = location in lattice of "target '...
              'origin"
nJ JX JY JZ ICOMPX,ICOMPY,ICOMPZ',NF]);
dlmwrite('shape.dat',text,'delimiter','');
dlmwrite('shape.dat',FP,'delimiter','
t','precision','%d','-append');
```

C. Bash scripts to perform parallel DDA simulations

All DDA simulations were run on the SGI Altix 4700 at the ZIH at TU Dresden using the following scripts for parallel computing.

C.1. Script to run parallel calculations

```
#!/bin/bash
module purge #removes all user loaded modules
module load intel #loads intel library for ifort compiled progs
for((j=400;j<=800;j=j+5));do
mkdir wave_$j
sed -e "s/ngrmpf/0.$j 0.$j 1/g" ddscat.par > wave_$j/ddscat.par
cp ddscat wave_$j/ddscat
cp shape.dat wave_$j/shape.dat
cd wave_$j
bsub -W 12:00 -M 10000000 -o ddscat.out -e ddscat.err ddscat
cd ..
done
```

C.2. Scrip to collect output of parallel calculations

```
#!/bin/bash
awk 'NR==14' wave_400/qtable > allqtable #reads line 14 of inputfile and overwrites and creates allqtable
for((j=400;j<=800;j=j+5));do
cd wave_$j
awk 'NR==15' qtable >> ../allqtable #reads line 15 of qtable and attaches to allqtable
cd ..
done
#script to collect the data of the whole spectrum from all single qtable files
```

Bibliography

[1] Jackson, J. D. *Classical Electrodynamics*; John Wiley & Sons Incorporated, 1999.

[2] Maier, S. A. *Plasmonics: fundamentals and applications*; Springer, 2007.

[3] Kreibig, U.; Volmer, M. *Optical properties of metal clusters*; Springer, 1995.

[4] Le Ru, E. C.; Etchegoin, P. *Principles of Surface-Enhanced Raman Spectroscopy*; And Related Plasmonic Effects; Elsevier Science, 2008.

[5] Bohren, C.; Huffman, D. *Absorption and Scattering of Light by Small Particles*; Absorption and Scattering of Light by Small Particles (Wiley Science Paperback Series); Wiley-VCH, 1998.

[6] Hao, F.; Nordlander, P. *Chemical Physics Letters* **2007**, *446*, 115–118.

[7] Etchegoin, P. G.; Le Ru, E. C.; Meyer, M. *The Journal of Chemical Physics* **2006**, *125*, 164705.

[8] Romaniello, P.; de Boeij, P. L. *The Journal of Chemical Physics* **2005**, *122*, 164303.

[9] Johnson, P. B.; Christy, R. W. *Physical Review B* **1972**, *6*, 4370–4379.

[10] Gaponenko, S. V. *Introduction to Nanophotonics*; Cambridge Univ Press, 2010.

[11] Mie, G. *Annalen der Physik* **1908**.

[12] Gans, R. *Annalen der Physik* **1912**, *342*, 881–900.

[13] Quinten, M.; Schönauer, D.; Kreibig, U. *Zeitschrift Für Physik D-Atoms Molecules and Clusters* **1989**, *12*, 521–525.

[14] Quinten, M.; Kreibig, U. *Surface Science* **1986**, *172*, 557–577.

[15] Sinzig, J.; Quinten, M. *Applied Physics a-Materials Science & Processing* **1994**, *58*, 157–162.

[16] Turkevich, J.; Stevenson, P. C.; Hillier, J. *The Journal of Physical Chemistry* **1953**, *57*, 670–673.

[17] Frens, G. *Nature (London), Physical Science* **1973**, *241*, 20–22.

[18] Sinzig, J.; Radtke, U.; Quinten, M.; Kreibig, U. *Zeitschrift Für Physik D-Atoms Molecules and Clusters* **1993**, *26*, 242–245.

[19] Liz-Marzán, L. M.; Giersig, M.; Mulvaney, P. *Langmuir* **1996**, *12*, 4329–4335.

[20] Li, J.-F.; Huang, Y. F.; Ding, Y.; Yang, Z.-L.; Li, S. B.; Zhou, X. S.; Fan, F. R.; Zhang, W.; Zhou, Z. Y.; Wu, D. Y.; Ren, B.; Wang, Z. L.; Tian, Z.-Q. *Nature* **2010**, *464*, 392–395.

[21] Doering, W. E.; Nie, S. *Analytical Chemistry* **2003**, *75*, 6171–6176.

[22] Mulvaney, S. P.; Musick, M. D.; Keating, C. D.; Natan, M. J. *Langmuir* **2003**, *19*, 4784–4790.

[23] Oldenburg, S. J.; Averitt, R. D.; Westcott, S. L.; Halas, N. J. *Chemical Physics Letters* **1998**, *288*, 243–247.

[24] Prodan, E.; Radloff, C.; Halas, N. J.; Nordlander, P. *Science* **2003**, *302*, 419–422.

[25] Loo, C.; Lowery, A.; Halas, N.; West, J.; Drezek, R. *Nano Letters* **2005**, *5*, 709–711.

[26] Ringler, M.; Ph.D. thesis; LMU Müchen; 2008.

[27] Xu, Y. L. *Applied optics* **1995**, *34*, 4573–4588.

[28] Zuloaga, J.; Prodan, E.; Nordlander, P. *Nano Letters* **2009**, *9*, 887–891.

[29] Yee, K. *IEEE Transactions on Antennas and Propagation* **1966**, *14*, 302–307.

[30] Taflove, A. *IEEE Transactions on Electromagnetic Compatibility* **1980**, 191–202.

[31] Oskooi, A. F.; Roundy, D.; Ibanescu, M.; Bermel, P.; Joannopoulos, J. D.; Johnson, S. G. *Computer Physics Communications* **2010**, *181*, 687–702.

[32] Flatau, P. J.; Draine, B. T. *J. Opt. Soc. Am. A* **1994**, *11*, 1491.

[33] Draine, B. T.; Flatau, P. J. *Journal of the Optical Society of America. A, Optics, image science, and vision* **2008**, *25*, 2693–2703.

[34] Fleischmann, M.; Hendra, P. J.; McQuillan, A. J. *Chemical Physics Letters* **1974**, *26*, 163–166.

[35] Jeanmaire, D. L.; Van Duyne, R. P. *Journal of Electroanalytical Chemistry and Interfacial Electrochemistry* **1977**, *84*, 1–20.

[36] Ziegler, C.; Eychmüller, A. *The Journal of Physical Chemistry C* **2011**, *115*, 4502–4506.

[37] Turkevich, J.; Stevenson, P.; Hillier, J. *Discussions of the Faraday Society* **1951**, *11*, 55–75.

[38] Brust, M.; Walker, M.; Bethell, D.; Schiffrin, D. J.; Whyman, R. *Journal of the Chemical Society, Chemical Communications* **1994**, 801.

[39] Schmid, G.; Pfeil, R.; Boese, R.; Bandermann, F.; Meyer, S.; Calis, G. H. M.; van der Velden, J. W. A. *Chemische Berichte* **1981**, *114*, 3634–3642.

[40] Andreescu, D.; Sau, T. K.; Goia, D. V. *Journal of Colloid And Interface Science* **2006**, *298*, 742–751.

[41] Martin, M. N.; Basham, J. I.; Chando, P.; Eah, S.-K. *Langmuir* **2010**, *26*, 7410–7417.

[42] Myroshnychenko, V.; Rodríguez-Fernández, J.; Pastoriza-Santos, I.; Funston, A. M.; Novo, C.; Mulvaney, P.; Liz-Marzán, L. M.; García de Abajo, F. J. *Chemical Society Reviews* **2008**, *37*, 1792.

[43] Jana, N. R. *Small* **2005**, *1*, 875–882.

[44] Murphy, C. J.; Sau, T. K.; Gole, A. M.; Orendorff, C. J.; Gao, J.; Gou, L.; Hunyadi, S. E.; Li, T. *The Journal of Physical Chemistry B* **2005**, *109*, 13857–13870.

[45] Sau, T. K.; Murphy, C. J. *Journal of the American Chemical Society* **2004**, *126*, 8648–8649.

[46] Cao, L.; Zhu, T.; Liu, Z. *Journal of Colloid And Interface Science* **2006**, *293*, 69–76.

[47] Jana, N.; Gearheart, L.; Murphy, C. *Advanced Materials* **2001**, *13*, 1389–1393.

[48] Chen, H. M.; Liu, R.-S.; Tsai, D. P. *Crystal Growth & Design* **2009**, *9*, 2079–2087.

[49] Millstone, J. E.; Wei, W.; Jones, M. R.; Yoo, H.; Mirkin, C. A. *Nano Letters* **2008**, *8*, 2526–2529.

[50] Yang, Y.; Yan, Y.; Wang, W.; Li, J. *Nanotechnology* **2008**, *19*, 175603.

[51] Wang, H.; Halas, N. J. *Advanced Materials* **2008**, *20*, 820–825.

[52] Goia, D. V.; Matijevic, E. *Colloids and Surfaces A: Physicochemical and ...* **1999**, *146*, 139–152.

[53] Jana, N. R.; Gearheart, L.; Murphy, C. J. *Langmuir* **2001**, *17*, 6782–6786.

[54] Rodríguez-Fernández, J.; Pérez-Juste, J.; García de Abajo, F. J.; Liz-Marzán, L. M. *Langmuir* **2006**, *22*, 7007–7010.

[55] Perrault, S. D.; Chan, W. C. W. *Journal of the American Chemical Society* **2009**, *131*, 17042–17043.

[56] Niu, J.; Zhu, T.; Liu, Z. *Nanotechnology* **2007**, *18*, 325607.

[57] Brown, K. R.; Walter, D. G.; Natan, M. J. *Chemistry of Materials* **2000**, *12*, 306–313.

[58] Bakshi, M. S. *Langmuir* **2009**, *25*, 12697–12705.

[59] Jana, N. R.; Gearheart, L.; Murphy, C. J. *Chemistry of Materials* **2001**, *13*, 2313–2322.

[60] Sperling, R. A.; Rivera Gil, P.; Zhang, F.; Zanella, M.; Parak, W. J. *Chemical Society Reviews* **2008**, *37*, 1896.

[61] Giljohann, D. A.; Seferos, D. S.; Daniel, W. L.; Massich, M. D.; Patel, P. C.; Mirkin, C. A. *Angewandte Chemie International Edition* **2010**, *49*, 3280–3294.

[62] Wilson, R. *Chemical Society Reviews* **2008**, *37*, 2028.

[63] Liu, N.; Prall, B. S.; Klimov, V. I. *Journal of the American Chemical Society* **2006**, *128*, 15362–15363.

[64] Perepichka, D. F.; Rosei, F. *Angewandte Chemie International Edition* **2007**, *46*, 6006–6008.

[65] Mätzler, C. *IAP Res. Rep* **2002**.

[66] Segelstein, D.; Ph.D. thesis; University of Missouri; Kansas City; 1981.

[67] Bigall, N. C.; Härtling, T.; Klose, M.; Simon, P.; Eng, L. M.; Eychmüller, A. *Nano Letters* **2008**, *8*, 4588–4592.

[68] Zhao, L.; Ji, X.; Sun, X.; Li, J.; Yang, W.; Peng, X. *The Journal of Physical Chemistry C* **2009**, *113*, 16645–16651.

[69] Haiss, W.; Thanh, N. T. K.; Aveyard, J.; Fernig, D. G. *Analytical Chemistry* **2007**, *79*, 4215–4221.

[70] Khlebtsov, N. G. *Analytical Chemistry* **2008**, *80*, 6620–6625.

[71] Khlebtsov, N. G.; Bogatyrev, V. A.; Dykman, L. A.; Melnikov, A. G. *Journal of Colloid And Interface Science* **1996**, *180*, 436–445.

[72] Scholl, J. A.; Koh, A. L.; Dionne, J. A. *Nature* **2012**, *483*, 421–427.

[73] Langille, M. R.; Personick, M. L.; Zhang, J.; Mirkin, C. A. *Journal of the American Chemical Society* **2012**, *134*, 14542–14554.

[74] Peng, Z. A.; Peng, X. *Journal of the American Chemical Society* **2001**, *123*, 1389–1395.

[75] Ji, X.; Song, X.; Li, J.; Bai, Y.; Yang, W.; Peng, X. *Journal of the American Chemical Society* **2007**, *129*, 13939–13948.

[76] Ojea-Jiménez, I.; Bastús, N. G.; Puntes, V. *The Journal of Physical Chemistry C* **2011**, *115*, 15752–15757.

[77] Kimling, J.; Maier, M.; Okenve, B.; Kotaidis, V.; Ballot, H.; Plech, A. *The Journal of Physical Chemistry B* **2006**, *110*, 15700–15707.

[78] Xia, H.; Bai, S.; Hartmann, J.; Wang, D. *Langmuir* **2010**, *26*, 3585–3589.

[79] Zhao, L.; Jiang, D.; Cai, Y.; Ji, X.; Xie, R.; Yang, W. *Nanoscale* **2012**, *4*, 5071–5076.

[80] Pong, B. K.; Elim, H. I.; Chong, J. X.; Ji, W.; Trout, B. L.; Lee, J. Y. *The Journal of Physical Chemistry C* **2007**, *111*, 6281–6287.

[81] Polte, J.; Ahner, T. T.; Delissen, F.; Sokolov, S.; Emmerling, F.; Thünemann, A. F.; Kraehnert, R. *Journal of the American Chemical Society* **2010**, *132*, 1296–1301.

[82] Rodríguez-Fernández, J.; Novo, C.; Myroshnychenko, V.; Funston, A. M.; Sánchez-Iglesias, A.; Pastoriza-Santos, I.; Pérez-Juste, J.; de Abajo, F. J. G.; Liz-Marzán, L. M.; Mulvaney, P. *The Journal of Physical Chemistry C* **2009**, *113*, 18623–18631.

[83] Vitos, L.; Ruban, A. V.; Skriver, H. L.; Kollar, J. *Surface Science* **1998**, *411*, 186–202.

[84] Montejano-Carrizales, J. M.; Rodríguez-López, J. L.; Pal, U.; Miki-Yoshida, M.; José-Yacamán, M. *Small* **2006**, *2*, 351–355.

[85] Sánchez-Iglesias, A.; Pastoriza-Santos, I.; Pérez-Juste, J.; Rodríguez-González, B.; García de Abajo, F. J.; Liz-Marzán, L. M. *Advanced Materials* **2006**, *18*, 2529–2534.

[86] Lofton, C.; Sigmund, W. *Advanced Functional Materials* **2005**, *15*, 1197–1208.

[87] Li, K.; Stockman, M. I.; Bergman, D. J. *Physical Review Letters* **2003**, *91*.

[88] Nie, S.; Emory, S. R. *Science* **1997**, *275*, 1102–1106.

[89] Küstner, B.; Gellner, M.; Schütz, M.; Schöppler, F.; Marx, A.; Ströbel, P.; Adam, P.; Schmuck, C.; Schlücker, S. *Angewandte Chemie International Edition* **2009**, *48*, 1950–1953.

[90] Chang, S.; Ko, H.; Singamaneni, S.; Gunawidjaja, R.; Tsukruk, V. V. *Analytical Chemistry* **2009**, *81*, 5740–5748.

[91] McAloney, R. A.; Sinyor, M.; Dudnik, V.; Goh, M. C. *Langmuir* **2001**, *17*, 6655–6663.

[92] McAloney, R. A.; Dudnik, V.; Goh, M. C. *Langmuir* **2003**, *19*, 3947–3952.

[93] Schneider, C. A.; Rasband, W. S.; Eliceiri, K. W. *Nature Methods* **2012**, *9*, 671–675.

[94] Ghosh, S. K.; Pal, T. *Chemical Reviews* **2007**, *107*, 4797–4862.

[95] Toderas, F.; Baia, M.; Baia, L.; Astilean, S. *Nanotechnology* **2007**, *18*, 255702.

[96] Liao, J.; Zhang, Y.; Yu, W.; Xu, L.; Ge, C.; Liu, J.; Gu, N. *Colloids and Surfaces A: Physicochemical and Engineering Aspects* **2003**, *223*, 177–183.

[97] Li, M.; Johnson, S.; Guo, H.; Dujardin, E.; Mann, S. *Advanced Functional Materials* **2011**, *21*, 851–859.

[98] Hussain, I.; Brust, M.; Barauskas, J.; Cooper, A. I. *Langmuir* **2009**, *25*, 1934–1939.

[99] Han, X.; Goebl, J.; Lu, Z.; Yin, Y. *Langmuir* **2011**, *27*, 5282–5289.

[100] Zhong, Z.; Patskovskyy, S.; Bouvrette, P.; Luong, J. H. T.; Gedanken, A. *The Journal of Physical Chemistry B* **2004**, *108*, 4046–4052.

[101] Nordlander, P.; Oubre, C.; Prodan, E.; Li, K.; Stockman, M. I. *Nano Letters* **2004**, *4*, 899–903.

[102] Zeman, E. J.; Schatz, G. C. *The Journal of Physical Chemistry* **1987**, *91*, 634–643.

[103] Le Ru, E. C.; Blackie, E.; Meyer, M.; Etchegoin, P. G. *The Journal of Physical Chemistry C* **2007**, *111*, 13794–13803.

[104] Osawa, M.; Matsuda, N.; Yoshii, K.; Uchida, I. *The Journal of Physical Chemistry* **1994**, *98*, 12702–12707.

[105] Wang, Y.; Zou, X.; Ren, W.; Wang, W.; Wang, E. *The Journal of Physical Chemistry C* **2007**, *111*, 3259–3265.

[106] Cai, W. B.; Ren, B.; Li, X. Q.; She, C. X.; Liu, F. M.; Cai, X. W.; Tian, Z. Q. *Surface Science* **1998**, *406*, 9–22.

[107] Zhu, Z.; Zhu, T.; Liu, Z. *Nanotechnology* **2004**, *15*, 357–364.

[108] Pérez-González, O.; Zabala, N.; Borisov, A. G.; Halas, N. J.; Nordlander, P.; Aizpurua, J. *Nano Letters* **2010**, *10*, 3090–3095.

[109] Romero, I.; Aizpurua, J.; Bryant, G. W.; García de Abajo, F. J. *Optics Express* **2006**, *14*, 9988–9999.

[110] Link, S.; El-Sayed, M. A. *The Journal of Physical Chemistry B* **1999**, *103*, 8410–8426.

[111] Mohanan, J. L.; Arachchige, I. U.; Brock, S. L. *Science* **2005**, *307*, 397–400.

[112] Gaponik, N.; Herrmann, A.-K.; Eychmüller, A. *The Journal of Physical Chemistry Letters* **2011**, *3*, 8–17.

[113] Lesnyak, V.; Wolf, A.; Dubavik, A.; Borchardt, L.; Voitekhovich, S. V.; Gaponik, N.; Kaskel, S.; Eychmüller, A. *Journal of the American Chemical Society* **2011**, *133*, 13413–13420.

[114] Bigall, N. C.; Herrmann, A.-K.; Vogel, M.; Rose, M.; Simon, P.; Carrillo-Cabrera, W.; Dorfs, D.; Kaskel, S.; Gaponik, N.; Eychmüller, A. *Angewandte Chemie International Edition* **2009**, *48*, 9731–9734.

[115] Reincke, F.; Hickey, S. G.; Kegel, W. K.; Vanmaekelbergh, D. *Angewandte Chemie International Edition* **2004**, *43*, 458–462.

[116] Wang, Y.; Chen, H.; Wang, E. *Nanotechnology* **2008**, *19*, 105604.

[117] Heath, J.; Knobler, C.; Leff, D. *The Journal of Physical Chemistry B* **1997**, *101*, 189–197.

[118] Tang, Z.; Zhang, Z.; Wang, Y.; Glotzer, S. C.; Kotov, N. A. *Science* **2006**, *314*, 274–278.

[119] Jin, R. *Science* **2001**, *294*, 1901–1903.

[120] Ziegler, C.; Klose, M.; Voitekhovich, S. V.; Gaponik, N.; Eychmüller, A. *Zeitschrift für Physikalische Chemie* **2011**, *225*, 363–371.

[121] Sau, T. K.; Rogach, A. L.; Jäckel, F.; Klar, T. A.; Feldmann, J. *Advanced Materials* **2010**, *22*, 1805–1825.

[122] Narayanan, R.; El-Sayed, M. A. *The Journal of Physical Chemistry B* **2005**, *109*, 12663–12676.

[123] Liz-Marzán, L. M. *Langmuir* **2006**, *22*, 32–41.

[124] Lesnyak, V.; Voitekhovich, S. V.; Gaponik, P. N.; Gaponik, N.; Eychmüller, A. *ACS Nano* **2010**, *4*, 4090–4096.

[125] Nichick, M. N.; Voitekhovich, S. V.; Shavel, A.; Lesnikovich, A. I.; Ivashkevich, O. A. *Polyhedron* **2009**, *28*, 3138–3142.

[126] Voitekhovich, S. V.; Talapin, D. V.; Klinke, C.; Kornowski, A.; Weller, H. *Chemistry of Materials* **2008**, *20*, 4545–4547.

[127] International Business Machines Corporation, Columbia University **2006**.

[128] Herr, R. J. *Bioorganic & Medicinal Chemistry* **2002**, *10*, 3379–3393.

[129] Lee, P. C.; Meisel, D. *The Journal of Physical Chemistry* **1982**, *86*, 3391–3395.

[130] Aravind, P. K.; Nitzan, A.; Metiu, H. *Surface Science* **1981**, *110*, 189–204.

[131] Chen, G.; Wang, Y.; Yang, M.; Xu, J.; Goh, S. J.; Pan, M.; Chen, H. *Journal of the American Chemical Society* **2010**, *132*, 3644–3645.

[132] Thomas, S.; Biswas, N.; Venkateswaran, S.; Kapoor, S.; Naumov, S.; Mukherjee, T. *The Journal of Physical Chemistry A* **2005**, *109*, 9928–9934.

[133] Kittler, S.; Greulich, C.; Diendorf, J.; Köller, M.; Epple, M. *Chemistry of Materials* **2010**, *22*, 4548–4554.

[134] Billes, F.; Endredi, H.; Keresztury, G. *Journal of Molecular Structure: THEOCHEM* **2000**, *530*, 183–200.

[135] Thomas, J. M.; Thomas, W. J. *Principles and Practice of Heterogeneous Catalysis*; Wiley-VCH: Weinheim, 2005.

[136] Schüth, F. *Chemie in unserer Zeit* **2006**, *40*, 92–103.

[137] Meulenkamp, E. A. *The Journal of Physical Chemistry B* **1998**, *102*, 5566–5572.

[138] Slama, R.; Ghribi, F.; Houas, A.; Barthou, C.; El Mir, L. *Thin Solid Films* **2011**, *519*, 5792–5795.

[139] Davis, M.; Hikal, W. M.; Gümeci, C.; Hope-Weeks, L. J. *Catalysis Science & Technology* **2012**, *2*, 922.

[140] Wang, C.-T.; Lin, J.-C. *Applied Surface Science* **2008**, *254*, 4500–4507.

[141] Krumm, M.; Pueyo, C. L.; Polarz, S. *Chemistry of Materials* **2010**, *22*, 5129–5136.

[142] Gao, Y. P.; Sisk, C. N.; Hope-Weeks, L. J. *Chemistry of Materials* **2007**, *19*, 6007–6011.

[143] Dilger, S.; Lizandara-Pueyo, C.; Krumm, M.; Polarz, S. *Advanced Materials* **2011**, *24*, 543–548.

[144] Sun, T.; Qiu, J.; Liang, C. *The Journal of Physical Chemistry C* **2008**, *112*, 715–721.

[145] Haruta, M. *The Chemical Record* **2003**, *3*, 75–87.

[146] Hashmi, A. S. K. *Angewandte Chemie International Edition* **2005**, *44*, 6990–6993.

[147] Lee, M.-K.; Tu, H.-F. *Journal of the Electrochemical Society* **2008**, *155*, D758.

[148] Manzoli, M.; Chiorino, A.; Boccuzzi, F. *Applied Catalysis B: Environmental* **2004**, *52*, 259–266.

[149] Iwasa, N.; Mayanagi, T.; Nomura, W.; Arai, M.; Takezawa, N. *Applied Catalysis A: General* **2003**, *248*, 153–160.

[150] Cao, C.; Xia, G.; Holladay, J.; Jones, E.; Wang, Y. *Applied Catalysis A: General* **2004**, *262*, 19–29.

[151] Chin, Y. H.; Dagle, R.; Hu, J.; Dohnalkova, A. C.; Wang, Y. *Catalysis Today* **2002**, *77*, 79–88.

[152] Chinayon, S.; Mekasuwandumrong, O.; Praserthdam, P.; Panpranot, J. *Catalysis Communications* **2008**, *9*, 2297–2302.

[153] Cubeiro, M. L.; Fierro, J. L. G. *Journal of Catalysis* **1998**, *179*, 150–162.

[154] Althues, H.; Ph.D. thesis; TU Dresden; Dresden; 2007.

[155] Liu, W.; Herrmann, A.-K.; Geiger, D.; Borchardt, L.; Simon, F.; Kaskel, S.; Gaponik, N.; Eychmüller, A. *Angewandte Chemie International Edition* **2012**, *51*, 5743–5747.

[156] Henglein, A. *The Journal of Physical Chemistry B* **2000**, *104*, 6683–6685.

[157] Rouquerol, F.; Rouquerol, J.; Sing, K. *Adsorption by Powders and Porous Solids: Principles, Methodology and Applications.*; Elsevier Ltd, 1999.

[158] Zhang, K.; Hong, J.; Cao, G.; Zhan, D.; Tao, Y.; Cong, C. *Thermochimica Acta* **2005**, *437*, 145–149.

[159] Małecka, B. *Journal of Thermal Analysis and Calorimetry* **2004**, *78*, 535–544.

[160] Armbrüster, M.; Kovnir, K.; Behrens, M.; Teschner, D.; Grin, Y.; Schlögl, R. *Journal of the American Chemical Society* **2010**, *132*, 14745–14747.

[161] Köhler, D.; Heise, M.; Baranov, A. I.; Luo, Y.; Geiger, D.; Ruck, M.; Armbrüster, M. *Chemistry of Materials* **2012**, *24*, 1639–1644.

[162] Osswald, J.; Kovnir, K.; Armbrüster, M.; Giedigkeit, R.; Jentoft, R. E.; Wild, U.; Grin, Y.; Schlögl, R. *Journal of Catalysis* **2008**, *258*, 219–227.

Danksagung

In den letzten dreieinhalb Jahren habe ich viele Freiheiten bei der Verwirklichung meiner eigenen Forschungs- und auch Bildungsinteressen genossen. Dafür, und für die Erkenntnis, dass es manchmal leichter ist Probleme zu lösen als sich welche auszudenken, möchte ich mich bei Herrn Prof. Eychmüller herzlich bedanken. Ich weiß es auch sehr zu schätzen, dass ich die Möglichkeit hatte auf sehr viele wunderschöne Dienstreisen zu fahren.

Dem gesamten Arbeitskreis Eychmüller danke ich für die angenehme, ungezwungene und offene Arbeitsatmosphäre. Auch wenn ich sehr oft nur in meinem dunklen Raman-Kämmerchen gesessen habe und dadurch das ein oder andere Arbeitsgruppenseminar verpasst habe, war es doch stets angenehm das Büro zu verlassen und “frische” Laborluft zu schnuppern.

Ein ganz besonderer Dank gilt den fleißigen Korrekturlesern Anne, Puppe, Daniel und Schriggi, die mit viel Akribie meine “fremdsprachige” Arbeit auf Fehler und Unstimmigkeiten untersucht haben.

Natürlich möchte ich mich auch bei all den SHKs und Praktikanten, die mich während meiner Promotionszeit durch viele praktische Arbeiten unterstützt haben, bedanken. Ein besonderer Dank gilt meinem “Zögling” Stefan, für die gute Büropartnerschaft und die gute Zusammenarbeit in der “Spitzenforschung”.

Man findet neben der Promotion tatsächlich noch Zeit für andere Dinge! Für mich waren das der Sport und die Musik. Ich möchte an dieser Stelle die Gelegenheit nutzen, um mich für die tolle Zeit in der Halle und die mitunter verheerenden Bierstubenabende bei all den Volleyballern zu bedanken, die regelmäßig dabei waren, insbesondere natürlich bei den Mannschaften “Eiskalt” und der “Broilerbande”. Außerdem möchte ich mich bei der Band “Yellow Cap” für die herzliche Aufnahme, die tollen Konzerterlebnisse und die großartigen Tourneen durch ganz Europa vielmals bedanken.

Inzwischen bin ich nun fast zehn Jahre in Dresden. In dieser Zeit begegnet man vielen Menschen. Ich hatte das Glück einige sehr liebe Menschen kennenzulernen. Es sind großartige Freundschaften entstanden, Freundschaften fürs Leben. Besonders möchte ich mich bei Puppe, Bartschi, Hase, Daniel und Schnucki bedanken, dass ihr immer für mich da seid und mich immer mal daran erinnert, dass auch mein Tag nur 24 Stunden hat.

Es ist und bleibt das wichtigste im Leben - die Familie. Eine gut funktionierende Familie, in der sich jeder auf jeden verlassen kann, die einem ohne Nachfrage hilft und in der man sich wohl fühlt ist heutzutage nicht mehr selbstverständlich. Ich bin glücklich und stolz eine solche Familie zu haben. Vielen Dank für alles!

Versicherung

Hiermit versichere ich, dass ich die vorliegende Arbeit ohne unzulässige Hilfe Dritter und ohne Benutzung anderer als der angegebenen Hilfsmittel angefertigt habe; die aus fremden Quellen direkt oder indirekt übernommenen Gedanken sind als solche kenntlich gemacht. Die Arbeit wurde bisher weder im Inland noch im Ausland in gleicher oder ähnlicher Form einer anderen Prüfungsbehörde vorgelegt.

Datum, Unterschrift

Erklärung

Die vorgelegte Dissertation mit dem Titel: „Syntheses and Assemblies of Noble Metal Nanostructures“ wurde in der Zeit von Mai/2009 bis November/2012 in der Professur für Physikalische Chemie/Elektrochemie an der TU Dresden, unter der wissenschaftlichen Betreuung von Prof. Dr. rer. nat. habil. Alexander Eychmüller angefertigt.

Es existieren keine früheren Promotionsverfahren.

Hiermit erkenne ich die Promotionsordnung der Fakultät Mathematik und Naturwissenschaften der Technischen Universität Dresden vom 23.02.2011 an.

Datum, Unterschrift